Characterizing Transition Temperature Gas in the Galactic Corona

Bart P. Wakker[1], Blair D. Savage[1], Andrew J. Fox[2,3], Robert Benjamin[4],

ABSTRACT

We present a study of the properties of the transition temperature ($T \sim 10^5$ K) gas in the Milky Way corona, based on measurements of O VI, N V, C IV, Si IV and Fe III absorption lines seen in the far ultraviolet spectra of 58 sightlines to extragalactic targets, obtained with *Far-Ultraviolet Spectroscopic Explorer* (FUSE) and *Space Telescope Imaging Spectrograph*. In many sightlines the Galactic absorption profiles show multiple components, which are analyzed separately. We find that the highly-ionized atoms are distributed irregularly in a layer with a scaleheight of about 3 kpc, which rotates along with the gas in the disk, without an obvious gradient in the rotation velocity away from the Galactic plane. Within this layer the gas has randomly oriented velocities with a dispersion of 40–60 km s^{-1}. On average the integrated column densities are log N(O VI)=14.3, log N(N V)=13.5, log N(C IV)=14.2, log N(Si IV)=13.6 and log N(Fe III)=14.2, with a dispersion of just 0.2 dex in each case. In sightlines around the Galactic Center and Galactic North Pole all column densities are enhanced by a factor $\sim$2, while at intermediate latitudes in the southern sky there is a deficit in N(O VI) of about a factor 2, but no deficit for the other ions. We compare the column densities and ionic ratios to a series of theoretical predictions: collisional ionization equilibrium, shock ionization, conductive interfaces, turbulent mixing, thick disk supernovae, static non-equilibrium ionization (NIE) radiative cooling and an NIE radiative cooling model in which the gas flows through the cooling zone. None of these models can fully reproduce the data, but it is clear that non-equilibrium ionization radiative cooling is important in generating the transition temperature gas.

[1]Department of Astronomy, University of Wisconsin, Madison, WI 53706; wakker@astro.wisc.edu, savage@astro.wisc.edu

[2]European Southern Observatory, Alonso de Córdova 3107, Casilla 19001, Vitacura, Santiago, Chile

[3]Institute of Astronomy, University of Cambridge, Madingley Road, Cambridge, CB3 0HA, UK; afox@eso.org

[4]Department of Physics, University of Wisconsin, Whitewater, 800 West Main Street, Whitewater WI 53190; benjamir@wisp.physics.wisc.edu

Subject headings: ISM: clouds, ISM: general, Galaxy: halo, ultraviolet: ISM

1. Introduction

Understanding the processes in Milky Way Disk, Thick Disk and Halo gas that generate gas at temperatures $T > 10^5$ K is a crucial element in learning about the lifecycle of gas in galaxies. Such gas can be produced by supernovae, winds and infall, and its presence traces the circumstances of galactic evolution. Spitzer (1956) originally proposed the existence of a "hot interstellar Galactic Corona", with $T \sim 10^6$ K, to account for the presence of neutral clouds about 1 kpc above the Galactic plane (Münch 1952; Münch & Zirin 1961), the idea being that these clouds could only persist if they were confined by the pressure of an external medium. After the detection of the diffuse galactic soft X-ray background (Bunner et al. 1973, Williamson et al. 1974) and of O VI absorption (Rogerson et al. 1973; York 1974; Jenkins & Meloy 1974), Shapiro & Field (1976) proposed that this hot gas would produce a "Galactic Fountain" – a process in which the ISM is heated by supernova explosions, expands away from the Galactic plane, tries to settle hydrostatically, but as it cools clouds with $T \sim 10^4$ K rain back on the disk. This is a natural way to produce moving clouds of cooler gas embedded in a hot medium. The precise predictions of the process depend on many factors, most importantly the ratio of free-fall time to cooling time (Bregman 1980; Kahn 1981; Houck & Bregman 1990). Other ways to produce hot coronal gas have also been proposed. E.g., a Galactic wind originating in the center (see Everett et al. 2008 and references therein) or heat generated by accreting clouds (considered by Henley et al. 2010).

In his original paper, Spitzer (1956) pointed out that the $(1s^2 2s)^2 S_{1/2} \rightarrow (1s^2 2p)^2 P_{1/2,3/2}$ electronic transitions of the lithium-like ions O^{+5}, N^{+4} and C^{+3} (and the similar Si-ion Si^{+3}) produce resonance doublet absorption lines in the UV (at $\lambda \sim 1030$, 1240, 1550 and $1400\,\text{Å}$, respectively). These ions have ionization potentials for production of 113.9, 77.5, 47.9 and 33.5 eV and trace gas in the 1–3×10^5 K temperature range, which originates in processes that convert 10^6 K into 10^4 K gas and vice versa. At the temperatures sampled by these ions, the ISM is unstable – left to itself it will rapidly cool to below 10^4 K. The presence of these ions therefore implies the existence of 10^6 K or hotter gas that has cooled down or of a process that is heating cooler gas.

Here two notes about nomenclature are in order. First, Spitzer used "Corona" for the region containing hot gas out to a few kpc from the Galactic plane. "Halo" has often been used instead, referring to the region of space outside the Galactic disk. As the scaleheights of O VI, NV and C IV are found to be only ~ 3 kpc, Savage et al. (2003) refer to the region where the 10^5 K gas occurs as a "Thick Disk", as opposed to a much more extended

($>$50 kpc) Corona that is implied by the detection of O VI absorption associated with the Magellanic Stream (Sembach et al. 2003). We will follow Savage et al. (2003) in using this terminology. Second, the term "hot gas" has often been used to describe gas with $T$$>$$10^5$ K, using "warm gas" if the temperature is $\sim$5000 K to a few 10^4 K. However, since gas at temperatures $\sim$$10^5$ K has very different properties than gas at $T$$\sim$$10^5$ K (not the least of which is that is it cools rapidly), We will instead follow the convention of Savage & Wakker (2009), who proposed to instead use the term "transition temperature gas" for this quickly-evolving phase, reserving "hot gas" for the X-ray emitting phase with $T$$>$$10^6$ K.

The desire to detect the highly-ionized interstellar atoms was one of Spitzer's main motivators to push for the creation of a UV satellite in space, resulting in the launch of the Copernicus satellite in 1972. Other UV spectroscopic instruments followed, including the International Ultraviolet Explorer (*IUE*), the Goddard High Resolution Spectrograph (GHRS), the Space Telescope Imaging Spectrograph (STIS), the Far Ultraviolet Spectroscopic Explorer (*FUSE*) and the Cosmic Origins Spectrograph (COS). These instruments can detect the highly-ionized ions in the Milky Way disk and corona in absorption against both stars and extragalactic targets. Many such studies have been done: York (1974, 1977), Jenkins & Meloy (1974), Jenkins (1978a, 1978b), Cowie et al. (1979, 1981), Savage & de Boer (1979, 1981), Savage & Massa (1987), Sembach et al. (1990, 1991, 1994a, 1994b, 1995, 1999, 2001), Savage et al. (1990, 1995, 1997a, 1997b, 2001a, 2001b, 2003, 2005), Sembach & Savage (1992, 1994), Tripp et al. (1993), Savage & Sembach (1994), Sembach (1994), Jenkins et al. (1998, 2000), Oegerle et al. (2000, 2005), Sterling et al. (2002), Howk et al. (2002, 2003), Fox et al. (2003), Zsargó et al. (2003), Wakker et al. (2003), Knauth et al. (2003), Lehner et al. (2003), Indebetouw & Shull (2004b), Ganguly et al. (2005), Savage & Lehner (2006), Keeney et al. (2006), Bowen et al. (2008), Savage & Wakker (2009), Lehner et al. (2011). These studies show that in the disk the average density of the ionized hydrogen plasma in which the highly-ionized species occur is about $3$$\times$$10^{-4}$ cm^{-3}, while the scale height of the ions is $2.6$$\pm$$0.6$ kpc for O VI, $3.6^{+1.0}_{-0.8}$ kpc for C IV, and $3.2^{+1.0}_{-0.6}$ kpc for Si IV). The velocity spread of the gas is too low to explain the scaleheight as due to turbulent pressure. The distribution is highly irregular. Finally, the ionization conditions show that the gas is far out of equilibrium.

Starting in the early 1990s, the GHRS and STIS instruments on the Hubble Space Telescope (*HST*) have observed 85 extragalactic targets, usually for the purpose of studying intergalactic absorption in the sightlines. Toward each of these sightlines, absorption by Galactic N V, C IV and/or Si IV is seen. Combined with the $\sim$150 sightlines toward which O VI can be measured using *FUSE*, this dataset presents an opportunity to learn more about the properties of the transition temperature gas in the Milky Way, allowing us to address issues such as its kinematics relative to differential galactic rotation, its vertical velocity

spread, the total amount, its distribution on the sky and relation to other structures, and the physical processes that produce it.

In this paper we provide a table of extragalactic targets observed with *HST* spectrographs between 1992 and 2007, i.e., until the breakdown of the STIS spectrograph (Section 2). At the time this paper was finished (mid 2011), the COS spectrograph (launched in fall 2009) already produced many new spectra covering N V, C IV and Si IV absorption. However, as of September 2011 only a handful are public. and only two sightlines would be added to our sample of sightlines for which high S/N ratio data are available for all four highly-ionized species. Future studies will allow detailed studies of N V, C IV and Si IV in a few hundred sightlines (although O VI will be missing for most of these new sightlines). For each of the targets observed by *HST* before 2007, we include *FUSE* observations if they are available. We then determine the absorption that we think is associated with the thick disk of the Galaxy (Section 3). In a large fraction of the sightlines, absorption is also visible at high velocities ($|v_{\mathrm{LSR}}|{>}100 \mathrm{\,km\,s^{-1}}$; see e.g., Sembach et al. 2003; Fox et al. 2006). We do not include those components in this paper. The data also include absorption lines of ions with low ionization potential (C I, C II, N I, O I, Si II, S II, Ar I, Fe II). We will not address these ions here. A few abundant ions with intermediate ionization potentials (13.6–35 eV) also produce strong UV absorption lines (C III, N III, O III, Al III, Si III, S III and Fe III). Of this set, the Galactic C III λ977.020 and Si III λ1206.500 absorption are always saturated, the Galactic O III and most of the N III lines are in the EUV ($\lambda{<}912$ Å) and thus hidden by the Galactic H I absorption, N III λ989 blends with a strong Si II line. Al III λ1854 was observed by *IUE* toward many stars (see e.g. Savage & Wakker 2009), but lies outside the wavelength range of most existing *HST* spectra. However, S III λ1012.501 and Fe III λ1122.524 are visible in *FUSE* spectra (although the S III line is usually contaminated by Galactic H_2 absorption). In this paper, we will include S III and Fe III in our analyses, allowing a comparison of the properties of the warm ionized medium with the more highly-ionized transition temperature gas.

We list the measured column densities and other parameters of O VI, N V, C IV, Si IV, Fe III and S III for the Thick Disk component of the high-ion absorption lines in Section 3. Section 4 presents a discussion of the properties of the absorption, such as their distribution across the sky, the kinematical relationships between the different ions, and the column density ratios. We address the physical processes that cause these ions to appear in Section 5, where we present a discussion of the predictions for ionic column density ratios implied by the various models that have been proposed. Compared to earlier discussions (Spitzer 1990; Savage et al. 1997b; Fox et al. 2004; Indebetouw & Shull 2004a) we look more precisely at the numerical predictions for ionic ratios, and we consider several new models. Finally, we discuss what we have learned in Section 6.

2. Observations

2.1. Sources of data

In Table 1 we give observational information for the high-resolution ($R{>}10000$) GHRS, STIS-G140M or STIS-E140M spectra that were taken before 2007 and for which the signal-to-noise ratio per 20 $\mathrm{km\,s^{-1}}$ near either the N V or C IV line is larger than 7. This S/N limit is used because at lower S/N ratios the Galactic absorption lines become difficult to measure and the error in the ratios derived between ionic column densities is larger than a factor 2.

Table 1.   Observational data

Object	Lon [deg]	Lat [deg]	Status[a]	Instrument[b]	Resol[c] [km s^{-1}]	T$_{exp}$ [ks]	S/N O VI	S/N N V	S/N C IV	S/N Si IV	Obs. ID.
(1)	(2)	(3)	(4)	(5)	(6)	(7)	(8)	(9)	(10)	(11)	(12)
3C232	194.17	52.32	Skip	FUSE	20	10.8	1				P10714
				STIS−1222	30	11.2		12			O6700
				STIS−1400	30	11.2				11	O6700
				STIS−1567	30	22.3			13		O6700
3C249.1	130.39	38.55	Ratios	FUSE	20	260.5	16				D11701 P10716 S60109 U10275
				STIS−E140M	8	137.6		7	6	8	O6E10 O6E12 O6E13
3C273.0	289.95	64.36	Ratios	FUSE	20	43.3	27				P10135
				STIS−E140M	8	37.3		28	21	43	O5D30
3C351.0	90.08	36.38	Ratios	STIS−E140M	8	156.3		9	9	9	O5790
ESO141−G55	338.18	−26.71	Ratios	FUSE	20	40.9	16				I90401
				GHRS−1241	19	15.6		16			Z3E70
				GHRS−1247	19	9.8		16			Z3I70
				GHRS−1400	16	9.8				13	Z3I70
				GHRS−1538	14	11.1			12		Z3I70
ESO438−G09	277.55	29.36	Skip	STIS−1222	30	11.1		10			O5EW0
Fairall9	295.07	−57.83	Meas.	FUSE	20	34.8	6				P10106
				GHRS−1238	19	14.4		26			Z3E70
				GHRS−1250	18	8.1		26			Z26O0
				GHRS−1258	18	6.9					Z3E70
				GHRS−1539	14	8.1			6		Z26O0
H1821+643	94.00	27.42	Skip	FUSE	20	278.4	28				C09502 P10164
				STIS−E140M	8	101.9		13	16	19	O5E70
HE0226−4110	253.94	−65.77	Ratios	FUSE	20	204.8	24				D02701 P10191 P20713
				STIS−E140M	8	87.5		8	8	11	O6E10 O6E11
HE0340−2703	222.68	−52.12	Meas.	STIS−1222	30	4.9		11			O8EI0
HE1029−1401	259.33	36.52	Meas.	STIS−1222	30	4.1		33			O4EC0
				STIS−1272	30	3.4					O4EC0
HE1228+0131	291.26	63.66	Ratios	FUSE	20	4.0	5				P10190
				STIS−E140M	8	54.5		5	6	7	O56A0
HS0624+6907	145.71	23.35	Ratios	FUSE	20	132.3	11				P10710 S60112 U10210
				STIS−E140M	8	123.9		7	9	14	O6E10 O6E11
HS1543+5921	92.40	46.36	Skip	FUSE	20	8.5	2				P10805
				STIS−1222	30	25.2		13			O8MR0
				STIS−1272	30	54.0					O8MR0
				STIS−1321	30	49.5					O8MR0
MCG+10−16−111	144.21	55.08	Meas.	STIS−1222	30	19.5		30			O5EW0
MRC2251−178	46.20	−61.33	Meas.	FUSE	20	50.2	12				P11110
				STIS−1222	30	6.0		27			O4EC0
				STIS−1272	30	4.6					O4EC0
Mrk33	156.20	52.80	Skip	FUSE	20	23.7	6				C04805
				STIS−1222	30	15.8		9			O5CA0
Mrk110	165.01	44.36	Meas.	FUSE	20	11.5	1				P10713
				STIS−1222	30	4.5		10			O4N30 O4N35
Mrk205	125.45	41.67	Ratios	FUSE	20	231.9	17				D05401 Q10602 S60108 U10311

Table 1—Continued

Object	Lon [deg]	Lat [deg]	Status[a]	Instrument[b]	Resol[c] [km s^{-1}]	T$_{exp}$ [ks]	S/N O VI	S/N N V	S/N C IV	S/N Si IV	Obs. ID.
(1)	(2)	(3)	(4)	(5)	(6)	(7)	(8)	(9)	(10)	(11)	(12)
				STIS−E140M	8	124.0		8	6	9	O62Q0
Mrk279	115.04	46.86	Ratios	FUSE	20	235.3	44				C09002 D15401 F32501 P10803
				STIS−E140M	8	107.4		30	21	25	O6JM0 O8K10
Mrk290	91.49	47.95	Ratios	FUSE	20	112.9	19				D07601 E08401 P10729
				GHRS−1250	18	7.1		25			Z3KH0
Mrk335	108.76	−41.42	Ratios	FUSE	20	99.2	28				P10102
				STIS−E140M	8	32.3		11	5	7	O8N50
Mrk421	179.83	65.03	Meas.	FUSE	20	82.0	30				P10129 Z01001
				GHRS−1239	19	15.7		24			Z2IA0
Mrk478	59.24	65.03	Meas.	FUSE	20	14.0	8				P11109
				STIS−1222	30	7.6		29			O4EC1
				STIS−1272	30	6.3					O4EC1
Mrk501	63.60	38.86	Meas.	FUSE	20	30.2	9				C08101 P10733
				GHRS−1239	19	31.3		11			Z1A65
Mrk509	35.97	−29.86	Ratios	FUSE	20	90.4	30				P10806 X01701
				STIS−E140M	8	15.7		12	8	9	O6AP0
Mrk771	269.44	81.74	Meas.	FUSE	20	6.3	5				P10723
				STIS−1222	30	7.8		24			O4EC0 O4N30
				STIS−1272	30	5.2					O4EC0
Mrk817	100.30	53.48	Meas.	FUSE	20	186.8	43				P10804
				GHRS−1241	19	26.8		40			Z3E70
Mrk876	98.27	40.38	Ratios	FUSE	20	139.4	33				D02802 P10731 U10366
				STIS−E140M	6	58.4		11	8	16	O8NN0
Mrk926	64.09	−58.76	Skip	FUSE	20	11.2	3				P10740
				STIS−1222	30	3.9		8			O4EC1
				STIS−1272	30	3.7					O4EC1
Mrk1044	179.69	−60.48	Skip	FUSE	20	12.6	6				D04101
				STIS−1222	30	2.4		29			O8K40
				STIS−1272	30	4.8					O8K40
				STIS−1567	30	2.4			12		O8K40
Mrk1095	201.69	−21.13	Meas.	FUSE	20	56.0	10				P10112
				GHRS−1241	19	21.0		20			Z3E70
Mrk1383	349.22	55.12	Ratios	FUSE	20	63.1	23				P10148 P26701
				STIS−E140M	8	38.3		9	8	8	O8PG0
Mrk1502	123.75	−50.18	Meas.	FUSE	20	39.1	7				P11101
				GHRS−1239	19	49.5		10			Z1A60 Z2IA0
Mrk1513	63.67	−29.07	Meas.	FUSE	20	64.3	15				P10183
				STIS−1222	30	7.3		23			O4EC1
				STIS−1272	30	6.2					O4EC1
NGC985	180.84	−59.49	Meas.	FUSE	20	44.3	10				P10109
				STIS−1222	30	3.7		25			O4EC1
				STIS−1272	30	3.8					O4EC1
NGC1705	261.08	−38.74	Ratios	FUSE	20	24.0	27				A04601
				STIS−E140M	8	34.2		13	8	13	O58N0

Table 1—Continued

Object	Lon [deg]	Lat [deg]	Status[a]	Instrument[b]	Resol[c] [km s^{-1}]	T$_{exp}$ [ks]	S/N O VI	S/N N V	S/N C IV	S/N Si IV	Obs. ID.
(1)	(2)	(3)	(4)	(5)	(6)	(7)	(8)	(9)	(10)	(11)	(12)
NGC3516	133.24	42.40	Meas.	FUSE	20	114.5	9				G91701 P11104 P21101
				STIS−E140M	8	13.7		2	20	3	O57B0
NGC3783	287.46	22.95	Ratios	FUSE	20	178.4	26				B10701 E03101 P10133
				STIS−E140M	8	187.4		34	35	28	O57B0 O63M0 O63M1 O63M5
NGC4051	148.88	70.09	Skip	FUSE	20	86.6	16				B06202 C01901
				STIS−E140M	8	20.6		7	8	6	O5F00
NGC4151	155.08	75.06	Ratios	FUSE	20	96.6	36				C09201 P11105 P21102
				STIS−E140M	8	55.4		21	17	22	O5780 O5KT0 O5KT5 O61L0 O6JB0
NGC4593	297.48	57.40	Skip	STIS−E140M	8	22.0		10	7	7	O5L50
NGC5548	31.96	70.50	Ratios	FUSE	20	56.1	9				D15501 P10146
				STIS−E140M	8	107.5		24	11	10	O6JD0 O6KW0
				STIS−E140M	8	4.8		24	11	10	O4LL0
NGC7469	83.10	−45.47	Ratios	FUSE	20	44.0	16				C09001 P10187
				STIS−E140M	8	71.6		25	11	12	O6BN0 O8N50
PG0804+761	138.28	31.03	Meas.	FUSE	20	170.9	31				P10119 S60110
				STIS−1222	30	7.3		20			O4EC0 O4N30
				STIS−1272	30	4.2					O4EC0
PG0953+414	179.79	51.71	Ratios	FUSE	20	75.2	24				P10122
				STIS−E140M	8	49.0		9	9	10	O4X00
PG1001+291	200.08	53.21	Skip	FUSE	20	11.4	5				P20731
				STIS−E140M	8	96.8		7	5	8	O6E10 O6E11 O6E12
PG1004+130	225.12	49.12	Skip	FUSE	20	83.4	8				A03501
				STIS−1222	30	5.2		11			O5EW0
PG1049−005	252.28	49.88	Meas.	STIS−1222	30	1.5		6			O4N30
PG1116+215	223.36	68.21	Ratios	FUSE	20	77.0	25				P10131
				STIS−E140M	8	53.1		12	10	15	O5A30 O5E70
PG1211+143	267.55	74.32	Ratios	FUSE	20	52.2	17				P10720
				STIS−E140M	8	110.0		18	14	20	O61Y0
PG1216+069	281.07	68.14	Ratios	FUSE	20	12.4	4				P10721
				STIS−E140M	8	139.6		8	7	8	O6E10 O6E13
PG1259+593	120.56	58.05	Ratios	FUSE	20	528.1	38				P10801 U10318
				STIS−E140M	8	191.5		7	8	11	O63G0 O63G1
PG1302−102	308.59	52.16	Ratios	FUSE	20	144.7	15				P10802
				STIS−E140M	8	44.2		7	5	5	O5BU0 O5BU6
PG1341+258	28.71	78.15	Skip	STIS−1222	30	8.1		15			O5EW0
PG1351+640	111.89	52.02	Meas.	FUSE	20	119.2	17				P10725 S60107
				STIS−1222	30	8.5		10			O4EC5
				STIS−1272	30	6.2					O4EC5
PG1444+407	69.90	62.72	Ratios	FUSE	20	10.1	4				P10727
				STIS−E140M	8	97.2		8	8	8	O6E10
PG1718+481	74.38	34.83	Meas.	FUSE	20	59.5	2				E01001 P21001
				STIS−1567	30	11.3			22		O4VA0
PHL1811	47.47	−44.81	Ratios	FUSE	20	72.7	17				P10810 P20711
				STIS−E140M	8	67.8		12	9	18	O8D90

Of the set of observations, 9 targets were only observed using the GHRS, 18 were only observed using STIS-G140M and 31 were observed using STIS-E140M. Of the 58 targets used in our analysis, 43 also have *FUSE* data with S/N near O VI greater than 7. There are 55 targets having data with S/N>7 for N V, 33 have such data covering C IV, while for 26 targets the S/N ratio near all three lines is >7. These 26 form the main sample for the current study.

Figure 1 shows the distribution of the analyzed targets on the sky. The integrated Galactic H I column density is also shown, with a contour at a H I column density of $7{\times}10^{20}\,\mathrm{cm}^{-2}$. This shows that the extragalactic UV-bright targets that can be observed with space spectrographs only sample gas at high galactic latitudes, and that these targets are spread fairly evenly across the sky, with the exception of a concentration of targets in the "hole" near l=120°, b=45°, where the extinction is below average, allowing more targets to shine through the Galactic dust. This is also the region of sky where the large high-velocity cloud complex C can be found (Hulsbosch & Wakker 1988), targets behind which have been disproportionally selected for observations with *HST* spectrographs.

Table 1 and Figure 1 include 12 targets for which the status column in the table has the value "Skip". This is the case when the spectra have a sufficiently high S/N ratio, but there are problems with the measurements. E.g., toward H 1821+643 strong absorption is seen that is associated with the planetary nebula K1-16. For NGC 4151, both the STIS-E140M and *FUSE* spectrum have high S/N (∼14), and Galactic absorption is clearly seen in all highly-ionized species, but because of the low redshift of NGC 4151, it is blended with lines associated with the background galaxy, making the Galactic lines impossible to measure. For 3C 232 several STIS-G140M grating settings cover N V, C IV and Si IV, but the absorptions in the individual lines of the C IV and Si IV doublet do not seem to match up. Toward PG 1004+130 the Galactic O VI appears to be broad, as do Si III λ1206.500 and C II λ1036.337. However, a series of intrinsic O III lines probably contaminates the Galactic O VI. Eight other sightlines with high S/N near 1238 Å are excluded from the final sample (ESO 438−G09, HS 1543+5921, Mrk 33, Mrk 926, Mrk 1044, NGC 4593, PG 1001+291 and PG 1341+258). These have low S/N or no data for O VI, and either the two lines of the N V and/or C IV doublet do not match or there are intrinsic AGN lines contaminating the ISM lines. We still include these sightlines in Table 1, so that we can show their spectra in Figure 2, allowing the reader to check on the problems. However, they are not used in the analyses.

Table 1—Continued

Object	Lon [deg]	Lat [deg]	Status[a]	Instrument[b]	Resol[c] [km s⁻¹]	T_exp [ks]	S/N O VI	S/N N V	S/N C IV	S/N Si IV	Obs. ID.
(1)	(2)	(3)	(4)	(5)	(6)	(7)	(8)	(9)	(10)	(11)	(12)
PKS0312−77	293.44	−37.55	Meas.	STIS−E140M	8	46.3		3	3	3	O65T0 O65T1
PKS0405−12	204.93	−41.76	Ratios	FUSE	20	142.2	18				B08701 D10301
				STIS−E140M	8	54.4		7	7	9	O55S0
PKS2005−489	350.37	−32.60	Meas.	FUSE	20	48.6	17				C14903 P10738
				STIS−1222	30	6.1		67			O4EC0
				STIS−1272	30	5.5					O4EC0
PKS2155−304	17.73	−52.25	Ratios	FUSE	20	119.8	31				P10807
				STIS−E140M	8	57.0		11	11	15	O5BY0
RX J0100.4−5113	299.48	−65.84	Meas.	FUSE	20	22.6	9				D80603 E89702
				STIS−1222	30	2.3		8			O8P80
				STIS−1272	30	1.2					O8P80
RX J1830.3+7312	104.04	27.40	Meas.	FUSE	20	23.8	6				G02003
				STIS−1222	19	5.8		29			O5EW0
Ton S180	139.00	−85.07	Meas.	FUSE	20	26.7	14				D02801 P10105
				STIS−1222	30	4.1		27			O4EC0
				STIS−1272	30	3.5					O4EC0
Ton S210	224.97	−83.16	Ratios	FUSE	20	52.5	20				P10703
				STIS−E140M	8	5.1		4	5	7	O6L00
UGC12163	92.14	−25.34	Ratios	FUSE	20	49.9	8				B06201
				STIS−E140M	8	20.6		4	2	4	O5IT0
VIIZw118	151.36	25.99	Meas.	FUSE	20	194.4	18				P10116 S60113 U10215
				STIS−1222	30	9.5		16			O4EC1

Note. — a: Status of the analysis – "Ratios" means that this sightline is used to analyze ionic ratios; "Measured" means that only one or two of the four ions were measured; "Skip" implies that the S/N of the data is sufficient, but the measurement is impossible or ambiguous; b: *FUSE* or *HST* spectrograph, with in the case of GHRS data the central wavelength of the grating setting added; an added central wavelength for STIS data means that the G140M grating was used, otherwise the spectrum was obtained using the E140M echelle; c: approximate size of resolution element.
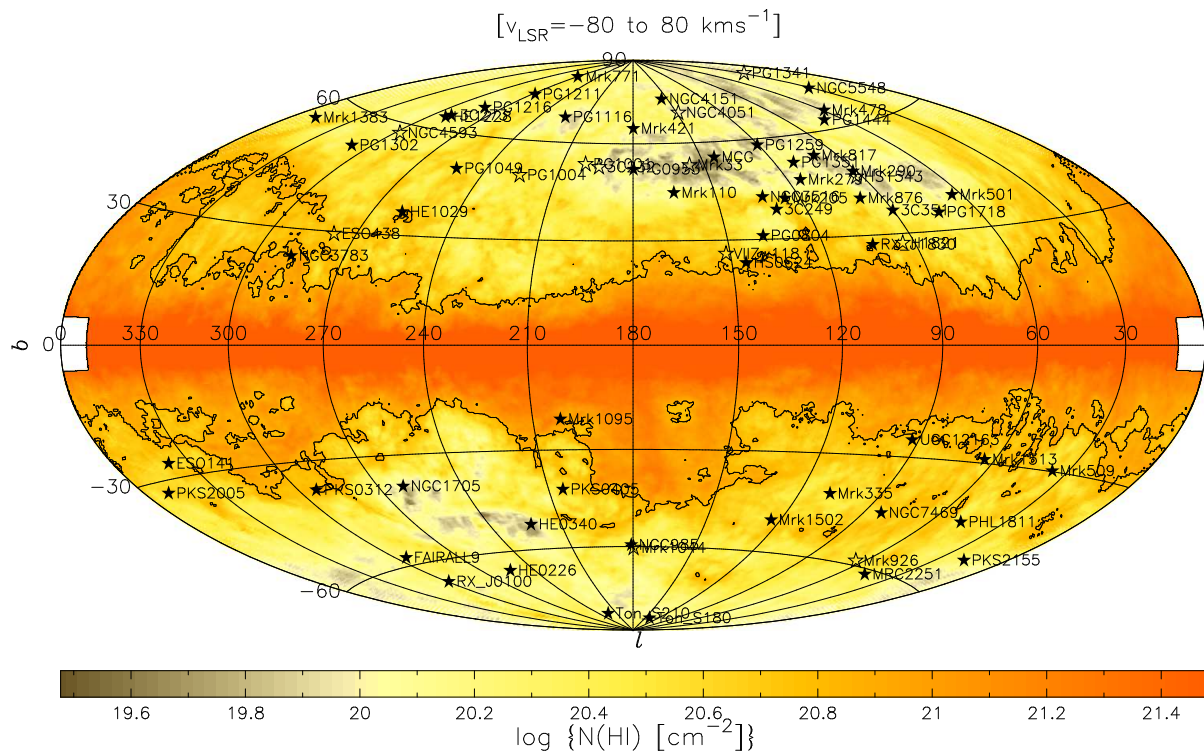
Fig. 1.— Distribution of targets with N V and/or C IV spectra, on top of a map of the logarithm of the column density of the 21-cm H I sky, integrated between -80 and $80 \, \mathrm{km \, s^{-1}}$, with a contour overlaid for $N(\mathrm{H \, I}) = 7 \times 10^{20} \, \mathrm{cm^{-2}}$. The data are shown in an Aitoff projection of Galactic coordinates centered on the Anti-Center direction. The H I data are from the Leiden-Argentina-Bonn (LAB) survey (Kalberla et al. 2005).

2.2. Calibration

For *HST* data, the calibrated fits files in the MAST archive were retrieved. This is the only step needed, except for observations with the STIS-G140M grating and central wavelength 1222 Å, where a 1-pixel shift seems necessary (see Wakker & Savage 2009). That conclusion is based on fourteen sightlines with good data and relatively simple ISM absorption lines. For these sightlines the S II λ1250.584, 1253.811 lines can be fit both in a G140M spectrum centered on 1222 Å and in one centered on 1272 Å, and sometimes also in an E140M spectrum. To align the lines in the 1222 Å-centered spectrum with those in the other spectra, an average redward shift of 12 $\mathrm{km\,s^{-1}}$ is needed, which corresponds to one pixel.

Finally, for observations with the STIS-E140M echelle, the MAST fits files give the data for each of the 42 orders separately. These orders were combined into a single spectrum by interpolating the photon counts and errors onto a common grid, adding the photon counts and converting back to a flux.

The processing of the *FUSE* data was described in detail by Wakker et al. (2003) and Wakker (2006), and therefore only a summary is given here. First, the spectra were calibrated using v2.1 or v2.4 of the *FUSE* calibration pipeline. To correct for residual wavelength shifts, the central velocities of the Milky Way interstellar lines were determined for each detector segment (LiF1A/1B/2A/2B, SiC2A/2B) of each individual observation. The *FUSE* segments were then aligned with the LSR interstellar velocities implied by the STIS-E140M spectra, or, if no E140M data were available, with the LSR velocity of the strongest component in the 21-cm H I spectrum. For targets with a STIS-E140M spectrum, the interstellar reference velocity was determined by fitting all Milky Way lines in that spectrum; the STIS wavelength calibration is accurate to about 1 $\mathrm{km\,s^{-1}}$ (Kim-Quijano et al. 2007). For sightlines with S/N>10 near 1031 Å, the resulting shifts were given by Wakker (2006). Using these shifts, LiF1A and LiF2B data are added together to produce the final spectrum for each target. The final velocity scale references the velocities to the Local Standard of Rest (LSR).

2.3. Presentation of spectra

We present the Galactic high-ionization absorption lines for six sightlines in Figure 2. These sightlines illustrate each of the items mentioned in the figure caption. The entire set of spectra is available in the electronic version of this paper. The plots include the available data for the O VI, N V, C IV and Si IV doublets, as well as their apparent column density profiles. Note that we regridded the spectra to 10 $\mathrm{km\,s^{-1}}$ velocity bins for this figure. This

does not affect the *FUSE* or STIS-G140M data, but does slightly degrade the STIS-E140M spectra (enhancing their S/N ratio). The apparent column density is defined as:

$$N_a(v) = \frac{m_e c}{\pi e^2} \, f \, \lambda \, \ln \frac{C(v)}{F(v)},$$

with $F(v)$ the observed profile, $C(v)$ the fitted continuum and f the oscillator strength. In addition, to allow comparing the kinematics of the high-ionization lines with those of lower ionization gas, we show a representative strong and weak line of an intermediate- and a low-ionization species, as described in the figure caption.

We also show profiles of the ratios between different ions. These are derived from the apparent column density profiles and their errors. We display the ionic ratio only in the range of velocities where it is larger than the error in this ratio, and only for sightlines and line-combinations where both doublet lines of the various ions were detected at a significant level.

We show the actual spectra in Fig. 2, i.e. they are not normalized relative to the continuum. However, for each absorption line we chose a vertical scale that places the continuum at about 80% of the maximum. For the apparent column density and ratio profiles, we use the same vertical scale for each ion throughout, to allow easy comparisons of the relative strength of the lines between different sightlines.

A sightline of note is NGC 4151 (spectra available in the electronic version of this paper). Here the O VI lines appears offset from all other absorption lines, which *do* line up with each other, even showing a component between -100 and -60 km s^{-1} in C IV, Si III and C II. There is no problem with the velocity calibration, as the Galactic H$_2$ absorption lines near O VI λ1031.926 are fitted perfectly well. The most likely explanation is that the O VI absorption between $v_{\rm LSR}$=25 and 60 km s^{-1} is related to the strong P-Cygni profile produced by the outflowing gas in NGC 4151 itself. We include the measurements for most ions in this sightline, but we exclude the O VI lines.

We note that in all cases the profiles of the high-ionization species cover a similar range of velocities. In all but a few cases (PG 1116+215, PKS 2155$-$304; see electronic version) the shapes and velocity extent of the intermediate-ionization lines (i.e. Si III and Fe III) follow that of the high-ionization lines. On the other hand, the strong low-ionization absorption lines tend to be narrower than the high-ionization absorption lines. The weak low-ionization lines (usually exemplified by S II λ1250.584) often show clear component structure, which is usually, but not always reflected in the high-ionization absorption (contrast e.g. ESO 141$-$G55, Mrk 205, PG 1302$-$102 to 3C 273.0, Mrk 509, PG 1116+215 and PKS 2005$-$489). Sometimes there is a narrow low-ionization component near $v\sim$0 km s^{-1},

with no absorption at higher velocities, where there is strong high-ionization absorption (e.g. toward HE 0226−4110 and Mrk 509).

3. Measurements

The Galactic high-ionization lines tend not to have simple gaussian profiles, but rather they typically appear to be a mixture of several broad, blended components. Since the typical optical depth of the lines is on the order of 1–2, and since we can only measure two lines for each ion, it is not advisable to estimate column densities by converting an equivalent width measurement into a column density or applying a curve-of-growth method. We also do not resort to fitting components to the line profiles as the signal-to-noise ratio is often low ($\sim$10–15), the profiles are usually asymmetric, and the component structure is not always clear. Profile fits would give formally correct results, and would allow us to calculate the total column density accurately, but the fitted central velocities and widths of the gaussian components would more often than not be misleading, as a good fit would require several components, which usually cannot be defined unambiguously.

Because of these considerations, we instead integrated the apparent column density ($N_a(v)$) profiles (Savage & Sembach 1991). For resolved and unsaturated lines this represents the true column density distribution of the ion, broadened by the instrumental profile. If the $N_a(v)$ profiles of the two members of each doublet match, then one can conclude that there is no unresolved saturation. In practice we find that this is a good assumption for the Galactic high-ionization lines, as the resulting column densities always match to within the errors (with one exception, see below).

To derive the column density profiles, we first fitted a local continuum to each of the absorption lines. To do this, we started by selecting line-free regions in a window about ±1000 km s^{-1} wide around each line and then fitted a first, second or third order Legendre polynomial to these points, following the method of Sembach & Savage (1992). In addition, a model for the molecular hydrogen absorption is applied, using the H$_2$ column densities found by Wakker (2006). Any associated H$_2$ optical depth is removed from the apparent optical depth profile. This is mostly important for the O VI λ1031.926 line, while for O VI λ1037.617 and S III λ1012.501 the H$_2$ contamination is often too large to be removed reliably. We only list the results for those two lines if the contamination is sufficiently minor. In some sightlines we list the measurements of H$_2$-decontaminated O VI lines, but do not use them for the analyses.

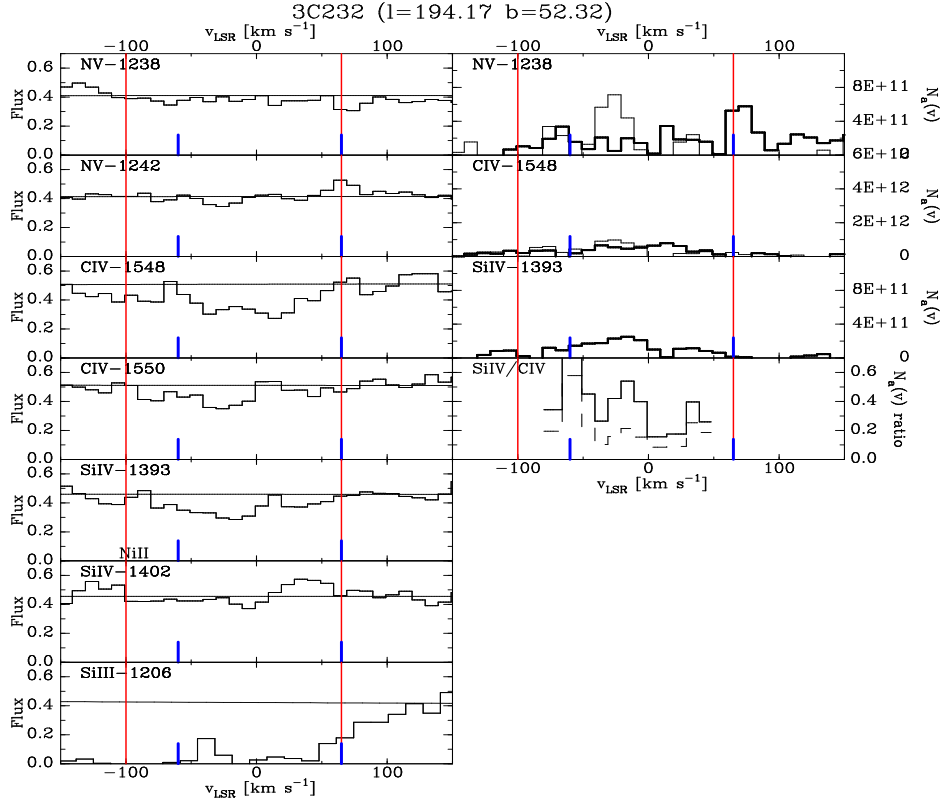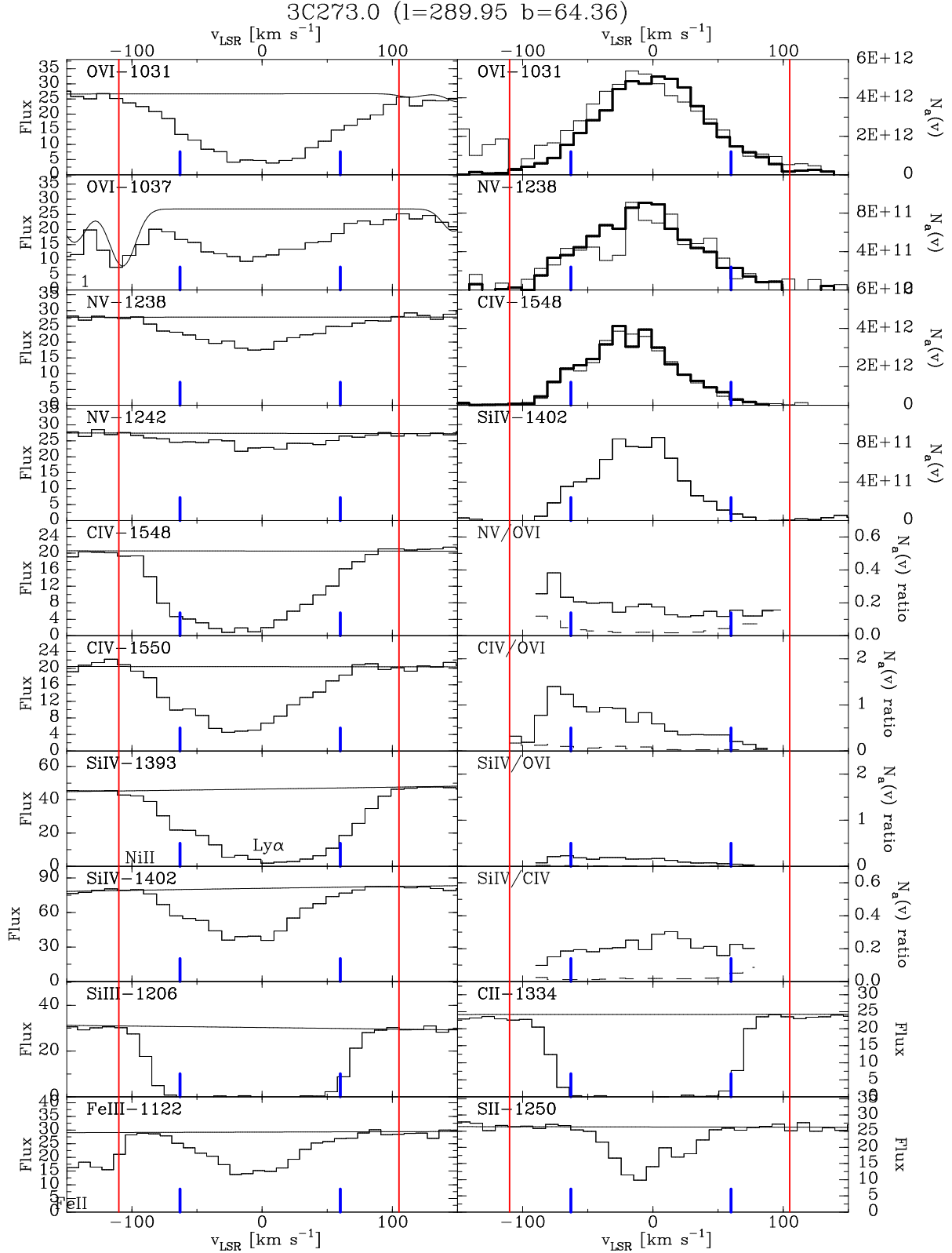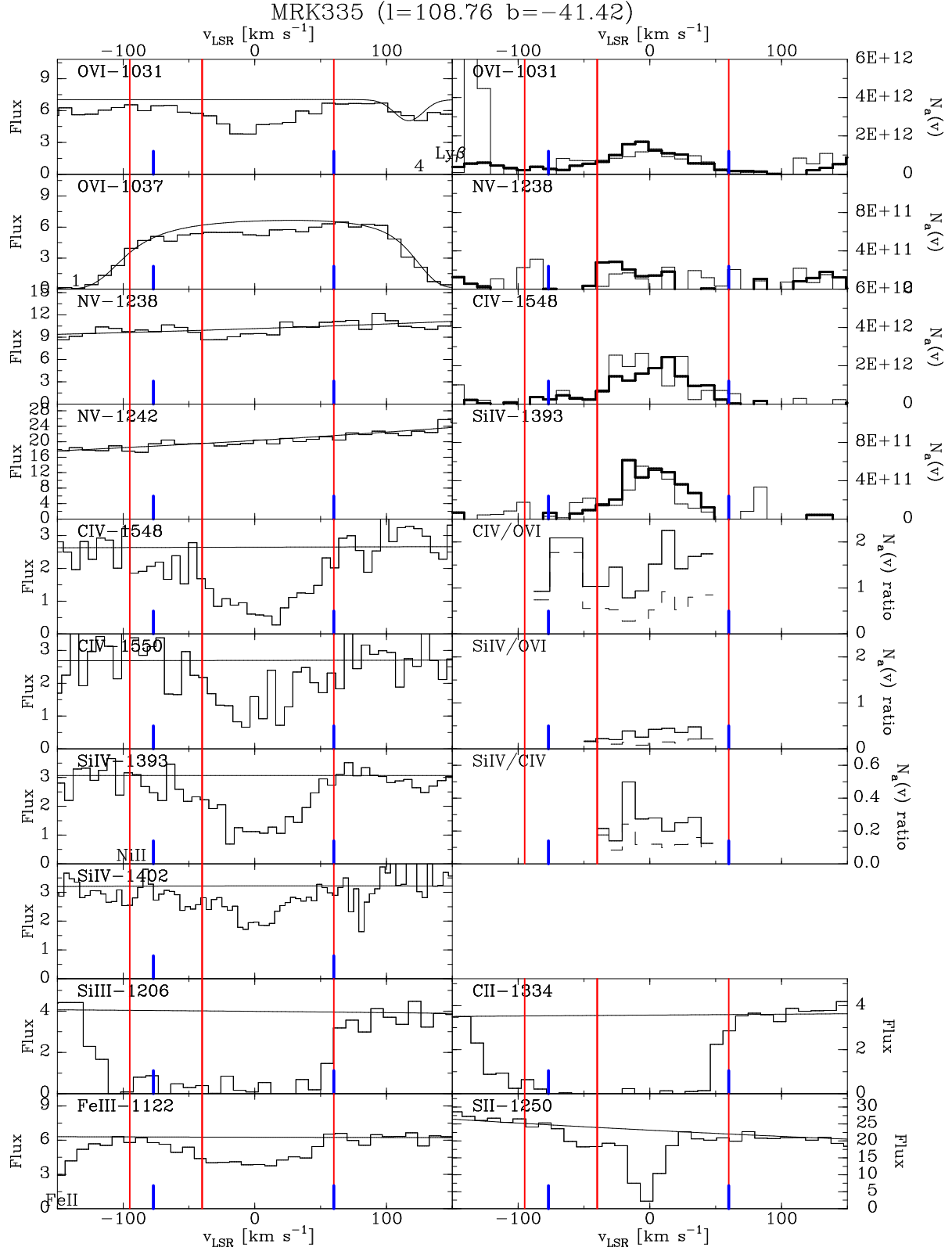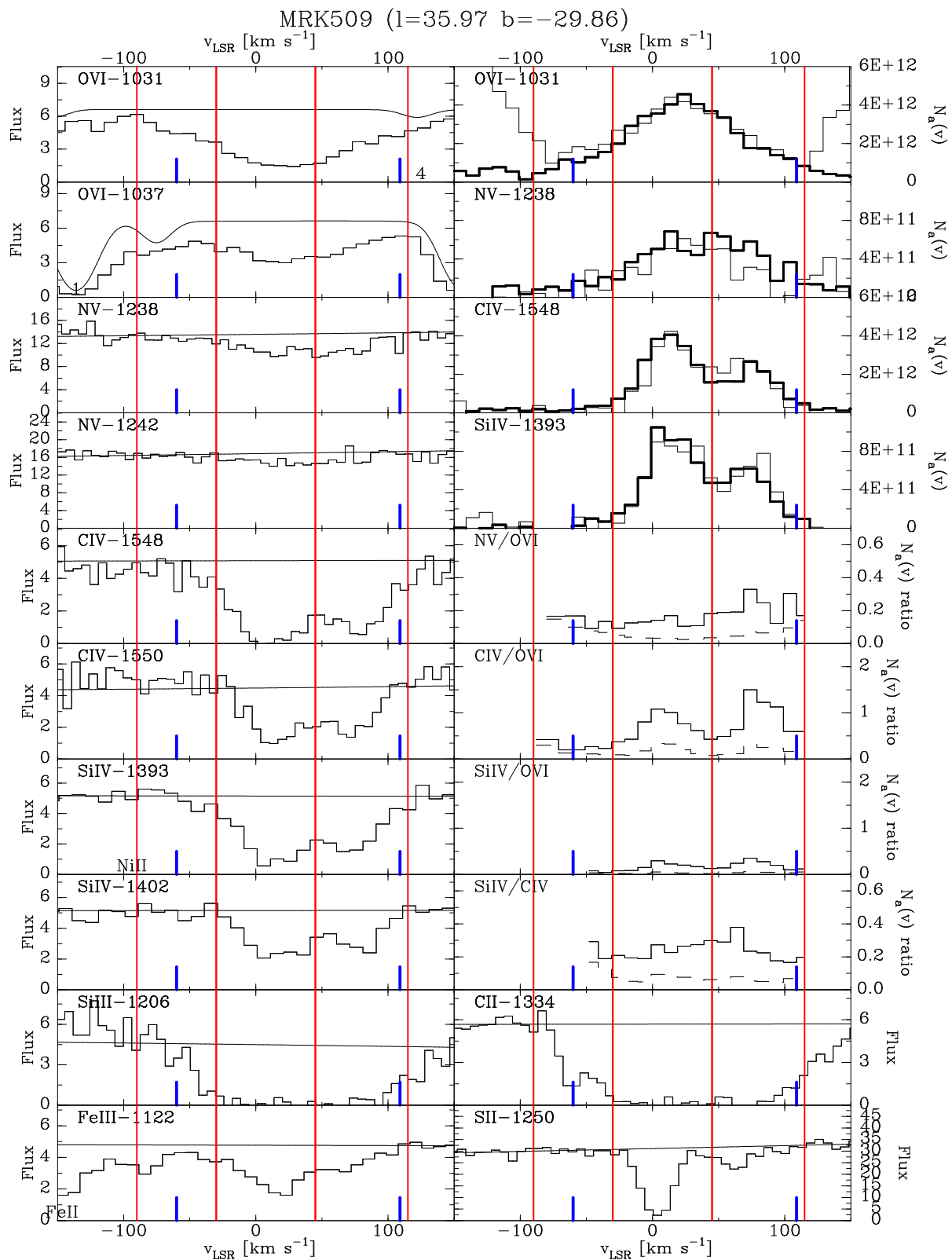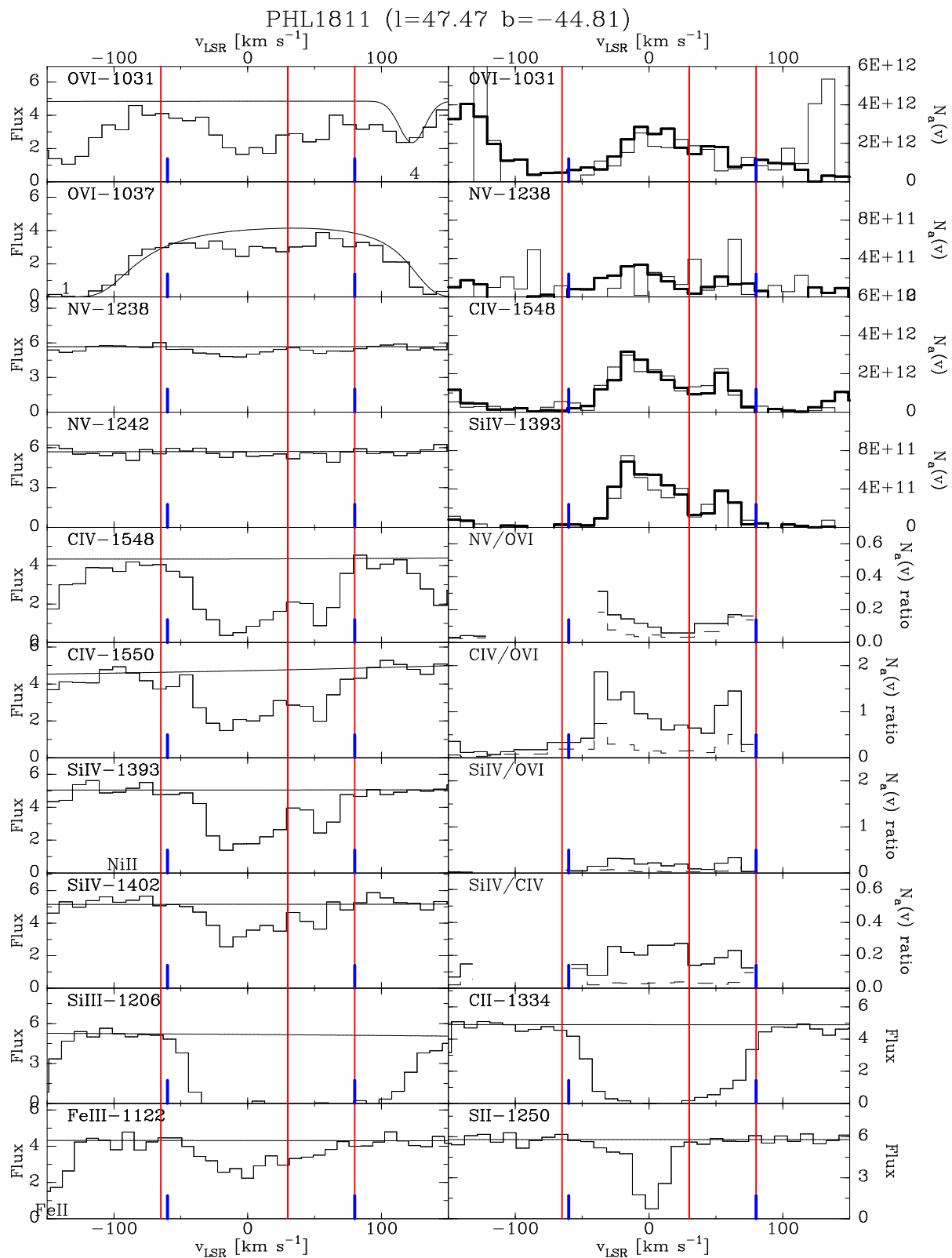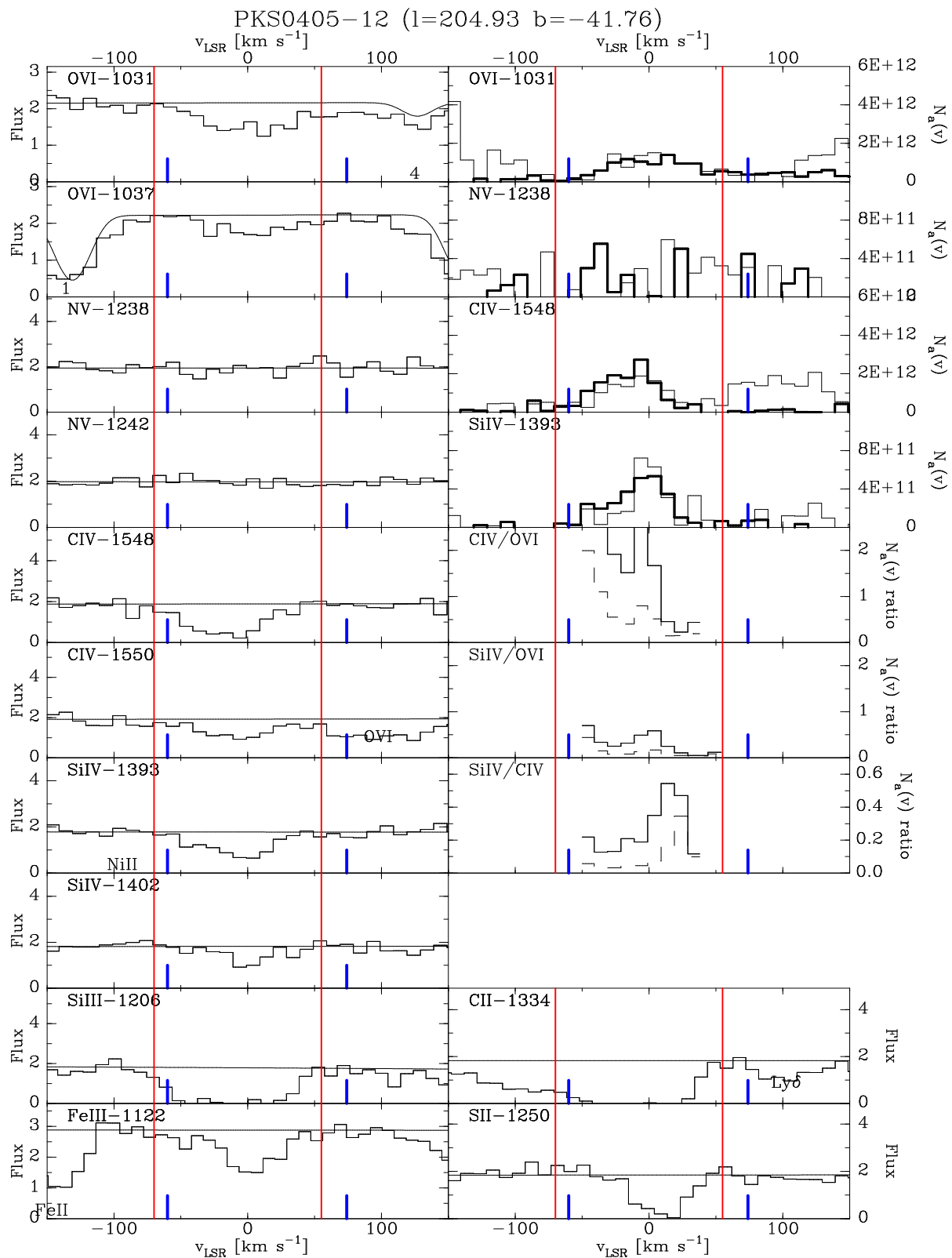We visually determined the velocity extent of the absorption associated with the Milky

Fig. 2a.— The panels show the available data for the four high-ionization lines, as well as for a strong and a weak intermediate-ionization and a strong and weak low-ionization line (when data is available). The panels on the left give the spectra for the high-ionization lines, as shown by the labels. The top set of panels on the right shows the apparent optical depth profiles for the high-ionization species, with the stronger absorption line shown as thick lines. No apparent optical depth profiles are shown for lines that were deemed unmeasurable, even though a panel is always shown if data were present. Below the optical depth profiles are panels showing the ratios between two ions, but only in spectral regions where the S/N in the ratio is >3 in a 10 km s^{-1} velocity bin. Strong intermediate ionization is represented by Si III (or by C III when Si III is not available). Weak intermediate ionization is given by Fe III. The strong low-ionization line is either C II λ1334.532 or C II λ1036.337, while the weak low-ionization line is S II λ1250.584 or Ar I λ1048.220. The intermediate- and low-ionization lines are always given in the bottom one or two panels. Line identifications are given at the top left of each panel. The continuum fit (including a model for H$_2$ absorption) is also shown. In a few cases (e.g. for O VI λ1037.617 toward Mrk 509), the continuum looks much higher than the data, because it was fit through pixels far outside the displayed range of velocities. All spectra were rebinned to 10 km s^{-1} pixels. Other absorption lines in each spectral window are identified by labels near the bottom of each panel. The short vertical blue lines show the range of velocities within 60 km s^{-1} of those consistent with standard Galactic differential rotation (see Section 4.2 for the justification of this number). The red vertical lines indicate the velocity limits of integration for the different Galactic components. Note that a figure is available for each sightline in the on-line version of this paper.

3C273.0 (l=289.95 b=64.36)

MRK335 (l=108.76 b=−41.42)

MRK509 (l=35.97 b=−29.86)

PHL1811 (l=47.47 b=−44.81)

PKS0405−12 (l=204.93 b=−41.76)

Way Thick Disk. In many sightlines absorption occurs at velocities more negative than $-80\ \mathrm{km\,s^{-1}}$ or more positive than $80\ \mathrm{km\,s^{-1}}$. This high-velocity absorption was analyzed by Sembach et al. (2003). It is often associated with known 21-cm H I high-velocity clouds, which trace the accretion of low-metallicity material and tidal streams (Wakker et al. 1999, 2007; Richter 2006). In this paper we concentrate on the high-ionization absorption associated with the gas at velocities below about $80\ \mathrm{km\,s^{-1}}$, which originates in the Disk and lower Galactic halo (i.e. the Thick Disk). An analysis of the high-velocity gas is deferred to the future.

Next, we looked at the structure of all absorption lines toward each target and used the visual appearance of each profile and the comparison between the profiles for different ions (high-, intermediate and low-ionization species) to decide whether one can discern individual components and in which velocity ranges these occur. The structure in the low-ionization lines is taken into consideration for the determinations, but it does not drive the resulting interpretation for the high-ionization line component structure. We also noted cases where the line of the highly-ionized species is blended with other galactic or intergalactic absorption lines.

We then integrated the $N_a(v)$ profile, both over the full velocity range over which we think absorption originates in the Thick Disk, and over the different selected velocity ranges for each individual component. For each $N_a(v)$ integration we determined a statistical and a systematic error, following the methods described by Wakker et al. (2003). The statistical error combines the Poisson noise, detector background and continuum placement, while the systematic error takes into account the placement of integration limits and fixed-pattern noise. We flagged the cases where we judged it possible to derive reasonable values for line ratios.

We also calculated a central velocity (v_0) and FWHM (W, full width at half maximum, $W = \sqrt{4\ln 2}\,b$, where b is the Doppler parameter) linewidth from the first and second moments of the $N_a(v)$ profile. For the analyses we also correct the derived FWHMs for instrumental broadening (see notes to Table 2 for details).

$$N = \int N_a(v)dv,$$

$$v_0 = [\int v N_a(v)dv]/[\int N_a(v)dv],$$

$$W = \sqrt{(4\ln 2)}\left([\int (v-v_0)^2 N_a(v)dv]/[\int N_a(v)dv]\right)^2.$$

We applied our best judgments to determine whether the resulting values are likely to represent a real width, as opposed to just being set by the center and width of the integration

range. Only in about half of the sightlines were the individual components separated clearly enough to derive individual velocities and widths. However, for the full Thick Disk integration we can derive a column density weighted average velocity and width in almost all cases.

We checked all doublet measurements for consistency. The two measurements for each half of each doublet were deemed to be compatible if the column density difference was less than the sum of the statistical and systematic errors for each individual component. For example, for the -110 to $+105$ $km\,s^{-1}$ integration toward 3C 273.0, the N V lines give column densities of $13.94\pm0.02\pm0.01$ and $13.90\pm0.03\pm0.01$. As 13.94 and 13.90 are closer together than $0.02+0.01+0.03+0.01=0.07$ dex, these two values are deemed compatible. We justify adding the errors linearly instead of in quadrature by noting that just by chance the measurement for a particular line will be more than 1σ above (or below) the real value in 16% of the cases. In 16% of those cases the measurement of the other line of the doublet will be more than 1σ off in the other direction. Thus, with 258 cases where we measure both members of a doublet, we expect 6.6 cases where the column densities implied by the two member of the doublet differ by more than the sum of the errors. We find seven such cases; in four of these the excess the difference is just 0.01 dex. In only one case do the two lines of the doublet suggest the presence of saturation. This is for the C IV lines in the direction toward ESO 141$-$G55, which are very deep, resulting in a factor 2 difference in the column densities derived from the two members of the doublet. Since our check shows that in all but one case the absorption lines are unlikely to be saturated, we estimated final values for the ionic column densities by averaging the measurements toward the two lines of the doublet, if both measurements were deemed to be useful. There is one exception: for the saturated C IV line toward ESO 141$-$G55, we instead used the rule-of-thumb derived by Sembach & Savage (1991) that log N(ion)$= 2\,$log$N$(weak) $-$ log N(strong).

The resulting measurements are presented in Table 2. This table shows for each target, and for each component, the measured column densities in each high-ionization line, as well as the central velocities, widths and ratios for those cases where the result was deemed to be reasonably reliable. Note that the widths that we list are corrected for instrumental broadening (see notes for details).

We compared our values to those listed by Savage et al. (1997b) in their earlier study of highly-ionized atoms toward extragalactic targets and find that for the most part our measurements of N V and C IV column densities are the same within the errors. There are two exceptions: (a) H 1821+643, for which Savage et al. (1997b) had not realized that there is strong contamination associated with the nearby planetary nebula K1-16, and (b) PKS 2155$-$304, for which we concluded that the N V λ1238.821 line is contaminated by an

intergalactic Lyα line because the two lines of the doublet do not match, and the absorption that might be Galactic N V extends to much more negative velocities than is the case for the other high-ionization lines.

We also checked our measurements against the numbers presented by Indebetouw & Shull (2004b). To make their measurements, they integrated all of the high-ionization absorption, mixing together high-velocity clouds and Milky Way Thick Disk components. In a few cases they did not remove blending intergalactic absorption and they did not remove the absorption associated with the planetary nebula K1-16 near the H 1821+643 sightline. Furthermore, their velocity limits are often inconsistent with our judgments. Also, in many cases the column densities they give for the two lines in a N V or C IV doublet are often rather different, sometimes by as much as 0.3 dex. In addition, the column density errors in their table are much larger than what we found (typically they are listed as 0.2–0.6 dex). Finally, in sightlines where there are no high-velocity clouds or other problems the column densities listed by Indebetouw & Shull (2004b) still usually differ from our results. Due to all these issues, we did not make a detailed comparison of our results to the measurements given by Indebetouw & Shull (2004b).

Table 2.   Measurements[a]

Object	vel. range	ion	strong line			weak line			ratios	
	km s^{-1}]		$\log N$ [cm^{-2}]	$<v>$ [km s^{-1}]	FWHM [km s^{-1}]	$\log N$ [cm^{-2}]	$<v>$ [km s^{-1}]	FWHM [km s^{-1}]	ions	log ratio
(1)	(2)	(3)	(4)	(5)	(6)	(7)	(8)	(9)	(10)	(11)
3C249.1	−100:70	OVI	14.38±0.03±0.01			[14.36±0.05±0.17]				
		NV	<13.32			[Lyα]			NV/OVI	<−1.06
		CIV	13.86±0.04±0.01	−38±2	68±7	13.85±0.08±0.01	−35±2	75±7	CIV/OVI	−0.52±0.09
		SiIV	13.39±0.03±0.01	−40±1	58±6	[Lyα]			SiIV/CIV	−0.47±0.09
		FeIII	14.27±0.05±0.01	−39±3	72±7				FeIII/CIV	0.41±0.10
		SIII	[H$_2$]							
	−100:−30	OVI	14.10±0.04±0.02			[14.18±0.05±0.19]				
		NV	<13.05			[Lyα]			NV/OVI	<−1.05
		CIV	13.68±0.04±0.01	−56±5	37±6	13.65±0.08±0.01			CIV/OVI	−0.44±0.10
		SiIV	13.21±0.03±0.02	−55±6	41±9	[Lyα]			SiIV/CIV	−0.45±0.09
		FeIII	14.11±0.05±0.02						FeIII/CIV	0.45±0.10
		SIII	[H$_2$]							
	−30:20	OVI	13.94±0.04±0.03			[13.80±0.09±0.11]				
		NV	<13.00			[Lyα]			NV/OVI	<−0.94
		CIV	13.41±0.05±0.02			13.42±0.10±0.02			CIV/OVI	−0.53±0.12
		SiIV	13.03±0.04±0.02			[Lyα]			SiIV/CIV	−0.38±0.12
		FeIII	13.79±0.08±0.04						FeIII/CIV	0.38±0.14
		SIII	[H$_2$]							
	20:70	OVI	13.50±0.09±0.04			[13.59±0.02±0.01]				
		NV	<13.06			[Lyα]			NV/OVI	<−0.44
		CIV	<12.88			<13.25			CIV/OVI	<−0.62
		SiIV	<12.31			<12.66				
		FeIII	<13.49							
		SIII	[H$_2$]							
3C273.0	−110:105	OVI	14.73±0.02±0.01			[H$_2$]				
		NV	13.94±0.02±0.01	−8±1	94±4	13.90±0.03±0.01	−6±2	101±6	NV/OVI	−0.81±0.04
		CIV	14.51±0.02±0.01			14.50±0.02±0.01			CIV/OVI	−0.22±0.04
		SiIV	[Lyα]			13.85±0.02±0.01	−13±1	76±4	SiIV/CIV	−0.66±0.04
		FeIII	14.38±0.02±0.02	−9±7	83±15				FeIII/CIV	−0.13±0.04
		SIII	14.63±0.02±0.09	−3±5	88±8				SIII/CIV	0.12±0.04
3C351.0	−60:35	OVI	[No flux]			[No flux]				
		NV	13.63±0.05±0.01	−18±4	43±9	13.60±0.09±0.02				
		CIV	13.96±0.02±0.01	−19±4	54±4	14.02±0.04±0.01	−18±4	54±4		
		SiIV	13.29±0.02±0.01	−17±4	52±3	13.33±0.04±0.04	−18±13	55±9	SiIV/CIV	−0.68±0.06
		FeIII	[Lyκ]							
		SIII	[No flux]							
ESO141−G55	−110:85	OVI	14.51±0.02±0.01	0±2	85±5	14.58±0.03±0.17				
		NV	13.67±0.06±0.01	−4±3	95±8	13.77±0.08±0.01	2±6	93±12	NV/OVI	−0.82±0.11
		CIV	14.31±0.06±0.01			14.54±0.06±0.01	−8±2	98±3	CIV/OVI	0.11±0.09
		SiIV	13.82±0.05±0.01	−2±2	86±5	13.90±0.05±0.01	−2±2	87±5	SiIV/CIV	−0.79±0.11
		FeIII	[FeII]							
		SIII	[H$_2$]							

Table 2—Continued

Object	vel. range	ion	strong line			weak line			ratios	
			$\log N$ [cm^{-2}]	$<v>$ [km s^{-1}]	FWHM [km s^{-1}]	$\log N$ [cm^{-2}]	$<v>$ [km s^{-1}]	FWHM [km s^{-1}]	ions	log ratio
(1)	[km s^{-1}] (2)	(3)	(4)	(5)	(6)	(7)	(8)	(9)	(10)	(11)
	−110:−30	OVI	13.83±0.05±0.05	−56±8	35±7	14.05±0.05±0.29				
		NV	13.06±0.14±0.05	−58±9	44±12	<13.33			NV/OVI	−0.88±0.16
		CIV	13.84±0.07±0.01	−55±7	39±9	14.00±0.06±0.01	−62±7	45±6	CIV/OVI	0.14±0.11
		SiIV	13.13±0.06±0.02			13.19±0.09±0.03			SiIV/CIV	−0.92±0.14
		FeIII	[FeII]							
		SIII	[H$_2$]							
	−30:30	OVI	14.30±0.03±0.02	4±5	32±2	14.26±0.03±0.07				
		NV	13.42±0.07±0.02			13.48±0.09±0.03			NV/OVI	−0.83±0.12
		CIV	14.00±0.11±0.02	0±8	39±2	14.28±0.09±0.01	1±5	34±2	CIV/OVI	0.14±0.15
		SiIV	13.60±0.08±0.01	1±5	34±2	13.69±0.06±0.01	0±5	33±2	SiIV/CIV	−0.78±0.17
		FeIII	14.21±0.03±0.03	3±4	28±3				FeIII/CIV	−0.21±0.14
		SIII	[H$_2$]							
	30:85	OVI	13.84±0.04±0.06			13.99±0.05±0.12				
		NV	13.00±0.13±0.05			13.24±0.13±0.05			NV/OVI	−0.79±0.19
		CIV	13.63±0.08±0.03			13.81±0.08±0.03			CIV/OVI	−0.01±0.13
		SiIV	13.15±0.07±0.03			13.22±0.08±0.03			SiIV/CIV	−0.71±0.16
		FeIII	13.72±0.06±0.08	46±6	21±5				FeIII/CIV	−0.18±0.13
		SIII	[H$_2$]							
Fairall9	−60:70	OVI	14.18±0.10±0.04			[H$_2$]				
		NV	<13.34			<13.62			NV/OVI	<−0.84
		CIV	14.04±0.10±0.01	−1±2	70±3	14.26±0.07±0.01	0±4	76±2	CIV/OVI	−0.03±0.16
		FeIII	<14.17						FeIII/CIV	< 0.02
		SIII	<14.69						SIII/CIV	< 0.54
	−60:0	OVI	[H$_2$]			<14.04				
		NV	<13.24			<13.45				
		CIV	13.78±0.13±0.02	−26±4	30±4	14.03±0.10±0.02	−24±5	31±4	CIV/OVI	>−0.14
		FeIII	<13.99						FeIII/CIV	< 0.09
		SIII	<14.48						SIII/CIV	< 0.58
	0:70	OVI	14.18±0.09±0.03	37±4	35±2	[H$_2$]				
		NV	<13.26			<13.46			NV/OVI	<−0.92
		CIV	13.72±0.12±0.02	27±6	33±4	13.88±0.09±0.03	34±9	42±5	CIV/OVI	−0.38±0.17
		FeIII	<14.05						FeIII/CIV	< 0.25
		SIII	<14.52						SIII/CIV	< 0.72
HE0226−4110	−60:40	OVI	[Lyγ]			13.95±0.07±0.02	0±3	43±4		
		NV	<13.14			<13.42			NV/OVI	<−0.81
		CIV	[OVI]			13.94±0.05±0.01	−7±1	50±4	CIV/OVI	−0.01±0.09
		SiIV	13.38±0.03±0.01	−7±2	48±3	13.40±0.05±0.01	−5±2	42±9	SiIV/CIV	−0.55±0.08
		FeIII	13.63±0.08±0.03	−4±5	28±11				FeIII/CIV	−0.31±0.09
		SIII	14.16±0.09±0.03	−2±1	27±8				SIII/CIV	0.22±0.10
	−60:−20	OVI	[Lyγ]			<13.43				
		NV	<12.88			<13.21				
		CIV	[OVI]			13.44±0.09±0.03			CIV/OVI	> 0.01

Table 2—Continued

Object (1)	vel. range [km s⁻¹] (2)	ion (3)	strong line log N [cm⁻²] (4)	<v> [km s⁻¹] (5)	FWHM [km s⁻¹] (6)	weak line log N [cm⁻²] (7)	<v> [km s⁻¹] (8)	FWHM [km s⁻¹] (9)	ratios ions (10)	log ratio (11)
		SiIV	12.88±0.04±0.02			12.79±0.09±0.06			SiIV/CIV	−0.60±0.13
		FeIII	<13.20						FeIII/CIV	<−0.24
		SIII	<13.73						SIII/CIV	< 0.29
	−20:40	OVI	[Lyγ]			13.89±0.06±0.02	5±5	30±3		
		NV	<13.05			<13.28			NV/OVI	<−0.84
		CIV	[OVI]			13.80±0.05±0.01	4±6	34±3	CIV/OVI	−0.09±0.08
		SiIV	13.23±0.03±0.01	4±5	28±4	13.30±0.05±0.02			SiIV/CIV	−0.53±0.08
		FeIII	13.65±0.07±0.03	0±4	26±5				FeIII/CIV	−0.15±0.09
		SIII	14.14±0.07±0.04	0±3	27±6				SIII/CIV	0.34±0.09
HE0340−2703	−70:60	NV	<13.24			<13.56				
HE1029−1401	−20:70	NV	13.39±0.03±0.03			13.35±0.05±0.06				
HE1228+0131	−60:60	OVI	[Lyβ]			[Unid. Contam.]				
		NV	13.62±0.09±0.02			<13.74				
		CIV	14.28±0.05±0.01	−4±2	58±4	14.35±0.04±0.01	−5±2	63±2		
		SiIV	13.47±0.03±0.01	−4±1	51±5	13.30±0.08±0.01	−4±3	43±14	SiIV/CIV	−0.93±0.11
		FeIII	14.28±0.09±0.03	7±7	61±10				FeIII/CIV	−0.03±0.11
		SIII	<14.66						SIII/CIV	< 0.35
HS0624+6907	−90:35	OVI	14.44±0.04±0.01	−29±3	65±5	[H₂]				
		NV	13.55±0.07±0.01			<13.52			NV/OVI	−0.89±0.08
		CIV	13.95±0.02±0.01			13.80±0.07±0.01			CIV/OVI	−0.56±0.08
		SiIV	13.52±0.02±0.01			13.58±0.02±0.01			SiIV/CIV	−0.33±0.08
		FeIII	14.44±0.04±0.02	−33±3	57±6				FeIII/CIV	0.56±0.08
		SIII	[H₂]							
	−90:−20	OVI	14.19±0.05±0.04			[H₂]				
		NV	13.48±0.06±0.02			<13.41			NV/OVI	−0.71±0.08
		CIV	13.85±0.02±0.02	−55±0	44±2	13.76±0.06±0.02	−54±8	46±3	CIV/OVI	−0.39±0.08
		SiIV	13.46±0.02±0.02	−55±0	39±3	13.48±0.02±0.02	−54±4	35±4	SiIV/CIV	−0.33±0.07
		FeIII	14.27±0.04±0.05						FeIII/CIV	0.47±0.07
		SIII	[H₂]							
	−20:35	OVI	14.11±0.07±0.05			[H₂]				
		NV	<13.03			<13.31			NV/OVI	<−1.08
		CIV	13.27±0.06±0.04	5±9	38±2	<13.25				
		SiIV	12.65±0.06±0.04	2±9	28±5	12.92±0.06±0.03	11±8	35±5		
		FeIII	13.97±0.07±0.09							
		SIII	[H₂]							
MCG+10−16−111	−120:20	NV	13.35±0.04±0.02	−45±3	80±3	[Unid. Contam.]				
MRC2251−178	−55:70	OVI	14.08±0.06±0.03	0±8	76±5	14.04±0.15±0.05	4±8	71±6		
		NV	<12.80			<13.06			NV/OVI	<−1.26
		FeIII	14.20±0.05±0.03	11±4	65±4					
		SIII	[H₂]							
Mrk110	−70:60	NV	13.37±0.10±0.03			<13.47				
Mrk205	−95:50	OVI	14.16±0.04±0.02			14.21±0.06±0.03				

Table 2—Continued

Object	vel. range	ion	strong line			weak line			ratios	
	$\mathrm{km\,s^{-1}}$]		$\log N$ $[\mathrm{cm^{-2}}]$	$<v>$ $[\mathrm{km\,s^{-1}}]$	FWHM $[\mathrm{km\,s^{-1}}]$	$\log N$ $[\mathrm{cm^{-2}}]$	$<v>$ $[\mathrm{km\,s^{-1}}]$	FWHM $[\mathrm{km\,s^{-1}}]$	ions	log ratio
(1)	(2)	(3)	(4)	(5)	(6)	(7)	(8)	(9)	(10)	(11)
		NV	13.26±0.12±0.01			<13.55				
		CIV	14.11±0.03±0.01			14.07±0.05±0.01			CIV/OVI	−0.10±0.09
		SiIV	13.57±0.02±0.01			13.55±0.04±0.01			SiIV/CIV	−0.53±0.07
		FeIII	14.47±0.03±0.01						FeIII/CIV	0.38±0.07
		SIII	14.72±0.04±0.07						SIII/CIV	0.63±0.07
	−95:−30	OVI	13.87±0.05±0.04			14.03±0.06±0.05				
		NV	13.21±0.09±0.01	−56±3	31±9	<13.34			NV/OVI	−0.74±0.12
		CIV	13.93±0.03±0.01			13.81±0.07±0.01	−56±7	39±4	CIV/OVI	−0.08±0.11
		SiIV	13.40±0.03±0.01	−57±5	32±5	13.37±0.03±0.01	−51±4	27±10	SiIV/CIV	−0.49±0.09
		FeIII	14.34±0.03±0.02	−58±4	26±5				FeIII/CIV	0.47±0.09
		SIII	14.49±0.05±0.06	−57±6	28±5				SIII/CIV	0.62±0.09
	−30:50	OVI	13.86±0.05±0.04	4±6	45±2	13.74±0.11±0.09	2±7	40±6		
		NV	<13.09			<13.40			NV/OVI	<−0.71
		CIV	13.66±0.04±0.02	0±8	41±5	13.73±0.08±0.02			CIV/OVI	−0.10±0.15
		SiIV	13.12±0.04±0.01			13.10±0.07±0.02			SiIV/CIV	−0.59±0.12
		FeIII	13.90±0.05±0.05						FeIII/CIV	0.20±0.10
		SIII	14.37±0.07±0.17						SIII/CIV	0.67±0.11
Mrk279	−110:65	OVI	14.41±0.02±0.01	−24±3	91±4	14.41±0.02±0.01	−26±3	88±5		
		NV	13.26±0.05±0.01	−6±3	77±7	13.35±0.07±0.01	−14±5	89±10		
		CIV	14.24±0.02±0.01	−25±1	74±4	14.20±0.02±0.01	−30±1	70±4		
		SiIV	13.66±0.02±0.01	−24±1	62±4	13.66±0.02±0.01	−23±2	78±3		
		FeIII	14.33±0.02±0.01	−33±2	61±6					
		SIII	14.55±0.02±0.04	−32±1	57±8					
	−110:−65	OVI	13.67±0.02±0.04			13.67±0.04±0.05				
		NV	<12.43			<12.71			NV/OVI	<−1.24
		CIV	13.19±0.04±0.04			13.24±0.07±0.04			CIV/OVI	−0.46±0.09
		SiIV	12.40±0.05±0.05			12.57±0.09±0.04			SiIV/CIV	−0.73±0.13
		FeIII	13.37±0.05±0.08						FeIII/CIV	0.16±0.09
		SIII	13.58±0.08±0.09						SIII/CIV	0.37±0.11
	−65:−20	OVI	13.95±0.02±0.03			13.98±0.02±0.03				
		NV	12.79±0.06±0.03			12.84±0.09±0.03			NV/OVI	−1.15±0.11
		CIV	13.97±0.02±0.01			13.93±0.02±0.02			CIV/OVI	−0.01±0.04
		SiIV	13.43±0.02±0.01	−38±5	26±4	13.39±0.02±0.01			SiIV/CIV	−0.54±0.04
		FeIII	14.10±0.02±0.02						FeIII/CIV	0.15±0.04
		SIII	14.32±0.02±0.03						SIII/CIV	0.37±0.04
	−20:20	OVI	13.98±0.02±0.03			13.98±0.02±0.03				
		NV	12.93±0.04±0.03			13.01±0.06±0.03			NV/OVI	−1.01±0.08
		CIV	13.74±0.02±0.03			13.74±0.02±0.02			CIV/OVI	−0.24±0.04
		SiIV	13.20±0.02±0.03			13.13±0.02±0.03			SiIV/CIV	−0.58±0.04
		FeIII	13.79±0.02±0.04						FeIII/CIV	0.05±0.04
		SIII	14.10±0.03±0.05						SIII/CIV	0.36±0.04
	20:65	OVI	13.60±0.03±0.04			13.49±0.06±0.06				

Table 2—Continued

Object (1)	vel. range [km s⁻¹] (2)	ion (3)	strong line log N [cm⁻²] (4)	strong line < v > [km s⁻¹] (5)	strong line FWHM [km s⁻¹] (6)	weak line log N [cm⁻²] (7)	weak line < v > [km s⁻¹] (8)	weak line FWHM [km s⁻¹] (9)	ratios ions (10)	ratios log ratio (11)
		NV	12.64±0.08±0.03			<12.69			NV/OVI	−0.90±0.11
		CIV	13.20±0.03±0.03			[12.88±0.13±0.05]			CIV/OVI	−0.34±0.08
		SiIV	12.43±0.05±0.05			[12.70±0.07±0.03]			SiIV/CIV	−0.77±0.06
		FeIII	12.84±0.14±0.12						FeIII/CIV	−0.36±0.14
		SIII	<13.33						SIII/CIV	< 0.13
Mrk290	−65:60	OVI	14.15±0.03±0.02	−15±6	66±4	14.16±0.06±0.03	−13±6	65±5		
		NV	<13.35			[Emission]			NV/OVI	<−0.80
		FeIII	14.02±0.06±0.03	−16±3	57±7					
		SIII	14.37±0.07±0.16							
Mrk335	−95:60	OVI	14.07±0.02±0.02	−10±3	76±4	14.01±0.06±0.23	−8±2	77±8		
		NV	<13.14			<13.26			NV/OVI	<−0.90
		CIV	14.17±0.03±0.01	−3±2	76±4	14.18±0.07±0.01	−3±4	69±16	CIV/OVI	0.14±0.10
		SiIV	13.61±0.03±0.01	−4±1	68±4	13.56±0.05±0.01	−11±4	75±9	SiIV/CIV	−0.59±0.10
		FeIII	14.27±0.03±0.02	−9±2	73±4				FeIII/CIV	0.09±0.09
		SIII	14.53±0.03±0.26							
	−95:−40	OVI	13.32±0.06±0.12			13.27±0.13±0.42				
		NV	<12.88			<13.03			NV/OVI	<−0.41
		CIV	13.26±0.09±0.02			<13.55			CIV/OVI	−0.03±0.17
		SiIV	12.68±0.10±0.02			<12.88			SiIV/CIV	−0.58±0.13
		FeIII	13.54±0.06±0.11							
		SIII	<13.56						SIII/CIV	< 0.30
	−40:60	OVI	13.98±0.02±0.03	2±3	51±2	13.93±0.05±0.13				
		NV	<13.04			<13.07			NV/OVI	<−0.92
		CIV	14.12±0.03±0.01	6±3	54±3	14.18±0.07±0.01	2±3	57±3	CIV/OVI	0.19±0.09
		SiIV	13.56±0.03±0.01	3±2	51±4	13.47±0.05±0.01	2±4	49±7	SiIV/CIV	−0.63±0.10
		FeIII	14.18±0.02±0.03	1±4	53±5				FeIII/CIV	0.03±0.08
		SIII	14.50±0.03±0.25							
Mrk421	−100:60	OVI	14.33±0.02±0.01	−18±4	94±2	14.36±0.02±0.01	−16±3	91±2		
		NV	<13.11			<13.40			NV/OVI	<−1.24
		FeIII	14.33±0.02±0.01	−41±3	76±5					
		SIII	14.50±0.03±0.04	−35±2	69±4					
Mrk478	−120:65	OVI	14.47±0.05±0.01	−37±4	98±6	[14.25±0.11±0.04]				
		NV	13.55±0.02±0.01	−48±4	93±8	[13.36±0.06±0.03]			NV/OVI	−0.92±0.05
		FeIII	<13.98							
		SIII	<14.44							
	−120:−10	OVI	14.35±0.05±0.02			[14.04±0.13±0.07]				
		NV	13.48±0.02±0.02	−62±3	61±3	[13.35±0.05±0.03]			NV/OVI	−0.87±0.05
		FeIII	13.98±0.10±0.05							
		SIII	14.32±0.13±0.06							
	−10:65	OVI	13.87±0.09±0.06			[13.85±0.15±0.09]				
		NV	<12.76			<12.82			NV/OVI	<−1.11
		FeIII	<13.72							

Table 2—Continued

Object	vel. range	ion	strong line			weak line			ratios	
			$\log N$ [cm^{-2}]	$<v>$ [km s^{-1}]	FWHM [km s^{-1}]	$\log N$ [cm^{-2}]	$<v>$ [km s^{-1}]	FWHM [km s^{-1}]	ions	log ratio
	km s^{-1}]									
(1)	(2)	(3)	(4)	(5)	(6)	(7)	(8)	(9)	(10)	(11)
		SIII	<14.18							
Mrk501	−55:25	OVI	14.23±0.05±0.03	−16±5	44±3	14.22±0.07±0.05	−25±8	46±6		
		NV	<13.29			<13.56			NV/OVI	<−0.93
		FeIII	13.94±0.09±0.04	−11±3	37±4					
		SIII	14.42±0.08±0.04	−19±5	39±5					
Mrk509	−90:115	OVI	14.67±0.02±0.01	21±2	102±2	14.72±0.02±0.02	15±7	115±8		
		NV	13.81±0.04±0.01	32±6	101±10	13.76±0.07±0.01	26±7	95±12	NV/OVI	−0.91±0.09
		CIV	14.51±0.03±0.01			14.37±0.04±0.01	38±5	73±10	CIV/OVI	−0.26±0.06
		SiIV	13.89±0.02±0.01	33±1	82±4	13.89±0.02±0.01	36±2	86±6	SiIV/CIV	−0.55±0.06
		FeIII	14.51±0.02±0.01							
		SIII	14.99±0.02±0.25							
	−90:−30	OVI	13.81±0.03±0.05			[H$_2$]				
		NV	<12.89			<13.17			NV/OVI	<−0.92
		CIV	13.14±0.09±0.03			<13.37			CIV/OVI	−0.67±0.09
		SiIV	<12.45			<12.70			SiIV/CIV	<−0.69
		FeIII	[Unid. Contam.]							
		SIII	<13.53						SIII/CIV	< 0.39
	−30:45	OVI	14.43±0.02±0.02			14.43±0.02±0.03				
		NV	13.51±0.04±0.02			13.54±0.07±0.01			NV/OVI	−0.90±0.09
		CIV	14.30±0.04±0.01	12±4	42±4	14.16±0.05±0.01	16±5	35±10	CIV/OVI	−0.20±0.07
		SiIV	13.68±0.03±0.01	14±4	39±5	13.66±0.03±0.01	16±4	39±8	SiIV/CIV	−0.56±0.07
		FeIII	14.29±0.02±0.02	13±4	37±3				FeIII/CIV	0.06±0.06
		SIII	14.71±0.02±0.07							
	45:115	OVI	14.16±0.02±0.03			14.19±0.02±0.04				
		NV	13.46±0.04±0.02			13.29±0.11±0.02			NV/OVI	−0.80±0.12
		CIV	14.06±0.03±0.01	76±6	39±4	14.01±0.05±0.01	70±6	34±8	CIV/OVI	−0.14±0.07
		SiIV	13.46±0.03±0.01	72±6	38±4	13.49±0.04±0.01	74±7	36±6	SiIV/CIV	−0.57±0.08
		FeIII	13.87±0.04±0.06							
		SIII	14.67±0.02±0.30							
Mrk771	−40:70	OVI	[Lyβ]			14.25±0.17±0.03	12±6	62±9		
		NV	13.40±0.04±0.02	15±0	65±3	13.63±0.05±0.02			NV/OVI	−0.73±0.18
		FeIII	<14.29							
		SIII	<14.78							
Mrk817	−70:60	OVI	14.36±0.02±0.02			14.38±0.02±0.02				
		NV	[Lyα]			<13.16			NV/OVI	<−1.21
		FeIII	14.02±0.02±0.03	−15±4	66±6					
		SIII	14.31±0.02±0.05	−19±3	54±6					
Mrk876	−80:80	OVI	14.42±0.02±0.01			[Lyβ]				
		NV	13.45±0.09±0.01			<13.80			NV/OVI	−0.97±0.09
		CIV	14.21±0.02±0.01			14.14±0.04±0.01			CIV/OVI	−0.24±0.04
		SiIV	13.65±0.02±0.01			13.60±0.02±0.01			SiIV/CIV	−0.56±0.05
		FeIII	14.24±0.03±0.02	−13±4	68±7				FeIII/CIV	0.06±0.05

Table 2—Continued

Object	vel. range	ion	strong line			weak line			ratios	
			$\log N$ [cm^{-2}]	$<v>$ [km s^{-1}]	FWHM [km s^{-1}]	$\log N$ [cm^{-2}]	$<v>$ [km s^{-1}]	FWHM [km s^{-1}]	ions	log ratio
(1)	km s^{-1}] (2)	(3)	(4)	(5)	(6)	(7)	(8)	(9)	(10)	(11)
		SIII	[14.51±0.03±0.31]							
	−80:−30	OVI	13.86±0.02±0.05			[Lyβ]				
		NV	<12.96			[Lyα]			NV/OVI	<−0.90
		CIV	13.76±0.03±0.02			13.69±0.07±0.02			CIV/OVI	−0.14±0.08
		SiIV	13.17±0.02±0.02			13.12±0.03±0.02			SiIV/CIV	−0.58±0.09
		FeIII	13.72±0.04±0.08						FeIII/CIV	0.00±0.09
		SIII	[14.08±0.04±0.15]							
	−30:80	OVI	14.29±0.02±0.02			[Lyβ]				
		NV	13.34±0.09±0.01			[Unid. Contam.]			NV/OVI	−0.95±0.09
		CIV	14.03±0.02±0.01			13.95±0.05±0.01			CIV/OVI	−0.30±0.05
		SiIV	13.49±0.02±0.01			13.43±0.03±0.01			SiIV/CIV	−0.53±0.06
		FeIII	14.09±0.03±0.03						FeIII/CIV	0.10±0.06
		SIII	[14.32±0.03±0.36]							
Mrk1095	−50:45	OVI	13.83±0.07±0.04	1±2	43±5	[H$_2$]				
		NV	13.12±0.13±0.04	4±6	55±7	[Lyα]			NV/OVI	−0.71±0.15
		FeIII	14.22±0.06±0.03	6±3	43±5					
		SIII	14.81±0.05±0.04							
Mrk1383	−105:60	OVI	14.58±0.02±0.01	−20±2	75±3	14.63±0.02±0.01	−23±2	78±3		
		NV	13.84±0.04±0.01	−23±4	85±5	[Lyα]			NV/OVI	−0.77±0.05
		CIV	14.40±0.04±0.01	−28±1	74±3	14.45±0.06±0.01	−29±2	76±4	CIV/OVI	−0.18±0.08
		SiIV	13.81±0.04±0.01	−25±1	59±5	13.76±0.03±0.01	−24±2	62±7	SiIV/CIV	−0.64±0.09
		FeIII	14.34±0.02±0.02	−19±2	62±5				FeIII/CIV	−0.09±0.07
		SIII	14.58±0.03±0.03	−21±2	48±17				SIII/CIV	0.15±0.08
	−105:−50	OVI	13.90±0.03±0.05			14.00±0.04±0.06				
		NV	<13.20			<13.40				
		CIV	13.75±0.05±0.03			13.84±0.08±0.03				
		SiIV	12.92±0.06±0.04			12.88±0.10±0.04				
		FeIII	<13.39							
		SIII	<13.62							
	−50:10	OVI	14.38±0.02±0.02			14.41±0.02±0.03				
		NV	13.63±0.04±0.01	−22±5	39±1	13.73±0.07±0.02			NV/OVI	−0.71±0.09
		CIV	14.24±0.05±0.01	−27±4	34±3	14.29±0.07±0.01	−28±3	31±4	CIV/OVI	−0.12±0.09
		SiIV	13.73±0.05±0.01	−25±2	30±3	13.66±0.03±0.01	−25±3	32±3	SiIV/CIV	−0.57±0.11
		FeIII	14.23±0.02±0.03	−21±3	28±2				FeIII/CIV	−0.04±0.09
		SIII	14.55±0.02±0.03	−20±3	29±2				SIII/CIV	0.28±0.09
	10:60	OVI	13.88±0.03±0.05			13.93±0.04±0.07				
		NV	<13.08			[Lyα]			NV/OVI	<−0.82
		CIV	13.49±0.05±0.01	30±6	27±5	13.44±0.13±0.02	41±8	20±11	CIV/OVI	−0.44±0.15
		SiIV	12.69±0.08±0.02	34±8	25±8	12.76±0.15±0.03	34±9	27±5	SiIV/CIV	−0.74±0.22
		FeIII	13.50±0.05±0.11							
		SIII	<13.57						SIII/CIV	< 0.11
Mrk1502	−50:40	OVI	14.10±0.10±0.03			[H$_2$]				

Table 2—Continued

Object	vel. range	ion	strong line			weak line			ratios	
	$\mathrm{km\,s^{-1}}$]		$\log N$ $[\mathrm{cm^{-2}}]$	$<v>$ $[\mathrm{km\,s^{-1}}]$	FWHM $[\mathrm{km\,s^{-1}}]$	$\log N$ $[\mathrm{cm^{-2}}]$	$<v>$ $[\mathrm{km\,s^{-1}}]$	FWHM $[\mathrm{km\,s^{-1}}]$	ions	log ratio
(1)	(2)	(3)	(4)	(5)	(6)	(7)	(8)	(9)	(10)	(11)
		NV	<13.36			<13.54			NV/OVI	<−0.74
		FeIII	14.27±0.10±0.03	−7±3	43±4					
		SIII	[H$_2$]							
Mrk1513	−90:80	OVI	14.44±0.03±0.01	0±2	79±3	14.51±0.03±0.02	−5±8	92±11		
		NV	13.30±0.04±0.02	4±6	88±10	[Lyα]			NV/OVI	−1.17±0.06
		FeIII	14.26±0.04±0.02	0±3	75±7					
		SIII	14.63±0.05±0.25							
NGC985	−55:90	OVI	14.25±0.04±0.02	12±4	74±6	14.39±0.05±0.02	20±4	82±4		
		NV	13.41±0.03±0.01	23±3	81±5	13.41±0.06±0.03			NV/OVI	−0.91±0.09
		FeIII	14.18±0.06±0.03	−5±4	64±10					
		SIII	14.60±0.06±0.16							
NGC1705	−90:80	OVI	14.23±0.04±0.02			[CII*]				
		NV	13.52±0.06±0.01			[NV−NGC1705]				
		CIV	14.33±0.03±0.01	−8±1	71±4	[CIV−NGC1705]				
		SiIV	13.66±0.02±0.01	−14±1	64±5	13.62±0.03±0.01	−10±1	60±6		
		FeIII	14.21±0.02±0.02	−15±2	66±6					
		SIII	[Stellar]							
	−90:10	OVI	14.00±0.04±0.03			[CII*]				
		NV	13.28±0.07±0.01			[NV−NGC1705]				
		CIV	14.22±0.04±0.01	−22±4	44±8	[CIV−NGC1705]				
		SiIV	13.58±0.02±0.01	−24±3	44±6	13.51±0.03±0.01	−22±4	37±9	SiIV/CIV	−0.68±0.06
		FeIII	14.12±0.02±0.03						FeIII/CIV	−0.10±0.04
		SIII	[Stellar]							
	10:80	OVI	13.87±0.04±0.04			[CII*]				
		NV	13.17±0.07±0.02			[NV−NGC1705]				
		CIV	13.70±0.04±0.02			[CIV−NGC1705]				
		SiIV	12.96±0.04±0.02			12.97±0.07±0.02	28±6	23±7	SiIV/CIV	−0.74±0.09
		FeIII	13.52±0.06±0.11						FeIII/CIV	−0.18±0.07
		SIII	[13.97±0.05±0.09]							
NGC3516	−90:65	OVI	[OVI−NGC3516]			[OVI−NGC3516]				
		NV	<13.59			<14.12				
		CIV	13.80±0.03±0.01	−36±3	67±6	13.91±0.04±0.01	−38±4	67±6		
		SiIV	13.23±0.10±0.01	−41±7	50±15	<13.42			SiIV/CIV	−0.63±0.11
		FeIII	14.25±0.09±0.03	−41±4	55±17				FeIII/CIV	0.39±0.10
		SIII	[H$_2$]							
	−90:0	OVI	14.25±0.06±0.04			[OVI−NGC3516]				
		NV	<13.45			<13.96			NV/OVI	<−0.80
		CIV	13.76±0.03±0.01	−42±3	47±2	13.87±0.04±0.02	−44±5	53±2	CIV/OVI	−0.44±0.08
		SiIV	13.29±0.08±0.02	−42±5	44±12	13.33±0.11±0.01	−43±4	39±10	SiIV/CIV	−0.50±0.15
		FeIII	14.31±0.07±0.02						FeIII/CIV	0.50±0.09
		SIII	[H$_2$]							
	0:65	OVI	[OVI−NGC3516]			[OVI−NGC3516]				

Table 2—Continued

Object	vel. range	ion	strong line			weak line			ratios	
			$\log N$ [cm^{-2}]	$<v>$ [km s^{-1}]	FWHM [km s^{-1}]	$\log N$ [cm^{-2}]	$<v>$ [km s^{-1}]	FWHM [km s^{-1}]	ions	log ratio
(1)	km s^{-1}] (2)	(3)	(4)	(5)	(6)	(7)	(8)	(9)	(10)	(11)
		NV	<13.38			<13.86				
		CIV	<12.74			<13.06				
		SiIV	<12.83			<13.15				
		FeIII	<13.73							
		SIII	[H$_2$]							
NGC3783	−75:100	OVI	[14.57±0.02±0.03]			[H$_2$]				
		NV	13.55±0.02±0.01			13.48±0.04±0.01				
		CIV	14.33±0.02±0.01			14.30±0.02±0.01				
		SiIV	13.78±0.02±0.01			13.77±0.02±0.01			SiIV/CIV	−0.53±0.04
		FeIII	[FeII]							
		SIII	[H$_2$]							
	−75:−20	OVI	[13.78±0.02±0.04]			[H$_2$]				
		NV	<12.74			<12.70				
		CIV	13.47±0.02±0.02			13.40±0.02±0.02				
		SiIV	12.99±0.02±0.02	−40±6	29±7	12.89±0.03±0.02	−38±7	28±8	SiIV/CIV	−0.50±0.05
		FeIII	[FeII]							
		SIII	[H$_2$]							
	−20:100	OVI	[14.50±0.02±0.04]			[H$_2$]				
		NV	13.48±0.02±0.01			13.48±0.04±0.01				
		CIV	14.27±0.02±0.01	26±3	59±3	14.24±0.02±0.01	24±3	55±3		
		SiIV	13.71±0.02±0.01	26±3	54±4	13.71±0.02±0.01	26±3	53±3	SiIV/CIV	−0.55±0.04
		FeIII	[FeII]							
		SIII	[H$_2$]							
NGC4151	−100:60	OVI	[14.21±0.02±0.02]			[14.13±0.05±0.04]				
		NV	13.22±0.11±0.01	−29±7	64±17	[Complex continuum]				
		CIV	14.05±0.02±0.01	−29±2	72±4	[Complex continuum]				
		SiIV	13.54±0.02±0.01	−26±0	56±6	13.53±0.03±0.01	−25±2	59±6	SiIV/CIV	−0.51±0.04
		FeIII	14.25±0.02±0.02	−18±2	59±6				FeIII/CIV	0.20±0.03
		SIII	14.49±0.02±0.28	−21±4	56±7				SIII/CIV	0.44±0.03
	−100:−60	OVI	<12.74			<13.07				
		NV	<12.68			[Complex continuum]				
		CIV	13.26±0.03±0.03			[Complex continuum]				
		SiIV	12.40±0.07±0.07			<12.38				
		FeIII	<12.90							
		SIII	13.43±0.08±0.33							
	−60:25	OVI	[14.05±0.02±0.03]			[13.92±0.05±0.07]				
		NV	13.19±0.08±0.01	−24±4	45±4	[Complex continuum]				
		CIV	13.97±0.02±0.01	−22±4	51±3	[Complex continuum]				
		SiIV	13.51±0.02±0.01	−24±4	49±2	13.51±0.02±0.01	−26±4	49±2	SiIV/CIV	−0.46±0.04
		FeIII	14.21±0.02±0.02	−18±2	41±2				FeIII/CIV	0.24±0.03
		SIII	14.49±0.02±0.10							
	25:60	OVI	[13.77±0.02±0.06]			[13.73±0.04±0.10]				

Table 2—Continued

Object	vel. range	ion	strong line			weak line			ratios	
	km s^{-1}]		log N [cm^{-2}]	$<v>$ [km s^{-1}]	FWHM [km s^{-1}]	log N [cm^{-2}]	$<v>$ [km s^{-1}]	FWHM [km s^{-1}]	ions	log ratio
(1)	(2)	(3)	(4)	(5)	(6)	(7)	(8)	(9)	(10)	(11)
		NV	<12.70			[Complex continuum]				
		CIV	<12.56			[Complex continuum]				
		SiIV	<12.12			<12.40				
		FeIII	<12.90							
		SIII	<13.05							
NGC5548	−110:30	OVI	14.48±0.05±0.01	−31±4	78±2	14.31±0.09±0.03				
		NV	13.63±0.03±0.01	−38±3	68±5	13.68±0.06±0.01	−51±4	67±9	NV/OVI	−0.74±0.12
		CIV	14.46±0.01±0.01	−44±1	64±3	14.43±0.02±0.01	−47±1	63±3	CIV/OVI	0.06±0.11
		SiIV	13.81±0.02±0.01	−45±1	64±3	13.84±0.02±0.01	−43±1	62±4	SiIV/CIV	−0.63±0.05
		FeIII	14.33±0.08±0.02	−28±2	52±8				FeIII/CIV	−0.12±0.09
		SIII	14.54±0.12±0.03							
	−110:−50	OVI	13.97±0.08±0.06			<13.95				
		NV	13.21±0.04±0.04			13.40±0.07±0.04			NV/OVI	−0.67±0.11
		CIV	14.12±0.04±0.03	−69±5	28±7	14.14±0.03±0.02	−69±5	28±7	CIV/OVI	0.16±0.09
		SiIV	13.49±0.03±0.03	−68±5	30±9	13.48±0.03±0.04	−68±6	30±10	SiIV/CIV	−0.65±0.06
		FeIII	<13.81						FeIII/CIV	<−0.32
		SIII	<14.28						SIII/CIV	< 0.15
	−50:30	OVI	14.33±0.05±0.03			14.15±0.10±0.06				
		NV	13.43±0.03±0.03			13.39±0.08±0.04			NV/OVI	−0.83±0.14
		CIV	14.21±0.03±0.02	−25±6	43±3	14.14±0.03±0.02	−25±6	39±5	CIV/OVI	−0.06±0.12
		SiIV	13.54±0.03±0.03	−24±6	43±3	13.61±0.03±0.03	−25±6	41±4	SiIV/CIV	−0.61±0.06
		FeIII	14.25±0.08±0.04						FeIII/CIV	0.07±0.09
		SIII	14.35±0.13±0.06							
NGC7469	−75:65	OVI	[14.01±0.04±0.04]			[H$_2$]				
		NV	<12.69			<13.24				
		CIV	14.07±0.02±0.01	1±2	79±2	14.08±0.03±0.01	−3±3	84±2		
		SiIV	13.56±0.02±0.01	−4±1	68±3	13.51±0.04±0.01	−3±3	71±5	SiIV/CIV	−0.53±0.06
		FeIII	14.24±0.04±0.02						FeIII/CIV	0.17±0.06
		SIII	[H$_2$]							
	−75:−10	OVI	[13.78±0.05±0.06]			[H$_2$]				
		NV	12.48±0.15±0.04			<13.04				
		CIV	13.66±0.03±0.01			13.70±0.05±0.02				
		SiIV	13.24±0.03±0.01			13.18±0.05±0.01	−31±5	28±7	SiIV/CIV	−0.47±0.08
		FeIII	14.03±0.04±0.05						FeIII/CIV	0.35±0.07
		SIII	[H$_2$]							
	−10:65	OVI	[13.67±0.07±0.08]			[H$_2$]				
		NV	<12.61			<13.08				
		CIV	13.86±0.02±0.01			13.86±0.04±0.01				
		SiIV	13.29±0.03±0.01			13.25±0.05±0.01			SiIV/CIV	−0.59±0.07
		FeIII	13.88±0.06±0.06						FeIII/CIV	0.02±0.07
		SIII	[H$_2$]							
PG0804+761	−90:60	OVI	14.49±0.02±0.01			[H$_2$]				

Table 2—Continued

Object	vel. range	ion	strong line			weak line			ratios	
			log N [cm^{-2}]	$<v>$ [km s^{-1}]	FWHM [km s^{-1}]	log N [cm^{-2}]	$<v>$ [km s^{-1}]	FWHM [km s^{-1}]	ions	log ratio
(1)	km s^{-1}] (2)	(3)	(4)	(5)	(6)	(7)	(8)	(9)	(10)	(11)
		NV	[Lyα]			<13.39			NV/OVI	<−1.10
		FeIII	14.28±0.02±0.01	−33±1	51±5					
		SIII	14.78±0.02±0.21							
PG0953+414	−125:70	OVI	14.36±0.02±0.01	−14±5	106±4	14.31±0.04±0.05	−20±7	113±12		
		NV	<13.22			<13.55			NV/OVI	<−1.12
		CIV	13.97±0.03±0.01	−22±3	114±3	13.84±0.08±0.01	−21±6	116±5	CIV/OVI	−0.44±0.10
		SiIV	13.34±0.05±0.01			13.32±0.07±0.01	−20±3	104±5		
		FeIII	14.14±0.04±0.03							
		SIII	14.27±0.07±0.12							
	−125:−35	OVI	13.88±0.03±0.04			13.86±0.07±0.13				
		NV	<13.03			<13.36			NV/OVI	<−0.84
		CIV	13.56±0.04±0.01			13.42±0.12±0.01			CIV/OVI	−0.38±0.15
		SiIV	[13.09±0.05±0.01]			12.88±0.10±0.01			SiIV/CIV	−0.61±0.16
		FeIII	13.90±0.04±0.05							
		SIII	14.06±0.08±0.08							
	−35:70	OVI	14.19±0.02±0.02			14.13±0.05±0.04				
		NV	<13.09			<13.40			NV/OVI	<−1.07
		CIV	13.76±0.03±0.01			13.63±0.08±0.01			CIV/OVI	−0.46±0.10
		SiIV	13.00±0.07±0.01			13.14±0.07±0.01			SiIV/CIV	−0.63±0.13
		FeIII	13.79±0.06±0.06							
		SIII	13.89±0.11±0.22							
PG1049−005	−60:40	NV	13.67±0.06±0.02	−4±4	46±7	<13.63				
PG1116+215	−85:85	OVI	14.21±0.02±0.01	13±2	80±4	14.26±0.03±0.02	12±4	82±6		
		NV	<13.33			<13.45				
		CIV	14.20±0.02±0.01			14.15±0.03±0.01				
		SiIV	13.67±0.02±0.01	−18±2	78±3	13.70±0.02±0.01	−10±2	82±4		
		FeIII	14.37±0.02±0.01	−21±2	72±5					
		SIII	14.60±0.03±0.07	−14±2	71±5					
	−85:−20	OVI	13.51±0.05±0.04			13.50±0.10±0.06				
		NV	<12.94			<13.27			NV/OVI	<−0.57
		CIV	13.86±0.02±0.01			13.84±0.04±0.01			CIV/OVI	0.34±0.12
		SiIV	13.38±0.02±0.01			13.32±0.02±0.01			SiIV/CIV	−0.50±0.05
		FeIII	14.12±0.03±0.02						FeIII/CIV	0.27±0.05
		SIII	14.25±0.04±0.03						SIII/CIV	0.40±0.06
	−20:30	OVI	13.90±0.03±0.03			13.97±0.04±0.03				
		NV	<12.91			<13.17			NV/OVI	<−1.03
		CIV	13.78±0.03±0.02			13.73±0.05±0.01	4±5	27±2	CIV/OVI	−0.18±0.08
		SiIV	13.30±0.02±0.02	0±6	29±2	13.38±0.02±0.02	3±6	31±2	SiIV/CIV	−0.42±0.07
		FeIII	13.96±0.03±0.03						FeIII/CIV	0.20±0.07
		SIII	14.29±0.03±0.06						SIII/CIV	0.53±0.07
	30:85	OVI	13.76±0.03±0.03			13.81±0.05±0.05				
		NV	<12.96			<13.22			NV/OVI	<−0.83

Table 2—Continued

Object (1)	vel. range [km s^{-1}] (2)	ion (3)	strong line			weak line			ratios	
			$\log N$ [cm^{-2}] (4)	$<v>$ [km s^{-1}] (5)	FWHM [km s^{-1}] (6)	$\log N$ [cm^{-2}] (7)	$<v>$ [km s^{-1}] (8)	FWHM [km s^{-1}] (9)	ions (10)	log ratio (11)
		CIV	13.47±0.04±0.02			13.30±0.10±0.03			CIV/OVI	−0.41±0.13
		SiIV	12.59±0.06±0.03			12.79±0.08±0.03			SiIV/CIV	−0.69±0.15
		FeIII	13.26±0.12±0.06						FeIII/CIV	−0.12±0.16
		SIII	<13.54						SIII/CIV	< 0.16
PG1211+143	−80:60	OVI	14.16±0.03±0.02	6±3	66±4	14.20±0.05±0.06	3±4	74±5		
	−60:60	NV	13.34±0.05±0.01	−7±5	66±5	[Lyα]			NV/OVI	−0.84±0.08
	−80:60	CIV	14.09±0.02±0.01	−9±1	53±5	14.09±0.02±0.01	−4±2	62±4	CIV/OVI	−0.09±0.07
		SiIV	13.61±0.02±0.01	−6±1	51±5	[13.72±0.02±0.01]			SiIV/CIV	−0.48±0.04
		FeIII	14.18±0.03±0.02	−6±2	56±4				FeIII/CIV	0.09±0.04
		SIII	14.51±0.04±0.18						SIII/CIV	0.42±0.05
PG1216+069	−60:60	OVI	[Lyβ]			[Unid. Contam.]				
		NV	[CIII]			[Lyβ]				
		CIV	[Unid. Contam.]			[Unid. Contam.]				
		SiIV	13.57±0.03±0.01	−1±2	49±4	13.46±0.05±0.01	0±3	31±9		
		FeIII	<14.26							
		SIII	<14.74							
PG1259+593	−80:50	OVI	14.11±0.02±0.01	−6±5	79±2	14.15±0.04±0.02	−12±6	81±4		
		NV	13.14±0.12±0.01			[Lyα]			NV/OVI	−0.99±0.13
		CIV	13.75±0.04±0.01	−5±3	65±4	13.76±0.08±0.01	−15±7	84±7	CIV/OVI	−0.37±0.10
		SiIV	13.33±0.02±0.01	−14±3	67±6	13.39±0.06±0.01	−12±3	77±4	SiIV/CIV	−0.40±0.11
		FeIII	14.11±0.02±0.01	−18±3	71±3				FeIII/CIV	0.35±0.09
		SIII	14.32±0.04±0.04							
	−80:−27	OVI	13.59±0.04±0.04			13.71±0.06±0.04				
		NV	12.98±0.11±0.02			[Lyα]				
		CIV	13.16±0.07±0.03			13.36±0.11±0.03			CIV/OVI	−0.39±0.15
		SiIV	12.88±0.04±0.02			12.99±0.07±0.01			SiIV/CIV	−0.32±0.15
		FeIII	13.74±0.03±0.03						FeIII/CIV	0.48±0.13
		SIII	14.02±0.05±0.03						SIII/CIV	0.76±0.14
	−27:50	OVI	13.97±0.02±0.01			13.97±0.05±0.02				
		NV	<13.00			[Lyα]			NV/OVI	<−0.97
		CIV	13.64±0.04±0.01			13.55±0.09±0.01			CIV/OVI	−0.37±0.11
		SiIV	13.15±0.03±0.01			13.18±0.07±0.01			SiIV/CIV	−0.44±0.13
		FeIII	13.88±0.03±0.02						FeIII/CIV	0.28±0.10
		SIII	14.04±0.05±0.08							
PG1302−102	−50:60	OVI	14.22±0.03±0.02	1±2	52±3	14.33±0.04±0.02	−1±3	60±3		
		NV	[Lyα]			<13.87				
		CIV	14.17±0.05±0.01	7±1	50±5	14.20±0.04±0.01	8±2	48±5		
		SiIV	13.73±0.04±0.01	6±2	56±3	13.62±0.07±0.01	7±2	45±7		
		FeIII	14.12±0.04±0.23	10±28	39±16					
		SIII	14.53±0.05±0.09							
	−50:0	OVI	13.92±0.04±0.04			14.09±0.05±0.05				
		NV	[Lyα]			<13.68			NV/OVI	<−0.33

Table 2—Continued

Object	vel. range	ion	strong line			weak line			ratios	
			log N [cm^{-2}]	$<v>$ [km s^{-1}]	FWHM [km s^{-1}]	log N [cm^{-2}]	$<v>$ [km s^{-1}]	FWHM [km s^{-1}]	ions	log ratio
	km s^{-1}]									
(1)	(2)	(3)	(4)	(5)	(6)	(7)	(8)	(9)	(10)	(11)
		CIV	13.64±0.05±0.03			13.68±0.07±0.04			CIV/OVI	−0.35±0.11
		SiIV	13.30±0.05±0.03			13.13±0.11±0.03			SiIV/CIV	−0.45±0.15
		FeIII	13.61±0.08±0.23						FeIII/CIV	−0.05±0.12
		SIII	14.13±0.07±0.08						SIII/CIV	0.47±0.11
	0:60	OVI	13.94±0.04±0.04			13.99±0.06±0.06				
		NV	<13.44			<13.67			NV/OVI	<−0.52
		CIV	14.03±0.06±0.01	19±4	29±5	14.06±0.04±0.01	18±5	33±3	CIV/OVI	0.08±0.10
		SiIV	13.55±0.05±0.02	20±6	37±2	13.48±0.09±0.01	17±5	26±6	SiIV/CIV	−0.52±0.12
		FeIII	13.98±0.05±0.24						FeIII/CIV	−0.06±0.09
		SIII	14.34±0.05±0.14						SIII/CIV	0.30±0.09
PG1351+640	−60:70	OVI	14.24±0.03±0.02	−1±6	74±4	14.37±0.06±0.03				
		NV	13.24±0.08±0.02			<13.30			NV/OVI	−1.06±0.11
		FeIII	[Unid. Contam.]							
		SIII	[H$_2$]							
PG1444+407	−115:20	OVI	14.35±0.11±0.02			14.51±0.13±0.05				
		NV	[Lyα]			13.65±0.10±0.01			NV/OVI	−0.78±0.20
		CIV	14.09±0.02±0.01	−49±1	50±5	14.22±0.04±0.01	−47±2	58±4	CIV/OVI	−0.28±0.17
		SiIV	13.49±0.03±0.01	−43±1	59±4	[Lyα]			SiIV/CIV	−0.66±0.05
	−115:80	FeIII	14.42±0.12±0.02							
		SIII	<14.90						SIII/CIV	< 0.75
	−115:20	OVI	14.35±0.11±0.02			14.51±0.13±0.05				
		NV	[Lyα]			13.65±0.10±0.01			NV/OVI	−0.78±0.20
		CIV	14.09±0.02±0.01	−49±1	50±5	14.22±0.04±0.01	−47±2	58±4	CIV/OVI	−0.28±0.17
		SiIV	13.49±0.03±0.01	−43±1	59±4	[Lyα]			SiIV/CIV	−0.66±0.05
		FeIII	<14.27						FeIII/CIV	< 0.12
		SIII	<14.81						SIII/CIV	< 0.66
PG1718+481	−65:50	CIV	14.09±0.02±0.01	−16±3	57±4	14.12±0.03±0.01	−14±4	61±3		
	−65:−15	CIV	13.82±0.03±0.04	−36±6	27±3	13.83±0.04±0.04	−37±6	26±2		
	−15:50	CIV	13.79±0.03±0.03	6±6	31±4	13.82±0.04±0.03	9±6	31±4		
PHL1811	−65:80	OVI	14.35±0.02±0.01	11±4	75±3	14.27±0.04±0.16	16±5	72±16		
		NV	13.36±0.08±0.01			<13.35				
		CIV	14.29±0.02±0.01	8±1	74±2	14.32±0.03±0.01	7±2	78±2		
		SiIV	13.61±0.02±0.01	9±1	69±3	13.55±0.03±0.01	7±2	66±4		
		FeIII	14.18±0.04±0.02	6±2	63±6					
		SIII	[H$_2$]							
	−65:30	OVI	14.20±0.03±0.02	−6±5	49±2	14.10±0.05±0.17				
		NV	13.22±0.08±0.01	−13±3	47±7	<13.25			NV/OVI	−0.93±0.10
		CIV	14.16±0.02±0.01	−8±3	45±5	14.18±0.03±0.01	−10±4	49±3	CIV/OVI	0.02±0.07
		SiIV	13.50±0.02±0.01	−5±3	42±5	13.45±0.03±0.01	−4±4	42±9	SiIV/CIV	−0.70±0.06
		FeIII	14.07±0.04±0.03	−5±5	39±8				FeIII/CIV	−0.10±0.06
		SIII	[H$_2$]							
	30:80	OVI	13.84±0.04±0.05	51±6	30±2	13.80±0.07±0.16				

Table 2—Continued

Object	vel. range	ion	strong line			weak line			ratios	
			$\log N$ [cm^{-2}]	$<v>$ [km s^{-1}]	FWHM [km s^{-1}]	$\log N$ [cm^{-2}]	$<v>$ [km s^{-1}]	FWHM [km s^{-1}]	ions	log ratio
(1)	km s^{-1}] (2)	(3)	(4)	(5)	(6)	(7)	(8)	(9)	(10)	(11)
		NV	12.80±0.15±0.02	58±5	28±5	<13.07			NV/OVI	−1.02±0.17
		CIV	13.73±0.03±0.01	52±5	26±4	13.80±0.04±0.01	50±4	27±3	CIV/OVI	−0.05±0.09
		SiIV	12.98±0.03±0.02	53±6	25±5	12.88±0.07±0.02			SiIV/CIV	−0.84±0.09
		FeIII	13.56±0.09±0.10						FeIII/CIV	−0.21±0.10
		SIII	[H$_2$]							
PKS0312−77	−70:40	NV	<13.60			<13.90				
		CIV	14.19±0.07±0.01	−18±2	57±5	14.17±0.11±0.01				
		SiIV	13.49±0.06±0.02	−26±7	57±13	13.53±0.08±0.01	−25±7	57±10	SiIV/CIV	−0.67±0.16
		FeIII	[FeII]							
PKS0405−12	−70:55	OVI	13.97±0.04±0.03	1±4	60±6	14.01±0.06±0.05	4±4	56±6		
		NV	<13.27			<13.58			NV/OVI	<−0.72
		CIV	14.09±0.03±0.01	−16±1	51±6	14.05±0.05±0.01	−6±7	64±6	CIV/OVI	0.08±0.09
		SiIV	13.43±0.03±0.01	−9±1	53±5	13.40±0.06±0.01	0±4	51±7	SiIV/CIV	−0.66±0.09
		FeIII	14.14±0.04±0.03	−2±2	55±5				FeIII/CIV	0.07±0.07
		SIII	14.55±0.04±0.07						SIII/CIV	0.48±0.07
PKS2005−489	−110:110	OVI	14.73±0.02±0.01	26±3	111±3	[CII*−GC]				
		NV	13.97±0.02±0.01	30±4	118±3	13.97±0.02±0.01	33±4	115±4	NV/OVI	−0.76±0.04
		FeIII	[FeII]							
		SIII	14.97±0.03±0.04							
	−110:−50	OVI	13.67±0.05±0.06			[CII*−GC]				
		NV	12.90±0.03±0.05			12.85±0.06±0.08			NV/OVI	−0.79±0.09
		FeIII	13.97±0.05±0.04	−79±6	33±3					
		SIII	<13.80							
	−50:50	OVI	14.48±0.02±0.02			14.51±0.03±0.02				
		NV	13.66±0.02±0.02			13.67±0.02±0.02			NV/OVI	−0.83±0.05
		FeIII	14.26±0.04±0.03							
		SIII	14.67±0.03±0.04							
	50:110	OVI	14.30±0.03±0.03			14.29±0.03±0.04				
		NV	13.61±0.02±0.02			13.62±0.02±0.03			NV/OVI	−0.67±0.05
		FeIII	14.22±0.03±0.03							
		SIII	14.65±0.03±0.07							
PKS2155−304	−55:75	OVI	14.25±0.02±0.02	18±5	80±2	14.22±0.02±0.03	16±6	79±2		
	−55:120	NV	[Lyα]			<13.40				
	−55:75	CIV	14.04±0.02±0.01	14±3	77±3	13.97±0.03±0.01	17±3	73±3		
		SiIV	13.33±0.02±0.01	2±3	76±3	13.30±0.04±0.01	0±3	67±6		
		FeIII	13.96±0.03±0.03	5±2	57±6					
		SIII	14.13±0.04±0.06	−6±2	43±10					
	−55:20	OVI	13.95±0.02±0.04			13.94±0.03±0.06				
		NV	[Lyα]			<13.26			NV/OVI	<−0.69
		CIV	13.77±0.03±0.01	−12±7	46±7	13.66±0.05±0.02	−10±9	47±8	CIV/OVI	−0.24±0.07
		SiIV	13.17±0.02±0.01	−16±5	44±4	13.17±0.04±0.01	−14±4	39±5	SiIV/CIV	−0.54±0.07
		FeIII	13.84±0.03±0.05	−7±4	29±6				FeIII/CIV	0.13±0.07

Table 2—Continued

Object	vel. range	ion	strong line			weak line			ratios	
	$\mathrm{km\,s^{-1}}$]		$\log N$ [cm^{-2}]	$<v>$ [km s^{-1}]	FWHM [km s^{-1}]	$\log N$ [cm^{-2}]	$<v>$ [km s^{-1}]	FWHM [km s^{-1}]	ions	log ratio
(1)	(2)	(3)	(4)	(5)	(6)	(7)	(8)	(9)	(10)	(11)
		SIII	14.12±0.03±0.06	−10±3	33±5				SIII/CIV	0.41±0.07
	20:75	OVI	13.96±0.02±0.04			13.92±0.02±0.06				
		NV	<12.92			<13.19			NV/OVI	<−1.02
		CIV	13.73±0.02±0.02	43±5	35±1	13.71±0.04±0.02	41±5	34±2	CIV/OVI	−0.22±0.05
		SiIV	12.85±0.04±0.02			12.71±0.11±0.03			SiIV/CIV	−0.94±0.13
		FeIII	13.35±0.08±0.14							
		SIII	<13.31						SIII/CIV	<−0.41
RX J0100.4−5113	−50:60	OVI	14.18±0.06±0.03	24±5	42±12	14.33±0.07±0.04				
		NV	<13.13			<13.55			NV/OVI	<−1.13
		FeIII	14.17±0.08±0.03	2±3	58±4					
		SIII	14.38±0.12±0.04	3±5	60±7					
RX J1830.3+7312	−70:30	OVI	14.33±0.09±0.02	−28±5	43±6	[14.38±0.10±0.04]				
		NV	[13.14±0.04±0.04]			[13.39±0.05±0.03]				
		FeIII	14.22±0.07±0.03	−34±5	47±9					
		SIII	[H$_2$]							
Ton S180	−80:75	OVI	14.33±0.03±0.01	−10±3	72±5	14.31±0.06±0.03	−11±4	80±6		
		NV	13.12±0.07±0.02	−15±7	82±15	<13.24			NV/OVI	−1.20±0.10
		FeIII	14.05±0.07±0.03	−9±5	77±9					
		SIII	14.18±0.12±0.06	−14±8	76±16					
Ton S210	−75:85	OVI	14.49±0.02±0.01			14.46±0.03±0.02				
		NV	13.56±0.13±0.01	−3±7	86±16	<13.91			NV/OVI	−0.91±0.14
		CIV	14.38±0.04±0.01	−8±4	90±4	14.31±0.06±0.01	−15±6	86±6	CIV/OVI	−0.12±0.08
		SiIV	13.61±0.04±0.01	−13±2	74±5	[Unid. Contam.]			SiIV/CIV	−0.74±0.08
		FeIII	14.01±0.06±0.03	−6±3	74±10				FeIII/CIV	−0.34±0.09
		SIII	14.36±0.07±0.14							
UGC12163	−90:70	OVI	14.12±0.10±0.03			14.29±0.12±0.04				
		NV	<13.60			<13.64			NV/OVI	<−0.61
		CIV	14.34±0.06±0.01			14.30±0.12±0.01	−10±6	72±13	CIV/OVI	0.11±0.21
		SiIV	13.82±0.06±0.01	−8±1	72±6	[Unid. Contam.]			SiIV/CIV	−0.50±0.14
		FeIII	14.44±0.07±0.02	11±6	89±7				FeIII/CIV	0.12±0.15
		SIII	14.85±0.09±0.13						SIII/CIV	0.53±0.16
VIIZw118	−125:60	OVI	14.29±0.03±0.01	−28±2	95±3	[CII*]				
		NV	13.19±0.07±0.02			<13.35			NV/OVI	−1.10±0.08
		FeIII	14.31±0.02±0.02	−29±8	83±15					
		SIII	[H$_2$]							
	−125:−40	OVI	13.91±0.04±0.04			[CII*]				
		NV	13.11±0.06±0.02	−77±4	46±3	<13.06			NV/OVI	−0.80±0.07
		FeIII	13.91±0.04±0.06							
		SIII	[H$_2$]							
	−40:60	OVI	14.06±0.03±0.03			[H$_2$]				
		NV	<12.78			<13.16			NV/OVI	<−1.28
		FeIII	14.10±0.03±0.03							

4. Results

In this section we analyze several different aspects of the highly ionized gas, including the kinematic properties of the absorption lines (extent, component width, relation to Galactic rotation), the distribution of column densities, the distribution of velocities and column densities across the sky, and the distribution of column density ratios. These analyses show that the gas in which these ions occur participates in differential galactic rotation, but has a large velocity dispersion. There is no evidence for a gradient in the rotation velocity with height above the Galactic plane. The highly-ionized ions are present across the sky, in similar amounts in every direction, but with a patchy distribution. There are some well-delineated regions where the average properties are noticeably different (factor two average enhancement around the Galactic Center and near the Galactic North Pole, O VI showing a factor two deficit at intermediate southern latitude). The column densities and column density ratios in individual parcels of transition temperature gas have a narrow distribution, suggesting a uniformity of its properties.

4.1. Velocity differences between ions

We compared the centroids of the absorption profiles of the different ions (O VI, N V, C IV, Si IV, Fe III) to each other and found that they correlate very well. In particular, for the 9 components where both the O VI and N V absorption lines are well-defined and simple, the centroids have an average offset of 0 ± 8 $\mathrm{km\,s^{-1}}$, i.e. the rms difference is well within the resolution of the *FUSE* O VI spectra, as well as within the alignment errors associated with the wavelength calibration of the *FUSE* data. For the 24 components with good data for both C IV and Si IV the difference in their centroids is 0 ± 3 $\mathrm{km\,s^{-1}}$. The centroids of O VI components are about 4 ± 8 $\mathrm{km\,s^{-1}}$ more negative than those of C IV, Si IV and Fe III, which is not a significant difference. The N V and C IV lines appear to be well-aligned (average difference -2 ± 4 $\mathrm{km\,s^{-1}}$ for 7 components), and all of the cases where both of these lines are seen are derived from STIS-E140M spectra. Thus, the preponderance of the evidence suggests that there are *no* velocity offsets between the centroids of the absorption lines of the different highly-ionized species.

4.2. Velocity extent of the Galactic absorption

In each direction, there is a range of velocities that is compatible with differential galactic rotation. Following Wakker (2004), we estimate this range using a model in which gas rotates

at 220 km s^{-1} around the center of the Milky Way for galactocentric radii 0.5 to 26 kpc in a layer with thickness 3 kpc inside the 8.0 kpc solar radius, increasing to 6 kpc at 26 kpc from the Galactic Center. At radii <0.5 kpc the velocity of rotation is assumed to decrease linearly to 0 km s^{-1} at R=0. Since most of our targets are at high galactic latitude, this usually produces a narrow range from 0 to about plus or minus 10 km s^{-1}, except for directions below $|b|$=30°, where a range of 0 to about plus or minus 40 km s^{-1} is found.

Figure 3 shows the observed extents of the absorption profiles graphically. The vertical lines give the range of velocities over which Galactic absorption is seen, while the short horizontal lines are drawn at the median difference of ±60 km s^{-1} more positive or negative than those the simple model predicts. As this figure shows, the observed range of velocities over which absorption is seen is much larger than that predicted by differential galactic rotation. Absorption typically extends to velocities that are 45 to 100 km s^{-1} more negative than expected, with an extreme of 125 km s^{-1} toward PG 0953+414. At high latitudes (b>45°) the typical profile also extends to velocities that are 30 to 80 km s^{-1} more positive. Looking separately at positive and negative velocities for four sky quadrants (b=−90°:−45°, b=−45°:0°, b=0°:45° and b=45°:90° (10, 10, 9 and 16 sightlines, respectively), the median and the average deviation from the maximum negative or positive velocity predicted by the simple model of rotation is about 60 km s^{-1}, *except* for negative velocities near the north polar cap, where the median and average are 90 km s^{-1}. That is, for sightlines near the north galactic pole there appears to be an excess of absorption at velocities more negative than −60 km s^{-1}.

The velocity range over which the Milky Way transition-temperature gas absorption extends is likely proportional to the outflow velocity of the hot gas. A value of about 60 km s^{-1} is in line with the predictions of Houck & Bregman (1990) for the formation velocities of neutral (i.e. cooled) clouds in a low-temperature (5×10^5 K) Galactic Fountain, with a density of 10^{-3} cm^{-3} and a (two-sided) flow rate of 0.4 M$_\odot$ yr^{-1}. Statistically speaking, however, the absorption profiles have a similar extent at positive and negative velocities, independent of Galactic longitude or latitude. Thus, on average, vertical motions are as large as motions parallel to the plane. This suggests that the material is highly turbulent. The only evidence for a deviation from this pattern is that there appears to be a slight preference for infall in the North Galactic Cap region. This may just be a temporary local occurrence in the solar neighborhood, however.
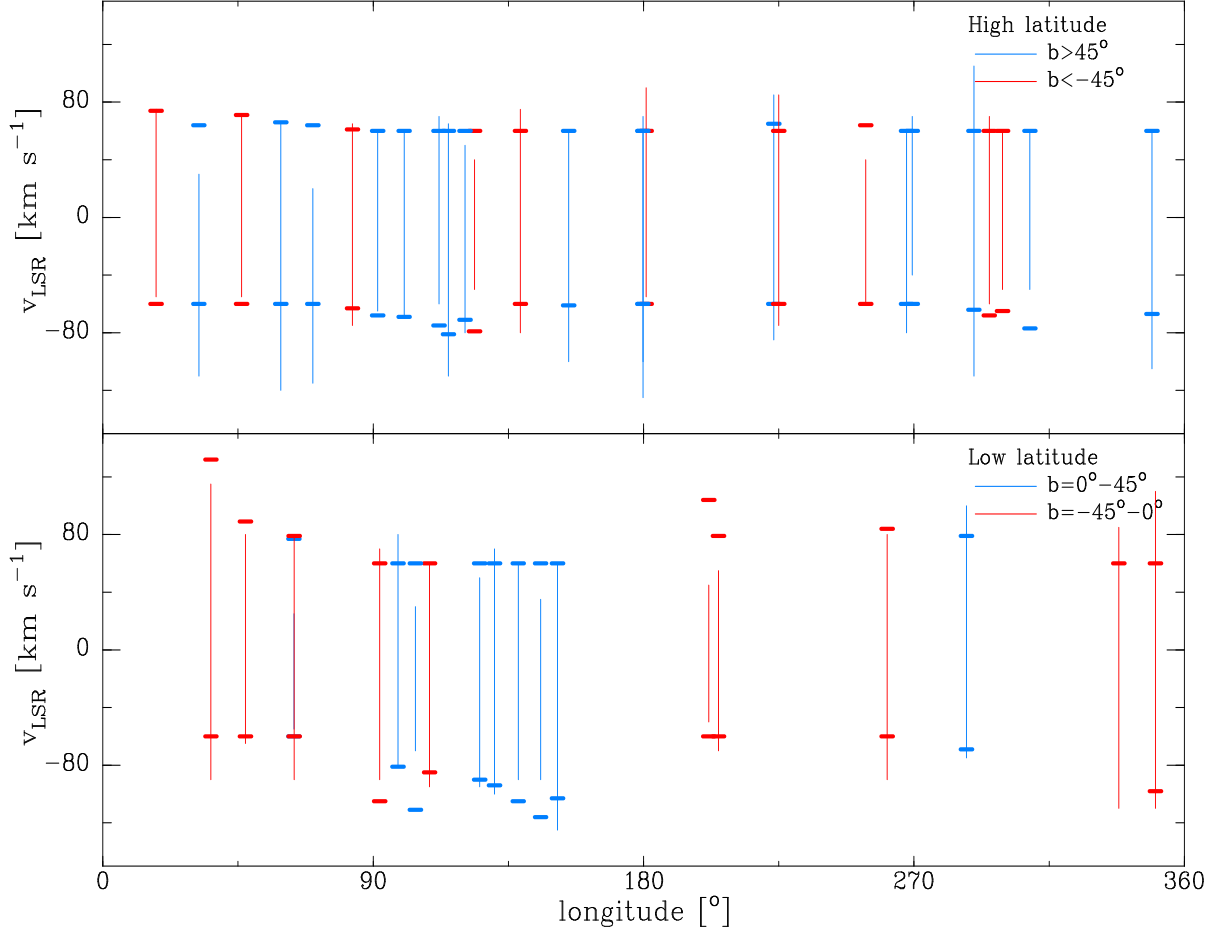
Fig. 3.— Comparison of the extent of the Galactic high-ionization absorption with the range of velocities allowed by differential galactic rotation, as function of galactic longitude. The thick horizontal bars are placed at velocities ± 60 km s^{-1} larger/smaller than the maximum/minimum velocity expected from rotation. The vertical lines indicate the observed range of velocities over which high-ionization absorption is seen. The top panel shows high-latitude sightlines, the bottom panel low-latitude sightlines, with northern sightlines in blue and southern sightlines in red.

4.3. Line width distribution

In Figure 4 we look at the distribution of linewidths, rather than at the total extent of the absorption. These widths are found by calculating the second moment (b) of the $N_a(v)$ distribution, converting it into the full-width-at-half-maximum (FWHM=1.665 b) and correcting for instrumental broadening. The figure has two panels for each ion. In the top panel we use the full absorption profile, while in the bottom panel we use the FWHM for individual components (see Section 3). Note that in about half of the sightlines only a single component can be discerned. Only components where the measured width was deemed reliable are included. This means that in some sightlines the width of the full profile can be measured, but the widths of the two or three components that make up the profile are individually unreliable. Thus, the total number of measurements of the full line width is larger than the number of well-measured components.

For many sightlines it is possible to separately calculate the widths of both members of the O VI, N V, C IV and Si IV doublets. In every case the two widths are identical to within the errors. Therefore, we use only the width of the strong line for the histograms in Figure 4 (except when only the weak line was measurable). Widths are not calculated if the Galactic profile blends with high-velocity absorption and it is not clear where to place the boundary (for Mrk 205, Mrk 279, Mrk 817, Mrk 876, and NGC 3783). All cases where we deemed it possible to estimate a width are listed in Table 2 and used in Figure 4.

We do not explicitly show a figure that directly compares the widths of the ions in individual absorption components, but these correlate very well. That is, if FWHM(O VI) is large, then FWHM(N V) is large. The correlation coefficient between the two widths is 0.97. FWHM(C IV) and FWHM(Si IV) also correlate closely (correlation coefficient 0.94). The correlation between FWHM(O VI) or FWHM(N V) and FWHM(C IV) or FWHM(Si IV) is not quite as good, but still strong ($\sim$0.92). Thus, O VI goes closely together with N V, but somewhat less strongly with C IV and Si IV, even though N V, C IV and Si IV are determined from STIS-E140M spectra (with 6.5 km s^{-1} resolution), while O VI is seen in *FUSE* spectra (20 km s^{-1} resolution). Thus, the differences in linewidths are not likely to be an artifact of the higher resolution of the STIS-E140M spectra.

As Fig. 4 shows, the FWHM of the full Galactic absorption ranges from about 50 km s^{-1} to about 120 km s^{-1}, with an average value in the range 60–80 km s^{-1}, dependent on the ion. The widths of the O VI and N V absorption lines appear similar, while those of C IV, Si IV and Fe III appear to be slightly narrower. We applied a t-test to see whether these differences are statistically significant. This test is most useful when applied to the distributions of the widths of the individual components. Then the difference in the average linewidth of O VI and N V (59$\pm$18 km s^{-1} and 62$\pm$20 km s^{-1}) is not significant (the probability that they do
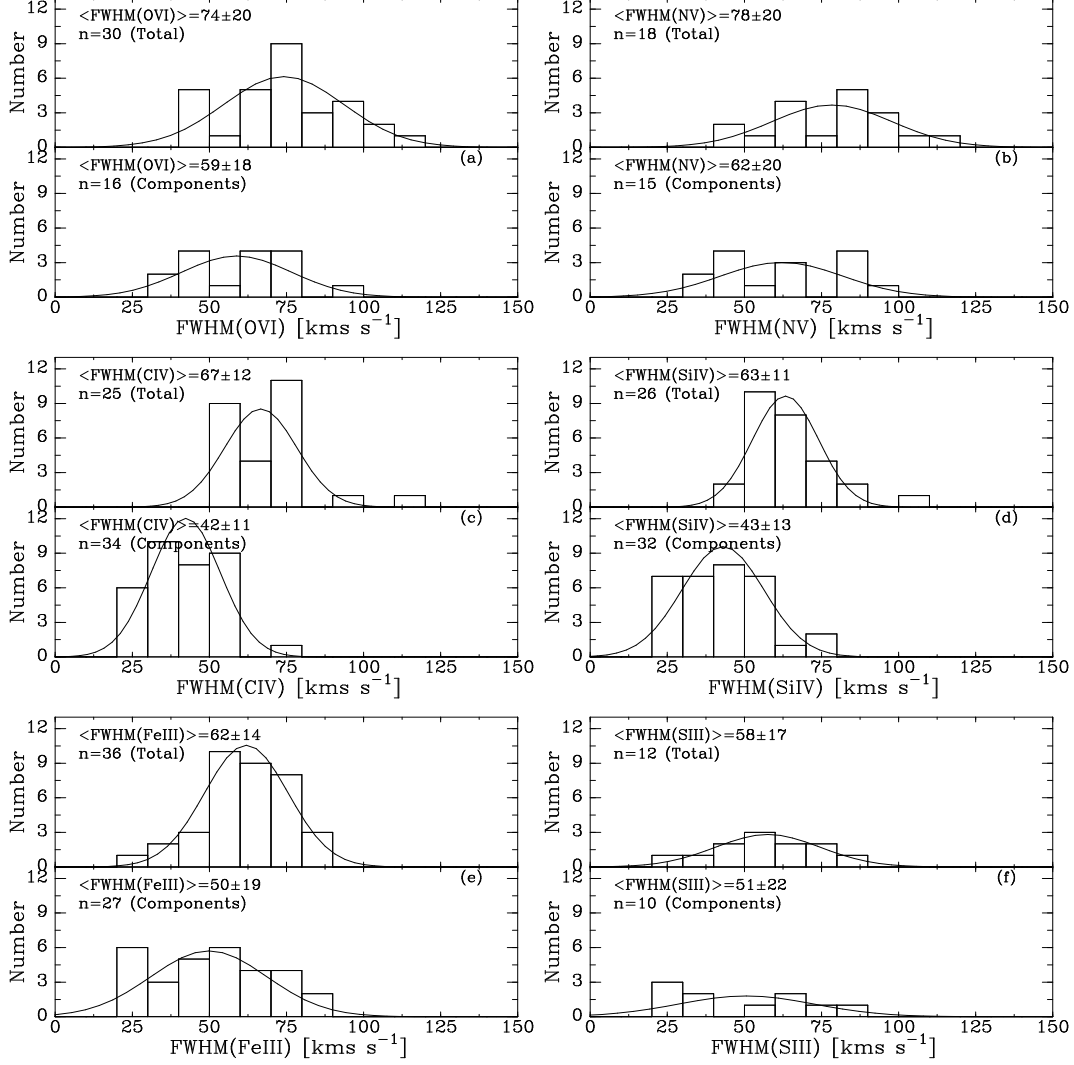
Fig. 4.— Distribution of linewidths for the six ions. There are two panels for each ion, with the top panel in each pair showing the distributions of the FWHM (calculated from the second moment) for the integrated Galactic absorption, and the bottom panel showing the values for individual components. The FWHM of the full Galactic absorption profile is a general indicator for the velocity spread of the high-ionization absorption associated with the Milky Way disk and lower corona. The FWHM of the individual components indicates the velocity spread in single structures. The average and spread of each distribution are given in the label, as are the number of sightlines/components that are used.

not differ is 55%). This is also the case for the difference between the average widths of C IV and Si IV (42 ± 11 km s^{-1} and 43 ± 13 km s^{-1}, probability that they do not differ is 80%). However, the difference between each pair of ions *is* significant, with probabilities that the widths do not differ of <0.5% when comparing O VI or N V to C IV or Si IV. The average width of the Fe III line (50 ± 19 km s^{-1}) is marginally larger than that of C IV (probability it does not differ 5%), and insignificantly smaller than that of O VI (probability it does not differ 2%). Thus, we cannot really tell whether Fe III belongs in the C IV/Si IV group or in the O VI/N V group. Because of its lower ionization potential, the former is more likely, however. For S III the number of points is too small to say anything useful.

Thus, the evidence points to a situation in which the O VI and N V lines have similar widths, as do the C IV, and Si IV lines, with the latter two ions having narrower lines on average. The general correlation of the linewidths and the alignment in velocity between all ions (see Section 4.1) shows that the different ions must originate in the same general structures, but also that they cannot be completely co-spatial. Further, since even at a temperature of 10^5 K the thermal width of the lightest of our elements (carbon) is only 20 km s^{-1}, most of the observed linewidth cannot be due to thermal broadening. This implies that there is either a high level of turbulence or there are strong velocity gradients in the gas.

A difference in line widths between O VI/N V vs C IV/Si IV was previously found by Fox et al. (2003), who analyzed high-resolution (3.5 km s^{-1}) STIS-E140H data of the halo star HD 116852. They saw both a narrow and a broad C IV and Si IV line, but O VI and N V did not show the narrow absorption. They interpreted this as indicating that there are regions in the Thick Disk that are sufficiently warm to contain C IV, but not warm enough to have O VI. In an analysis of 38 high-resolution STIS-E140H spectra of stars, Lehner et al. (2011) find the same effect in several other sightlines, with the average FWHM of the narrow C IV and Si IV components about $\sim$20 km s^{-1}. They further find only broad absorption components for O VI and N V (average FWHM 65 ± 22 and 50 ± 25 km s^{-1}, respectively), The S/N ratio of our data is usually not nearly as high as it is for these stellar spectra, making it more difficult to separate narrow and broad C IV/Si IV components. Further, all of our sightlines pass through several kpc of gas, whereas the sightlines to the stars typically are only 1–3 kpc long. This will produce more blending between structures at different distances/velocities for the AGN sightlines. Nevertheless, we find that the distributions of the widths of the O VI and N V lines in sightlines through the Thick Disk are very similar to those in sightlines through the disk. We also find that the C IV/Si IV lines are narrower, but we do not find the very narrow components seen in the disk. This is not necessarily a result of the poorer resolution of our spectra (6.5 km s^{-1} vs 3.5 km s^{-1}), since lines that are 20 km s^{-1} wide should still have been resolved. Thus, the presence of narrow C IV/Si IV absorption components may

indicate a real difference between low- and high-latitude sightlines. It may also be due to the longer pathlength through the disk for the AGN sightlines. Or it may be caused by the limitations of the lower S/N ratio in the extra-galactic sightlines.

4.4.   Signature of Galactic rotation

In order to determine whether the velocity of the absorbing gas reflects Galactic rotation, we use the kinematical model described in Sect. 4.2, but added an exponential density distribution having scaleheight 2.6 kpc. We then find the velocity and density along the sightline in steps of 0.2 kpc, convert this density to an optical depth and add a gaussian with FWHM 60 $\mathrm{km\,s^{-1}}$. Summing over the path produces a predicted apparent column density profile, from which a centroid can be calculated. We look at two versions of this model, one in which the coronal gas co-rotates with the disk at all heights above the plane and one in which there is a decrease in the rotation velocity of 10 $\mathrm{km\,s^{-1}}$ per kpc. The latter is inspired by the results of e.g., Fraternali et al. (2004), Heald et al. (2006, 2007) and Oosterloo et al. (2007), who find that in several nearby spiral galaxies Hα and H I emission show gradients of $\sim$15–25 $\mathrm{km\,s^{-1}\,kpc^{-1}}$ at heights more than 1 kpc above the plane. Since in reality the distribution of the transition temperature gas is highly irregular, the only justified use of this model is to give an expectation value for the centroid of the absorption profile, but it cannot be used to model the individual absorption profiles.

Using our model, we find that galactic rotation does have a subtle, but measurable effect on the centroids of the profiles. This can be seen in Figure 5, which shows the observations, and the predictions for a co-rotating corona as well as those for a corona with a vertical veloc-ity gradient. The differences between the observations and these two models are also shown. The panels on the left give this for low latitude sightlines, while those on the right are valid for sightlines at high latitudes. For the high latitude sightlines we expect to see little to no systematic variation with longitude in the centroid velocity, which is indeed observed to be the case. At low latitudes, the co-rotating corona predicts centroids to be about -40 $\mathrm{km\,s^{-1}}$ near $l=90°$, and about $+30$ $\mathrm{km\,s^{-1}}$ near $l=270°$, while the model with a 10 $\mathrm{km\,s^{-1}\,kpc}-1$ ver-tical velocity gradient predicts values of about -60 and $+60$ $\mathrm{km\,s^{-1}}$, respectively. Increasing the gradient to 20 $\mathrm{km\,s^{-1}\,kpc^{-1}}$ increased this range to about ±70 $\mathrm{km\,s^{-1}}$. The observations appear more in line with the co-rotating corona version of the model. Excluding the two outliers at $l>300$ $\mathrm{km\,s^{-1}}$ (ESO 141$-$G55 and PKS 2005$-$489), the average difference between predicted and observed centroids is 5 $\mathrm{km\,s^{-1}}$, with an rms spread of 16 $\mathrm{km\,s^{-1}}$ (see panel (c)). From Figure 5 we conclude that Galactic rotation does leave an imprint on the velocities of the highly-ionized atoms. However, the effect is subtle, leading to centroids differing from
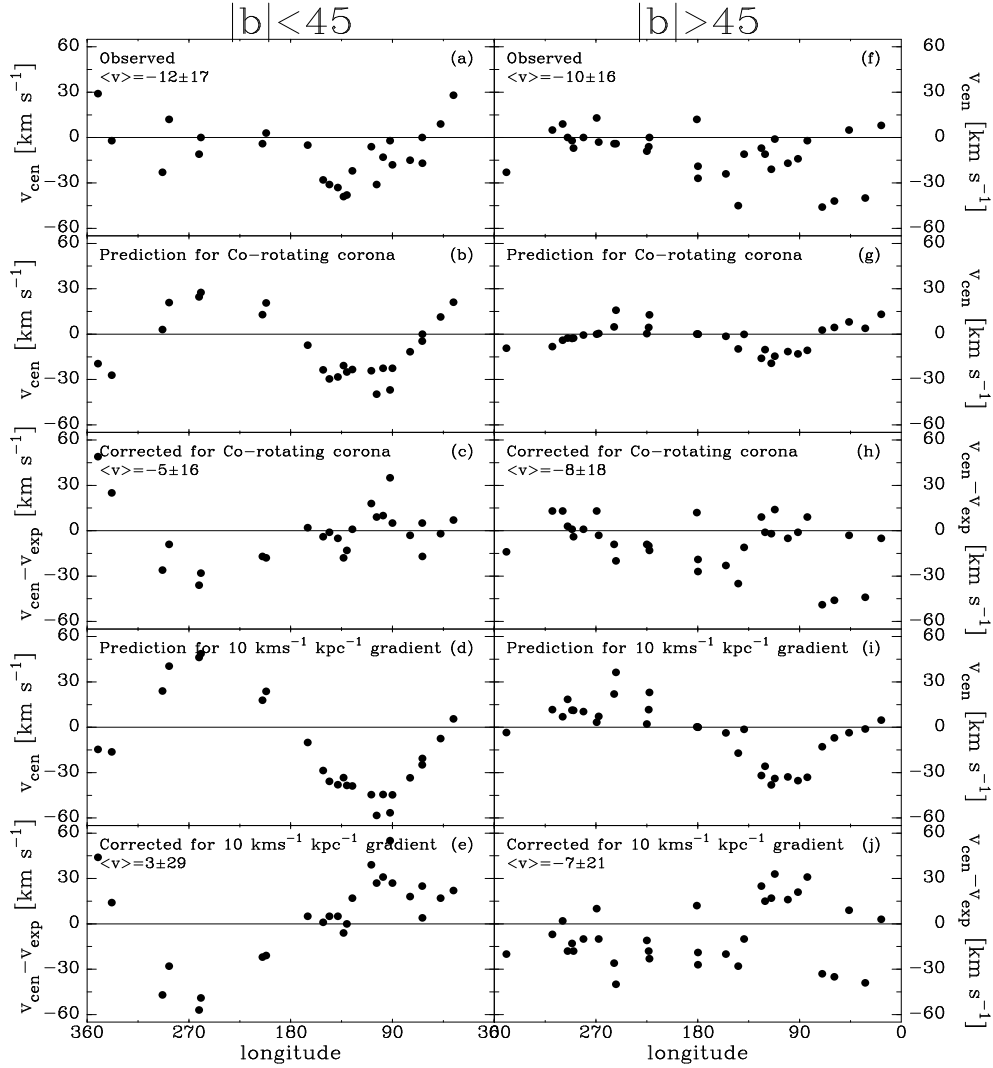
Fig. 5.— Comparison of observed and expected centroid velocities of the profiles of absorption by highly-ionized atoms, as function of longitude. Panels on the left are for sightlines at low latitudes ($|b|<45°$), panels on the right are for high latitudes. The top panels give the observations for O VI. The second and third panel give the predictions and difference between observed and predicted values for a co-rotating corona, while the bottom two panels give this for a corona having a 10 km s^{-1} decrease in velocity per kpc away from the Galactic mid plane.

$0 \ \mathrm{km\,s^{-1}}$ by no more than $40 \ \mathrm{km\,s^{-1}}$.

The assumed vertical distribution of the average density of the transition temperature has a large influence on the resulting predictions for the centroid velocities. If we were to assume that the density of the transition temperature gas is constant between 0 and several ($\sim$5) kpc above the Galactic plane, we would predict very little difference between a co-rotating corona and one with a vertical gradient, but the centroids would have values up to $\pm 50 \ \mathrm{km\,s^{-1}}$ (i.e. much larger than what is observed). If we instead assume a scaleheight of 0.5 kpc, the predicted centroids would range between $\pm 10 \ \mathrm{km\,s^{-1}}$ for a co-rotating corona and between $\pm 30 \ \mathrm{km\,s^{-1}}$ for one having a $10 \ \mathrm{km\,s^{-1}\,kpc}-1$ vertical gradient. The predictions for the latter case are about as good as the ones for our standard model.

Thus, it is possible to exclude a model in which the transition temperature extends to very large heights above the plane. However, it is not really possible to differentiate between a model with a co-rotating corona and a scale height of 2.6 kpc and a corona with a vertical velocity gradient and a scale height of 0.5 kpc. On the other hand, using the fact that the directly derived scale height is about 2.6 kpc, we can conclude that the transition temperature gas appears to be co-rotating up to heights of a few kpc.

4.5. Column density distribution

Figure 6 presents the distributions of the column densities for the different ions. For each ion we show the total Galactic column density in the top panel and the column densities of the individual components in the bottom panel. Upper limits are indicated by the hatched areas. In the bottom panel of each pair, the dotted vertical line shows the column density detection limit corresponding to a line with 20 mÅ equivalent width and FWHM $40 \ \mathrm{km\,s^{-1}}$. Such an equivalent width is the detection limit when integrating over a $75 \ \mathrm{km\,s^{-1}}$ window in data with an S/N ratio of about 20. These limits are 13.2 dex for O VI, 13.0 dex for N V, 12.7 dex for C IV, 12.4 dex for Si IV, 13.4 dex for Fe III and 13.7 dex for S III. Clearly, except for N V, the typical detection limit is 0.6 dex to 1.1 dex below the average component column density, making these lines always easily detectable. For N V the detection limit is usually only about 0.3 dex below the typical value, which is mostly caused by the fact that the interstellar abundance of nitrogen is about 0.8 dex less than that of oxygen and carbon. Therefore, although N V is detected in 43 Galactic components, for 46 components only an upper limit is possible. In contrast, an upper limit is found for O VI, C IV and Si IV in just 3, 3 and 4 components, respectively.

Savage et al. (2003) derived an average Galactic O VI column density of 14.32$\pm$0.19,

which is basically the same as the value of 14.31±0.20 found here. They also looked at the average value of $\log N(\text{O VI})\sin|b|$, which is 14.21±0.23, or about 0.11 dex lower. We do not show the distributions of $\log N(\text{O VI})\sin|b|$ separately, as they are very similar to the ones shown in Figure 6, but shifted to column densities that are ∼0.15 dex lower. The spread in the column densities of highly-ionized atoms is such that for 95% of the sightlines the integrated column density is within a factor ∼2.5 from the average. I.e., not only is the transition temperature gas widespread, *on average* it is fairly evenly distributed.

The histograms in Fig. 6 show that along paths through the Galactic Thick Disk, O VI, C IV and Si IV are always found. Only N V is sometimes missing, which is most likely due to the fact that the line is weaker, which in turn in due to the fact that the cosmic abundance of nitrogen is lower than that of oxygen and carbon. To calculate the average and dispersion of the distribution of $N(\text{N V})$, we only use the detections, and exclude the upper limits. We justify this on the basis of the fact that generally the ratio N V/O VI has a narrow range (see Sect. 4.8 below) and in sightlines where N V is not detected the implied limit to the N V/O VI ratio is within the range of detected values or above it. That is, given $N(\text{O VI})$ and N V/O VI, the non-detection of N V is generally not significant. There are only five (out of forty) components for which the measured upper limit on the ratio N V/O VI is slightly more than 2σ below the average ratio; i.e., based on $N(\text{O VI})$, a detection of N V would have been expected.

4.6. Sky distribution

Savage et al. (2003) discovered that the O VI column density is systematically enhanced in the northern sky relative to the southern sky, but they did not see a systematic dependence of $N(\text{O VI})$ on longitude. To be precise, they found an average for $\log N(\text{OVI})\sin|b|$ of 14.26 for $b>0°$ and 14.09 for $b<0°$. We can now refine this conclusion.

In Figures 7 and 8 we show the logarithmic column densities of the six ions as a function of Galactic longitude. In Figure 8 we further include curves showing the expected change of column density with latitude for a plane-parallel layer (i.e., $\log N(90°)\sin|b|$).

When looking at Figures 7 and 8 (at first ignoring the colors), it appears that sightlines with high column density occur relatively more often at longitudes within $30°$ of $l=0°$, with about a factor of two difference between directions near $l=0°$ vs directions near $l=180°$. This effect is not seen in the column densities of Fe III or S III. Further, sightlines at $b>45°$ tend to lie above the blue $\log N(90°)\sin|b|$ line. When exploring this further, we found that column densities are generally enhanced near the Galactic Center and near the Galactic north pole.
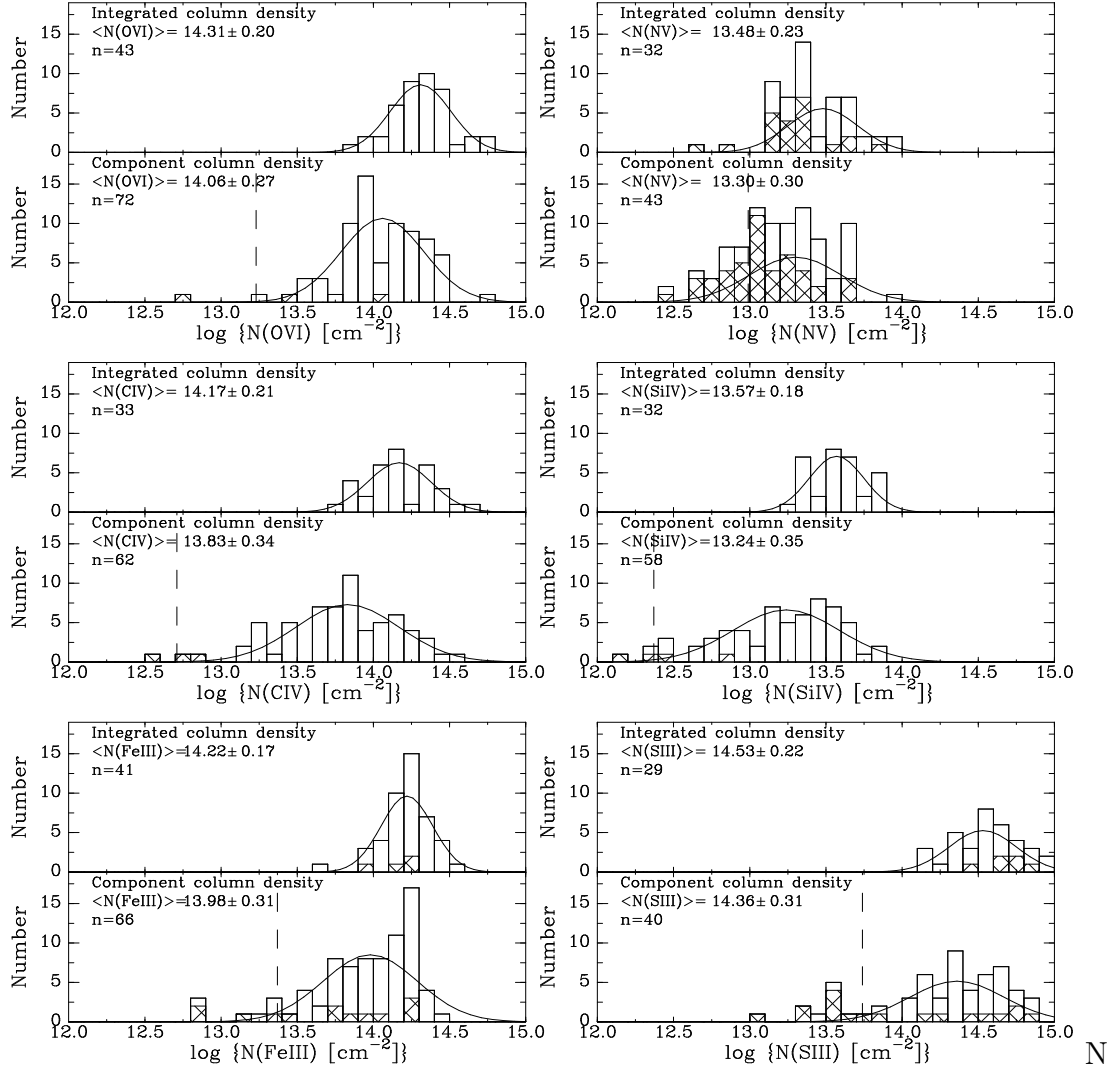
Fig. 6.— Distributions of column densities for the four high- and two intermediate-ionization species. The top panel of each pair is for the integrated column densities, the bottom panel for the individual components. The hatched parts of the histograms correspond to upper limits. The dotted vertical lines in the bottom panels show the detection limit for a 20 mÅ line with FWHM 40 km s^{-1}, while the curves are gaussians using the parameters listed in the label (i.e., number, average and dispersion). Limits were excluded in these calculations (see text for a discussion of why this is justified in the case of N V).

Further, O VI is deficient in parts of the southern sky. These regions are delineated in Figure 9. We note that there are about 100 additional sightlines toward which N(O VI) can be measured. These sightlines include the ones that were in the original *FUSE* O VI survey (Wakker et al. 2003) as well as sightlines observed between 2003 and 2007. We have not yet measured each of these with the same care as the sightlines in this paper, but a preliminary assessment shows that for these additional sightlines O VI column densities are also enhanced in the region of excess and depressed in the region of deficit defined by the sightlines measured in this paper. In Figures 7 and 8 we show the points in the region with enhanced column densities in red. It is clear from these figures that the excess column density seen in O VI in the region around the Galactic Center is also seen in the other ions. Comparing the average $\log N \sin|b|$ for the region with an excess to those in the "normal" sky gives differences in the logarithm of the polar column densities of 0.20, 0.36, 0.31, 0.26, 0.21 and 0.29 dex for O VI, N V, C IV, Si IV, Fe III and S III, respectively. That column densities are enhanced over the Galactic Center suggests the presence of enhanced activity. It is more difficult to explain the 0.17 dex deficit seen in N(O VI) in the southern sky, especially since it is not reflected in any of the other ions.

The total hydrogen column corresponding to each ion can be estimated from $\log <N \sin|b|>$ $- \log Af$, with $\log<N \sin|b|>$ the logarithm of the average polar column density (see Figure 8 for the values), A the element abundance and f the ionization fraction. The maximum ionization fraction of the ions is on the order of 20% at temperatures near 10^5 K (see e.g., Gnat & Sternberg 2007). We take f=10%, and use solar abundances of $\log A$=-3.31 for oxygen, -3.57 for carbon, -4.17 for nitrogen and -4.49 for silicon (Asplund et al. 2009). Then, the average polar column densities (logarithmic values 14.17, 13.22, and 13.94 for O VI, N V, and C IV, respectively) imply $\log N$(H,eqv)$\sim$18.4 for the transition temperature gas. This number can be compared to the total neutral hydrogen column density ($\log N$(H I)$\sim$20.28) and total ionized hydrogen column density ($\log N$(H$^+$)$\sim$20.0) (Savage & Wakker 2009).

We note that Savage et al. (2003) compared the distribution of O VI column densities to that of the radio-continuum loops and X-ray emission. They found no obvious correlation. We rechecked these comparisons and we still see no clear relation between N(O VI) and other known structures. We also compared the pattern of the column densities and velocities to the distribution on the sky of the high- and intermediate-velocity H I clouds (see Wakker 2004 for sky maps of these objects). In the north, a large part of the sky at l=100° to l-240°, b>30° is covered by negative-velocity gas ($v\sim$−40 to −90 km s^{-1}), in three structures called the "Intermediate-Velocity Arch", the "Intermediate-Velocity Spur" and the "Low-Latitude Intermediate-Velocity Arch" (as named by Kuntz & Danly 1996). Although the O VI absorption in this part of the sky tends to have negative centroids, O VI absorption with negative centroids occurs both on and away from these H I structures, and there

is no clear correlation. Furthermore, the region of sky where the excess high-ion column density is seen covers area both overlapping with and away from the intermediate-velocity gas. However, some connection between the two phenomena would be logical, since the intermediate-velocity clouds (IVCs) are about 1 kpc above the Galactic plane (Wakker 2001), which is similar to the scale height of the transition temperature gas. The connection clearly does not manifest itself as a simple correlation between the column densities of the neutral and transition temperature gas, but must be more complex. Understanding the connection will require many more sightlines toward which the highly-ionized species are detected, and/or maps of the emission from these ions.

We further looked at the difference between absorption at negative velocities and absorption at positive velocities, although comparison suffers from having just 30 to 40 sightlines for which this can be done. We made this comparison in many ways, looking at northern vs southern sightlines, sightlines inside and outside the region of the O VI excess, etc, but we found only one (small) possible systematic difference. This is that the column densities at negative velocities appear to be marginally larger than those at positive velocities, by 0.10, 0.03, 0.22 and 0.26 dex for O VI, N V, C IV and Si IV, respectively. In the region of the sky with excess total column density, these differences are 0.07, 0.16, 0.25 and 0.20 dex, while in parts of sky away from the excess or deficit region the differences are 0.19, 0.05, 0.23 and 0.31 dex. However, in the region with the O VI deficit, the differences are -0.15, -0.17, 0.12 and 0.15 dex. Since the dispersions in the averages are about 0.20–0.25 dex, these differences are generally only about 0.5 times the spread, which according to the t-test is barely significant (probability of it happening by chance 2%). However, all for four ions the column density at negative velocities appears to be slightly larger than that at positive velocities, so the effect is probably real.

4.7. Scale heights

The issue of the scaleheights of the different high-ionization species was addressed by Savage & Wakker (2009). They combined column density measurements from a number of sources. Data from the *Copernicus* and *FUSE* satellites was used to derive O VI column densities toward stellar and extragalactic targets (using measurements by Jenkins 1978b, Zsargó et al. 2003, Wakker et al. 2003 and Bowen et al. 2008). *HST* spectrographs provided Al III, Si IV and C IV spectra for a number of extragalactic targets, while *IUE* (the *International Ultraviolet Explorer*) was used to measure these ions in stellar spectra and toward Magellanic Cloud stars (Savage et al. 2001b). The total sample included 109 stars and 30 extragalactic objects, all having reliable data.
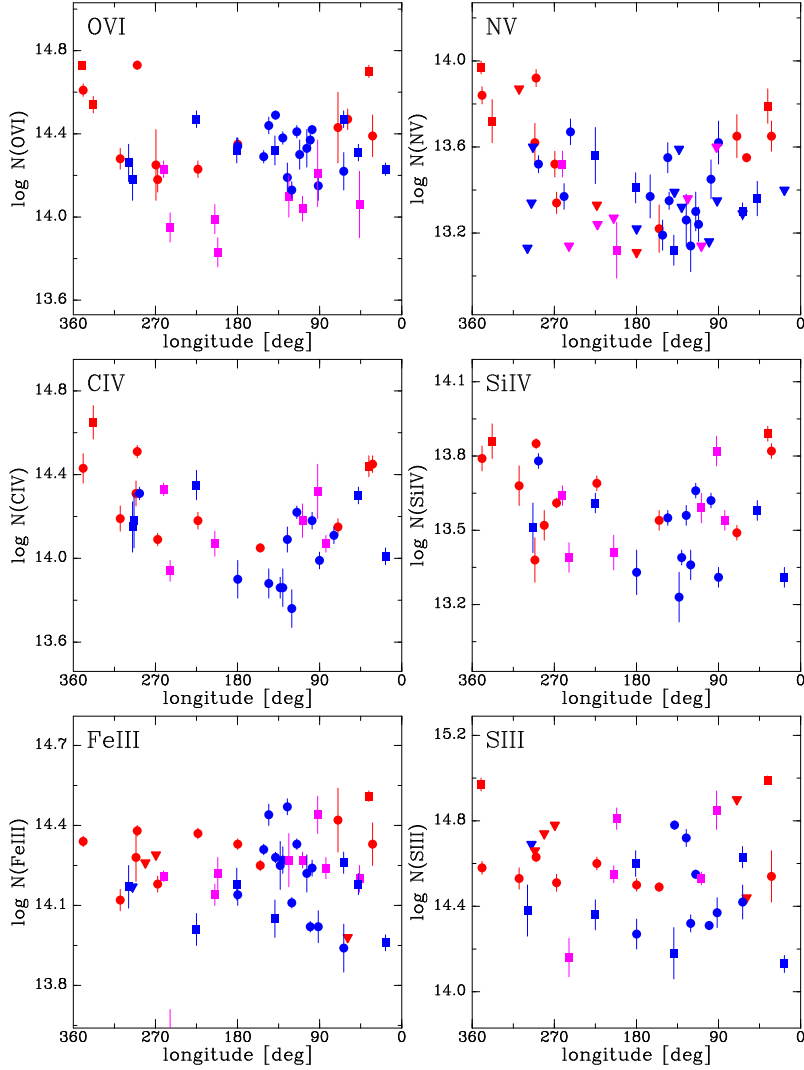
Fig. 7.— Scatter plot of ionic column densities against Galactic longitude. Circles are for sightlines with $b>0°$, squares are for sightlines with $b<0°$. Triangles correspond to upper limits. Red points are for sightlines where $N(\text{O VI})$ is systematically enhanced (an area of sky delineated as $|l|<40°$, $|b|<50°$ combined with $|l|<80°$, $b>40°$). Purple points are for sightlines showing a systematic deficit in $N(\text{O VI})$ (approximately l=70 to 280°, b=−60 to −10°) and blue points cover the rest of the sky.
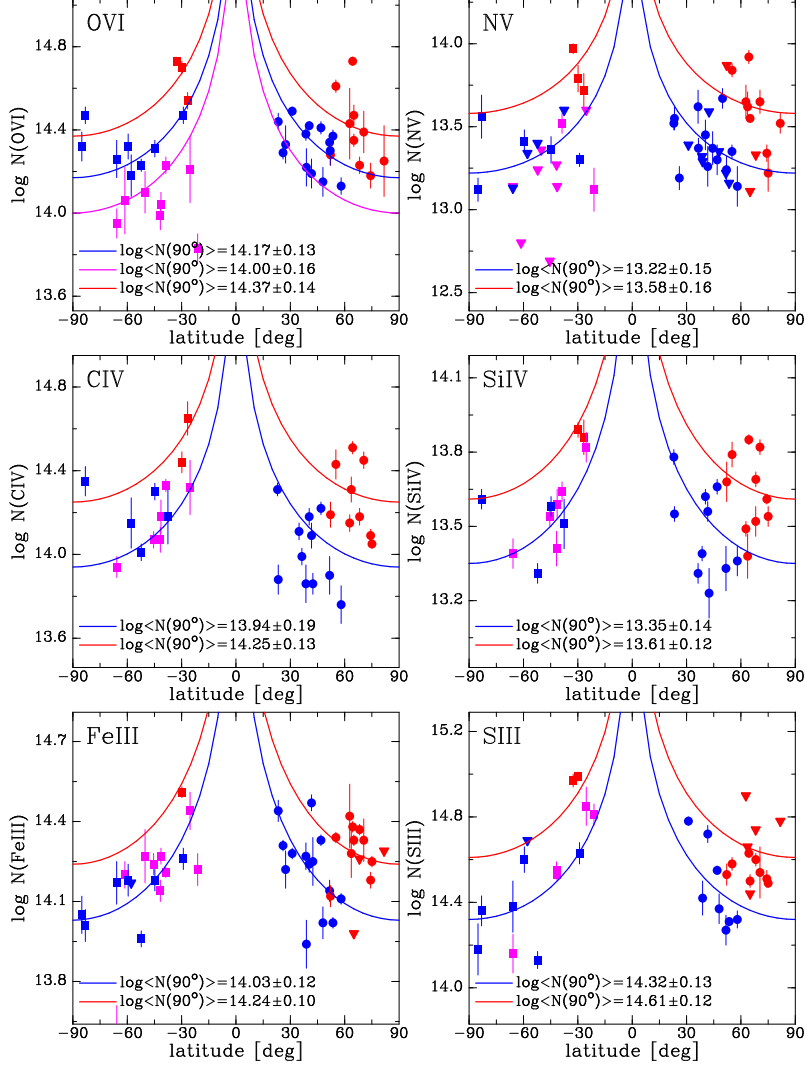
Fig. 8.— Scatter plot of ionic column densities against Galactic latitude. Symbol types and colors are the same as in Figure 7. In each plot we also give a curve representing the $N(90°)\sin|b|$ distribution of column densities that would result from a plane-parallel layer, with the values of the corresponding polar column densities given in the lower left corner of each panel.
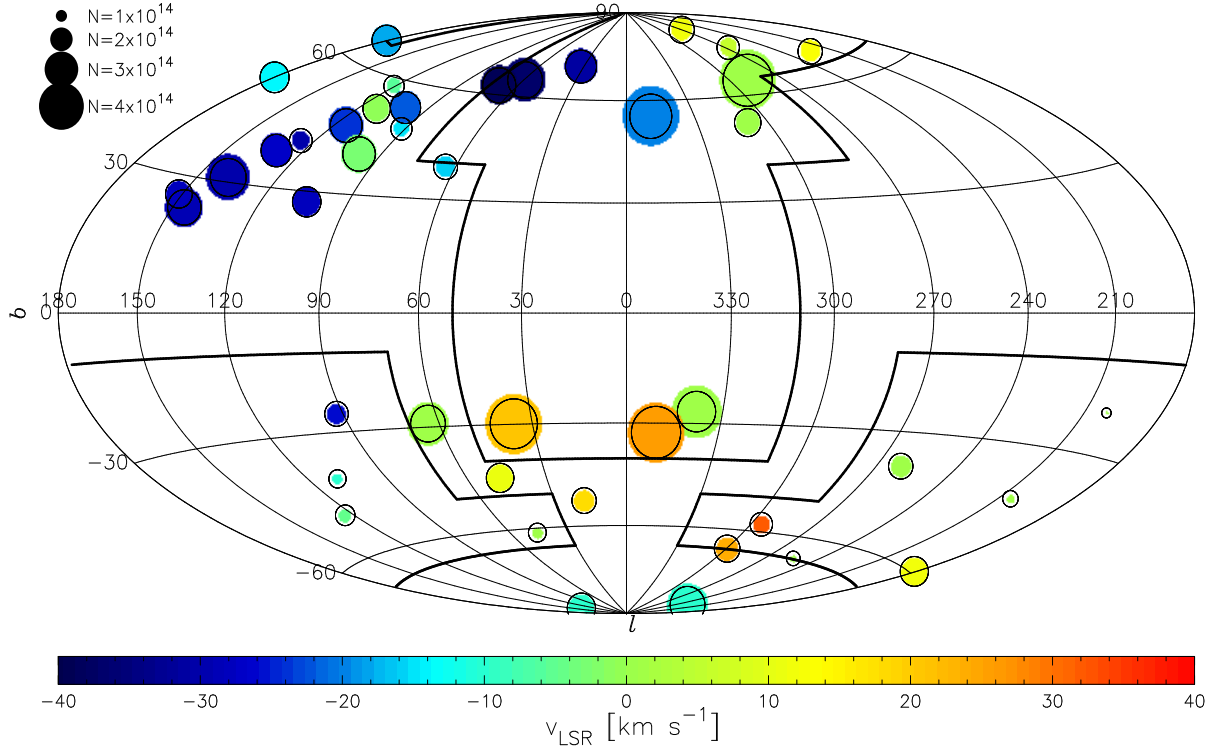
Fig. 9.— All-sky map of the O VI column density and centroid velocity, in aitoff projection, centered on the Galactic Center. Colors correspond to the centroid velocity of the Galactic O VI absorption, following the scale on the bottom. Symbol diameters are proportional to the value of N(O VI), following the legend in the upper left corner. The thick lines outline the regions with an excess or deficit in the O VI column density.

Using AGNs at $-90°<b<45°$ (i.e., omitting the region with O VI excess), Savage & Wakker (2009) derived scaleheights of 2.6 ± 0.6 kpc for O VI, $3.6^{+1.0}_{-0.8}$ kpc for C IV, and $3.2^{+1.0}_{-0.6}$ for Si IV. They argued that the slightly smaller O VI scaleheight compared to C IV and Si IV is consistent with predictions of hybrid coronal gas models in which these ions are produced by collisional ionization in cooling transition temperature gas, but with photoionization from the extragalactic background radiation increasing the amount of C IV and Si IV at high z. They also found that C IV and Si IV are relatively tightly correlated, with an average logarithmic ratio Si IV/C IV$= -0.60\pm0.11$ in the Thick Disk.

With the new set of measurements for N V, we also tried to apply the methods of Savage & Wakker (2009) to derive a scaleheight for N V, using data from the literature for measurement of N V toward disk stars (as listed by Savage & Wakker (2009) and complemented by values from Lehner et al. (2011). However, a fair comparison between the different scaleheights requires using the same set of stars and the same selection criteria for all ions. This results in a sample of N V measurements that is too small to give a reliable answer. With somewhat less restrictive criteria, the derived scaleheight for N V is similar to that of O VI and C IV. A proper assessment of the N V scaleheight will require more data, however.

The fact that both the linewidths and the scaleheights of C IV and Si IV are comparable and that their centroids are very well aligned is strong evidence in favor of the hypothesis that these ions originate in the same parcels of gas. Comparing to O VI we find that the scaleheight of O VI is slightly smaller, while the extent of the O VI absorption tends to be slightly wider, but the centroids of the O VI and C IV/Si IV are similar. The most likely explanation for these similarities and differences is that the O VI is associated with the same structures in which C IV and Si IV originate, but near the plane the O VI-containing gas is slightly more turbulent, while as one goes up, the fraction of O VI-containing gas decreases.

4.8. Line ratio histograms

Figure 10 shows the distributions of all ratios between the four highly-ionized species, as well as two ratios involving Fe III, for the absorption components where the derived ratio is flagged as being reliable. The panels on the left side give the distributions of the logarithms of the ratios, the panels on the right show the ratios linearly. The labels give the average ratio and its dispersion, excluding from the calculation some outliers, which are discussed below.

For the most part these distributions are rather narrow. In particular, the histograms of $\log$ (N V/O VI) and $\log$ (Si IV/C IV) have a dispersion of only 0.14 dex ($\pm40\%$), with a
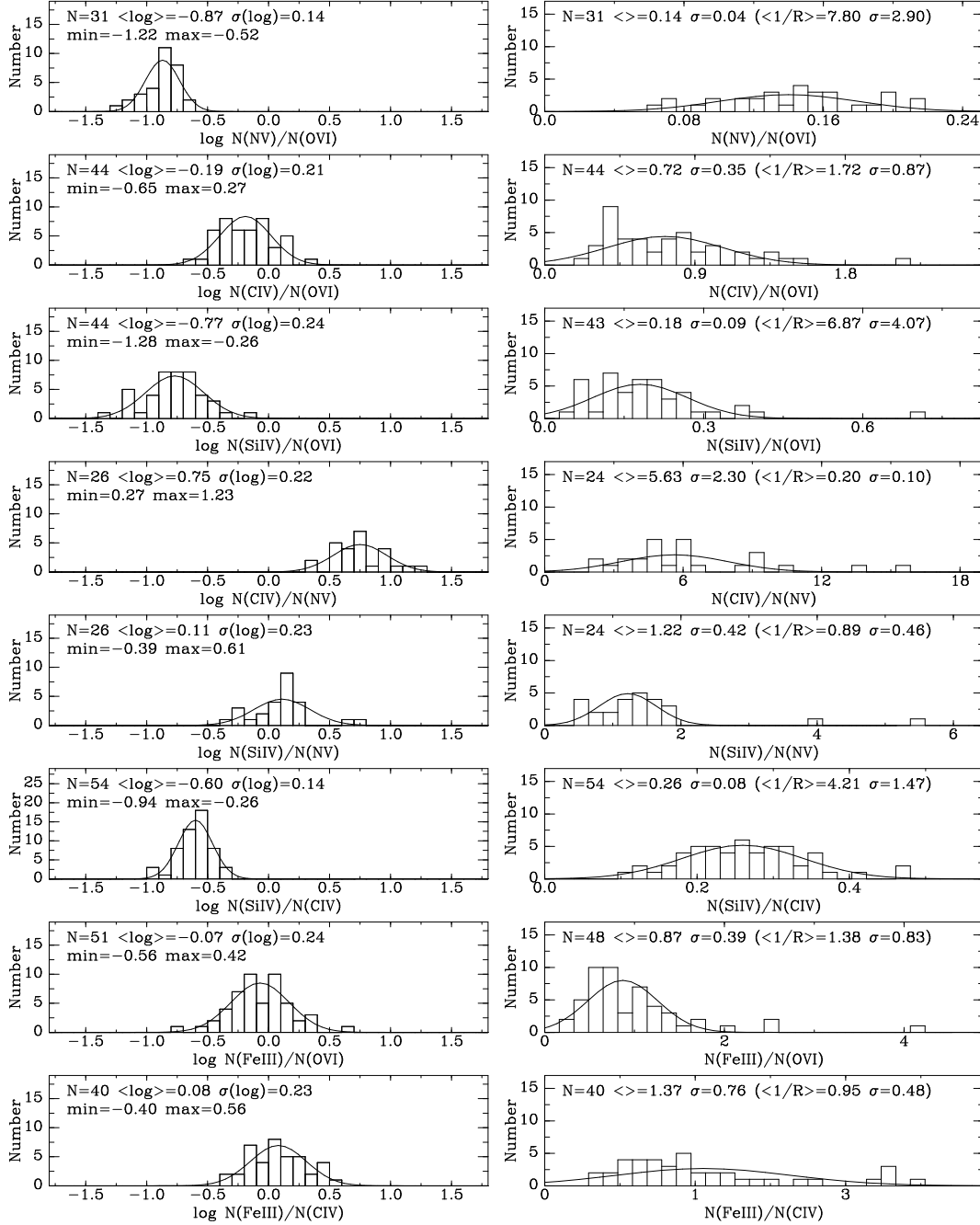
Fig. 10.— Histograms of the distribution of the logarithmic (left panels) and linear ratios (right panels) between O VI, N V, C IV, Si IV and Fe III. The number of measurements (N), average ($<\log>$) and dispersion ($\sigma(\log)$) of each ratio distribution are given in the top left corner. The second line gives the range of values. Gaussians with the listed parameters are overlaid. To make comparisons with other papers easier, in the panels on the right, the average linear ratio and its dispersion are given, as are the average and dispersion of the distribution of the inverse ratio. E.g., the average ratio of N V/O VI is 0.14, while the average ratio of O VI/N V is 7.80.

spread between the highest and lowest ratio of just 0.6 dex, or a factor $\sim$4. The dispersions in the distributions of $\log\,(\text{C IV/O VI})$, $\log\,(\text{Si IV/O VI})$, $\log\,(\text{C IV/N V})$, and $\log\,(\text{Si IV/N V})$ are $\sim$0.23 dex (70%), significantly larger than those in $\log\,(\text{N V/O VI})$ and $\log\,(\text{Si IV/C IV})$. This again supports the notion that O VI and N V originate together, as do Si IV and C IV, but although the two pairs of ions live in the same structure, they are not fully co-spatial. The median error in each individual ratio is about 0.10 dex. Thus, in the case of N V/O VI and Si IV/C IV, the observed dispersions in the distributions may reflect the observational uncertainty more than an intrinsic spread. For the other ratios there clearly are variations across the sky.

Previous determinations of these line ratios were presented by Sembach & Savage (1992), who measured N V, C IV and Si IV toward 12 high-z stars. They listed an average C IV/N V ratio of 4.6$\pm$2.7, where we find 5.6$\pm$2.3, using 24 components. For C IV/Si IV they found 3.6$\pm$1.3, compared to our value of 4.2$\pm$1.5. Indebetouw & Shull (2004b) also presented average ionic ratios, giving $\log\,(\text{N V/O VI})=-0.83\pm0.28$ (34 sightlines) and $\log\,(\text{C IV/O VI})=-0.28\pm0.18$ (11 sightlines), compared to our results of -0.87 ± 0.14 (31 components) and -0.19 ± 0.21 (44 components) for these ratios. I.e., we find similar values for C IV/O VI, but a much narrower distribution for N V/O VI, which in large part can be explained as the result of the very different velocity ranges over which the lines were integrated.

5. Ionization mechanisms

The comparison between two line ratios can be a great tool to diagnose the physical conditions in the gas giving rise to the high-ionization absorption. In earlier work the diagnostic value of ionic ratios was often pointed out (e.g. Sembach & Savage 1992; Spitzer 1996; Savage et al. 1997b), and the observed values of e.g., C IV/O VI or C IV/N V were compared with model predictions. However, the diagnostic power of the ratio-ratio diagram (first discussed by Indebetouw & Shull 2004a and Fox et al. 2004, 2005) was only fully appreciated after *FUSE* O VI data became available to complement STIS observations of C IV, N V and Si IV.

In this section we summarize the potential ionization mechanisms and compare the resulting predictions for ionic ratios and ionic column densities to the observations. Much of this has been done in one form or another in previous papers. However, unlike previous authors, we describe more explicitly the actual predictions in the different papers in which a given model is calculated, rather using a simplified range of possible values for the ratios. Further, for some processes (CIE, turbulent mixing) revised models were published fairly

recently, using updated atomic parameters. We also include three calculations that traditionally have not been part of such an overview: Thick Disk supernovae (Shelton 1998), static non-equilibrium radiative cooling (Gnat & Sternberg 2007), and cooling flows (described below). In the case of the last of these, we present this model in a journal paper for the first time, although the predictions were summarized in a conference paper (Shapiro & Benjamin 1991). Further, we include a new numerical model for turbulent mixing, which includes non-equilibrium ionization (Kwak & Shelton 2010).

This set of mechanisms does not exhaust the range of ideas published in the literature. Indebetouw & Shull (2004a) also list as possibilities evaporating shells, stellar wind bubbles, supernova remnants, and photoionization by white dwarfs. However, some of these appear unlikely because they predict ionic ratios that are very different from the observed values, or because one would expect a small covering factor or large variations in column density across the sky since objects like stellar wind bubbles and white dwarfs have a small volume filling factor.

Historically, different elemental abundances have been used to create the different models. This is because the standard reference values of the solar abundances of most elements (but especially C, N and O) have varied since 1980, as determinations improved or problems with the interpretation of solar absorption lines were corrected. We therefore adjusted the published predictions of ionic column densities to reflect the most recent values for the solar abundances of C, N, O and Si (Asplund et al. 2009: $\log A$(C, N, O, Si)$= -3.57, -4.17, -3.31$ and -4.49, respectively). However, this adjustment is not a simple scaling, as to first order the O VI column density is independent of metallicity, as the cooling is dominated by the oxygen ions. Thus, a lower oxygen abundance results in less efficient cooling, causing a larger region with transition temperature gas, giving a fixed O VI column density. The column densities of other ions then scale with the change in the *ratio* of elemental abundances. A different situation prevails in the turbulent mixing model, where the heating up of cold gas is important. In that case the column densities of the highly-ionized atoms *do* scale directly with the elemental abundances.

We compare the models to the data in Figures 11a, b, c and d, which plot four combinations of ratios. Figure 11a shows N V/O VI against Si IV/C IV, i.e. the ratios for the pairs of ions that seem to originate in the same regions of the ionized structures in the sightline. Figure 11b gives N V/O VI against C IV/O VI which represents a more global comparison through the ionized structure, with the x-axis relevant for the hottest gas and the values in the vertical direction influenced by the relative amount of the two different regions in the structure. In Figure 11c we show C IV/O VI against Si IV/CIV, which focuses on the cooler regions. Finally, Figure 11d presents C IV/N V against Si IV/C IV, equivalent to Figure 11c,

but chosen by bearing in mind that COS spectrograph on *HST* is producing many additional spectra of QSOs that will include data for N V, C IV and Si IV, but not for O VI.

5.1.   Observed ionic ratios

The filled datapoints in Figure 11 represent the ratios (or limits, shown by triangles) in the individual components of the Galactic absorption profile. We draw a box around the datapoints which represents the $\pm 2\sigma$ range around the average.

To determine whether our measurements for the highly-ionized gas in the Milky Way corona are representative, we also looked at the measurements in other environments: the Galactic disk, high-velocity clouds, and high-redshift damped Lyman-alpha (DLA) absorbers. We discuss each of these below.

For the Galactic disk we used the measurements of highly-ionized atoms toward 38 stars by Lehner et al. (2011), shown by open stars in Fig. 11. In most cases O VI, C IV and Si IV can be measured, while a value or upper limit is given for N V in 22 sightlines. Lehner et al. (2011) present a table of the integrated column densities, as well as one for component column densities. However, for the latter the different ions are not explicitly matched up, and a few times the fitted component structure differs for e.g. C IV versus O VI. In many sightlines the stellar continuum is difficult to define, especially for N V and O VI. Toward many stars the N V line is also relatively noisy. In other sightlines the C IV and/or Si IV lines are extremely deep and show evidence for saturation, making the derived column densities suspect, and indeed in every one of those cases the Si IV/C IV ratio is found to lie about 0.3 dex outside the range found at high latitude toward AGNs. In a number of cases the apparent interstellar O VI profile strongly differs from the C IV/Si IV profiles, which may indicate the presence of stellar absorption lines. Reassessing the Lehner et al. (2011) sample, we decided to keep only the 12 sightlines where the stellar continuum is relatively clean and toward which the interstellar absorption lines are not saturated. These are the stars given number 1, 2, 6, 10, 11, 12, 13, 14, 27, 33, 35 and 38 in the Lehner et al. (2011) list. With this restriction of only including measurements for stars with unsaturated and unambiguous absorption, the ratios for these disk sightlines fall completely within the box determined from the extragalactic targets (with the exception of N V/O VI toward HD 99857, which is 1.5σ outside the box), indicating that the physical conditions in the transition temperature gas do not change much with height above the Galactic plane.

Another kind of cloud in which highly-ionized gas is often detected are the high-velocity clouds (HVCs). Fox et al. (2004, 2005, 2010) and Collins et al. (2004, 2005) analyzed these

lines toward the two largest HVCs (complex C and the Magellanic Stream). Sembach et al. (2003) presented measurements of O VI in 84 HVCs seen in sightlines toward extra-galactic targets, while Lehner & Howk (2010) find highly-ionized high-velocity clouds toward several galactic stars. Each of these papers shows a small subset of the total available data. In order to look at the ionic ratios in the HVCs, we therefore measured O VI, N V, C IV and Si IV in each of the sightlines used in this paper. The full results will be presented in a future paper on highly-ionized gas in HVCs. We find that detecting N V in HVCs is rare, but out of about 25 limits that can be formed for N V/O VI only three fall outside the observed range for Milky Way coronal gas. Similarly, of the about 20 HVCs in which C IV and O VI are both seen, the ratio falls in the observed range for the Milky Way coronal gas. In the case of Si IV/C IV this is true for all but two of the $\sim$25 possible ratios. The two exceptions are clouds with relatively narrow lines, where it appears likely that photoionization plays a role.

===

[FIG 11A CAPTION CONTINUED]

MODELS: (a) Black line (label: CIE): ratios in collisional ionization equilibrium, as calculated by Gnat & Sternberg (2007), for temperatures ranging from $\log T$=5.4 to $\log T$=4.4. (b) Magenta lines (label: Static Cooling): non-equilibrium radiative cooling models from Gnat & Sternberg (2007) for temperatures ranging from $\log T$=5.4 to $\log T$=4.4, with a solid line for solar metallicity and a dotted line for two times solar metallicity; the line gets thicker at lower temperatures, where the gas spends more time; the gas traverses this trajectory in about $3\times10^4/n_0\,(\mathrm{cm}^{-3})$ yr. In these models the gas is not flowing, and there is no additional heat input or output. (c) Orange lines (label: Shock Heating): Dopita & Sutherland (1996) shock models, with shock velocities of 200 and 300 $\mathrm{km\,s}^{-1}$ for the no-magnetic-field case marked and connected by a thick line; The other three thick line segments connect the 200 and 300 $\mathrm{km\,s}^{-1}$ case for higher magnetic parameters, $B\,n^{-3/2}$=1, 2 and 4 $\mu\mathrm{G\,cm}^{-3/2}$. (d) Red lines (label: Conductive Interfaces): the Borkowski et al. (1990) conductive interfaces predictions; A "perpendicular" and a "parallel" symbol mark which of the two lines is for perpendicular or parallel magnetic field; the line thickness increases linearly with the age of the interface, 0.1 Myr at the thinnest point, 10 Myr at the other end, which is reached after
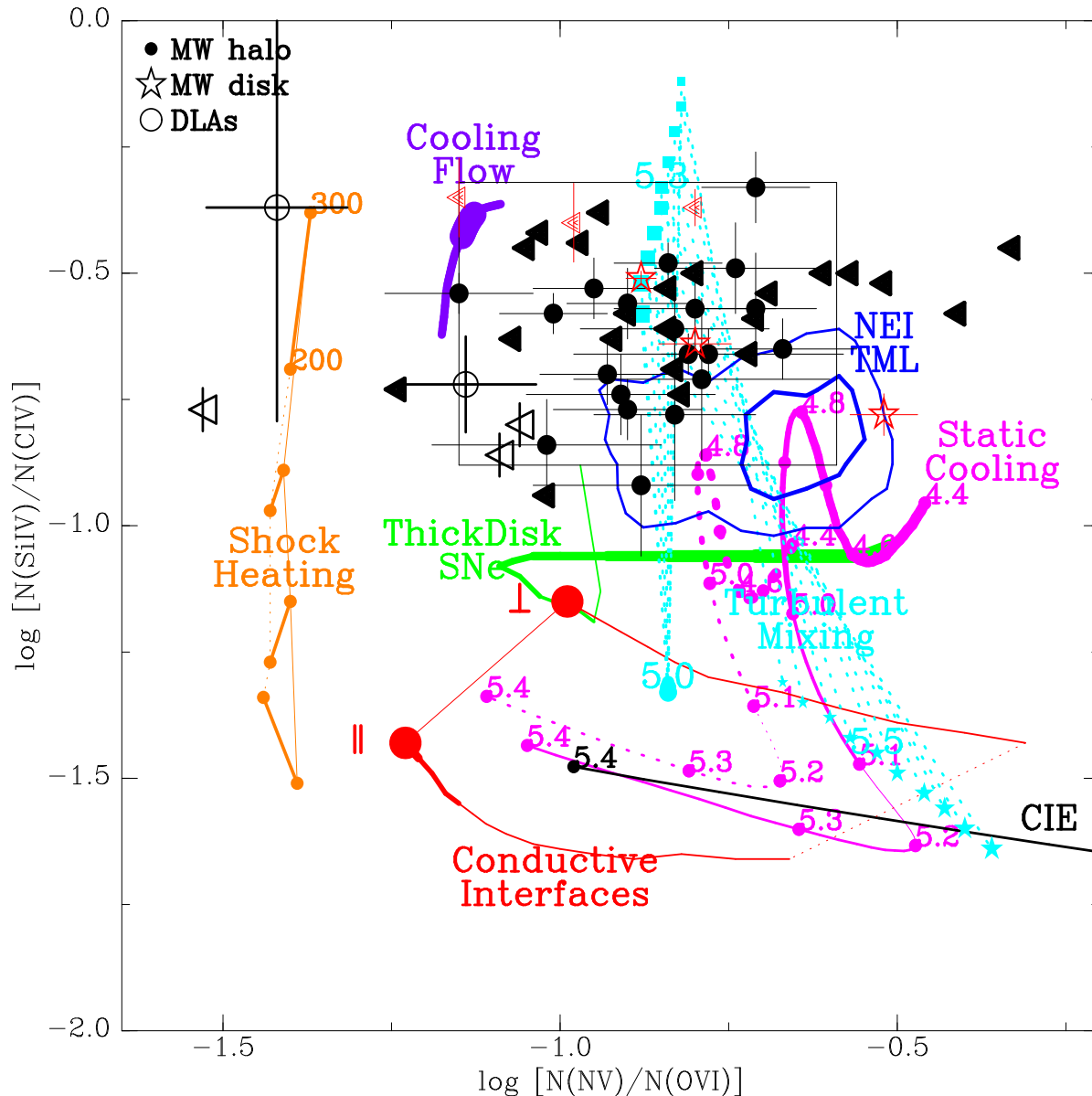
Fig. 11a.— Theoretical ranges and observed values for pairs of ionic ratios. DATA: Filled black circles show ratios in individual components, as determined in Section 3, black triangles show cases with one ratio measured, but the other ratio being an upper or lower limit. A black box outlines the region given by $<R>\pm\delta R$, where the average $<R>$ and spread δR of the ratio distribution can be found in Figure 10. Open red stars and red triangles represent the results of Lehner et al. (2011), limited to their stars numbered 1, 2, 6, 8, 9, 10, 11, 12, 13, 14, 23, 27, 28, 32, 33, 35 and 38, i.e., not including stars for which the lines are saturated, have very complex component structure or difficult to determine stellar continua. Open black circles and triangles represent measurements in DLAs at redshifts 2.0 to 3.1, as presented by Fox et al. (2007). Note that this selection leaves just six sightlines with measured values for N V, while in two other sigthlines O VI is missing; thus fewer than 12 symbols show up in each individual ratio-ratio plot.

1–2 Myr. As a result, the line for this model appears as a quickly-traversed thin red line ending in a large dot, where the ratios stabilize. (e) Green line (label: Thick Disk SN): the Shelton (1998) Thick Disk supernovae model (SNe occuring at heights up to 2 kpc), giving the evolution of the ratios with time (from 1 to 16 Myr in age), with the line thickness proportional to the amount of time spent at each point. (f) Light blue lines (label: Turbulent Mixing): predictions of the Slavin et al. (1993) semi-analytic turbulent mixing layer model; circles, squares and stars are shown for entrainment velocities ranging from 25 to 100 $\mathrm{km\,s^{-1}}$ at temperatures of $\log T$=5.0, 5.3 and 5.5, respectively; the symbol size is proportional to the entrainment velocity. (g) Solid blue contours (label: NEI TML): distribution of ratios in the Kwak & Shelton (2010) turbulent mixing layer models, corresponding to 256 column densities derived by integrating through an interface at 1 Myr intervals for ages between 20 Myr and 80 Myr. (h) Dark purple line (label; Cooling Flow): the predictions of the model by Benjamin & Shapiro that is described in the appendix. This model is applicable to cooling hot gas flowing through an interface. The range of flow velocities is 20–30 $\mathrm{km\,s^{-1}}$ (thicker part of the line) and 12–42 $\mathrm{km\,s^{-1}}$ (thinner part). For these flow velocities the absolute column densities are within 2 and 1 times the observed dispersion around the observed average value.

==

Open circles and triangles in Fig. 11 show the measurements of Fox et al. (2007) associated with a number of Damped Lyα Absorbers (DLAs) at redshifts 2.0 to 3.1. They found 12 absorption line systems in which at least three of O VI, N V, C IV and Si IV could be measured. If we use these results and derive ionic ratios, we find that the eight systems for which both Si IV/C IV and C IV/OVI can be calculated give ratios that fall in exactly the same range as the Milky Way results. N V, however, seems underabundant, with only three detections and five upper limits. In all of these cases $\log$ N V/O VI is <-1.1, which contrasts with the average value of -0.87 seen in the Milky Way.

The metallicities found in the neutral portions of these DLAs (as determined from S, Si or Zn absorption lines), are [Z/H]=-0.85, -0.91 and -1.62 for the three DLAs in which N V is detected, but much lower (between -1.6 and -2.3) for the five cases with an N V upper limit (Fox et al. 2007). Thus, the non-detections are likely due to a lack of metals. In two of the three DLAs with N V and O VI detections, the [N/O] ratio could also be measured directly from N I lines, resulting in [N/O]=-1.2 and -1.1 (Fox et al. 2009). This follows the general trend that nitrogen is underabundant in DLAs (e.g. Petitjean et al. 2008). Thus, the finding that the N V/O VI ratios in DLAs are lower than in the Galactic Thick Disk
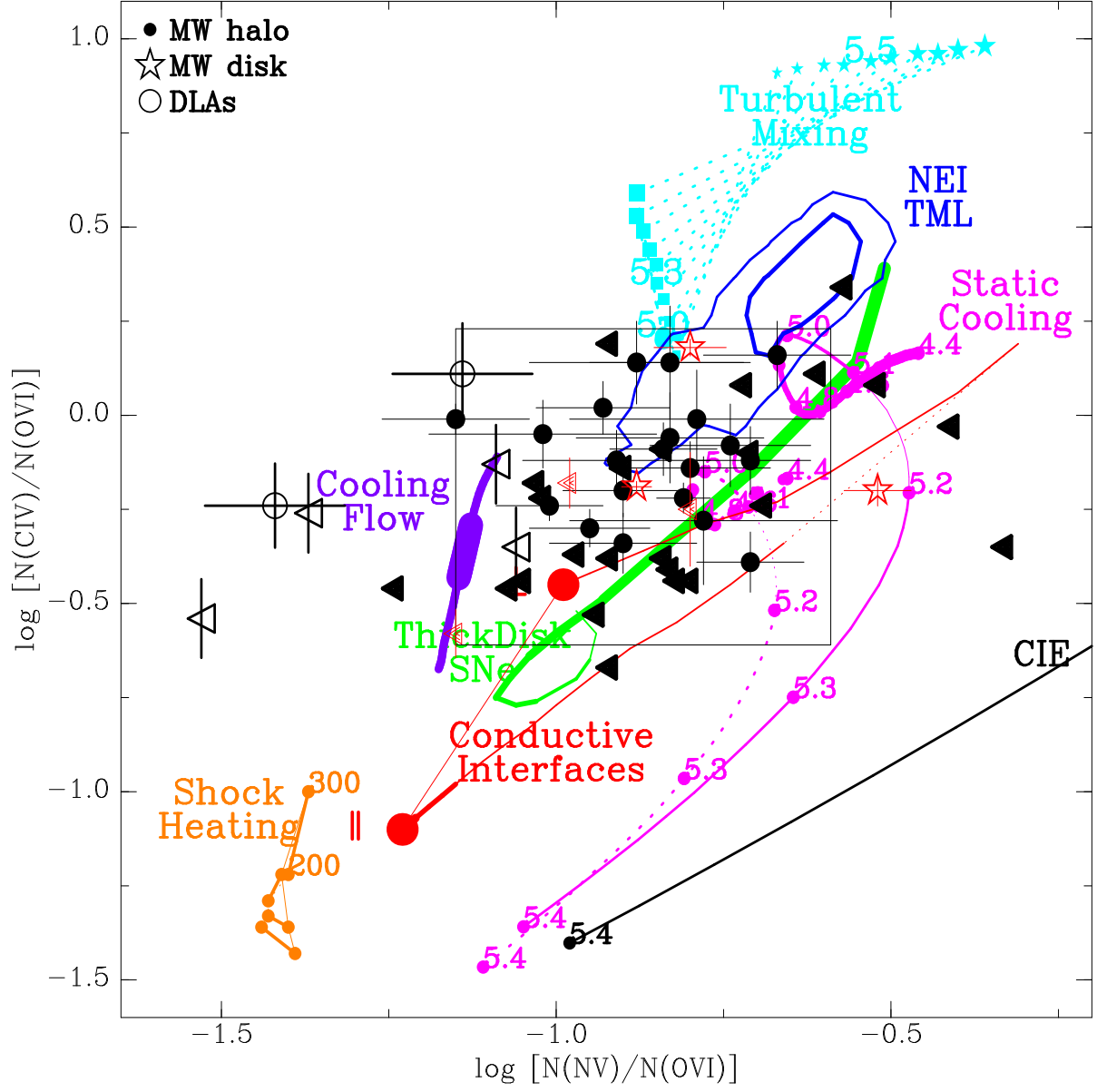
Fig. 11b.— See caption for Fig. 11a
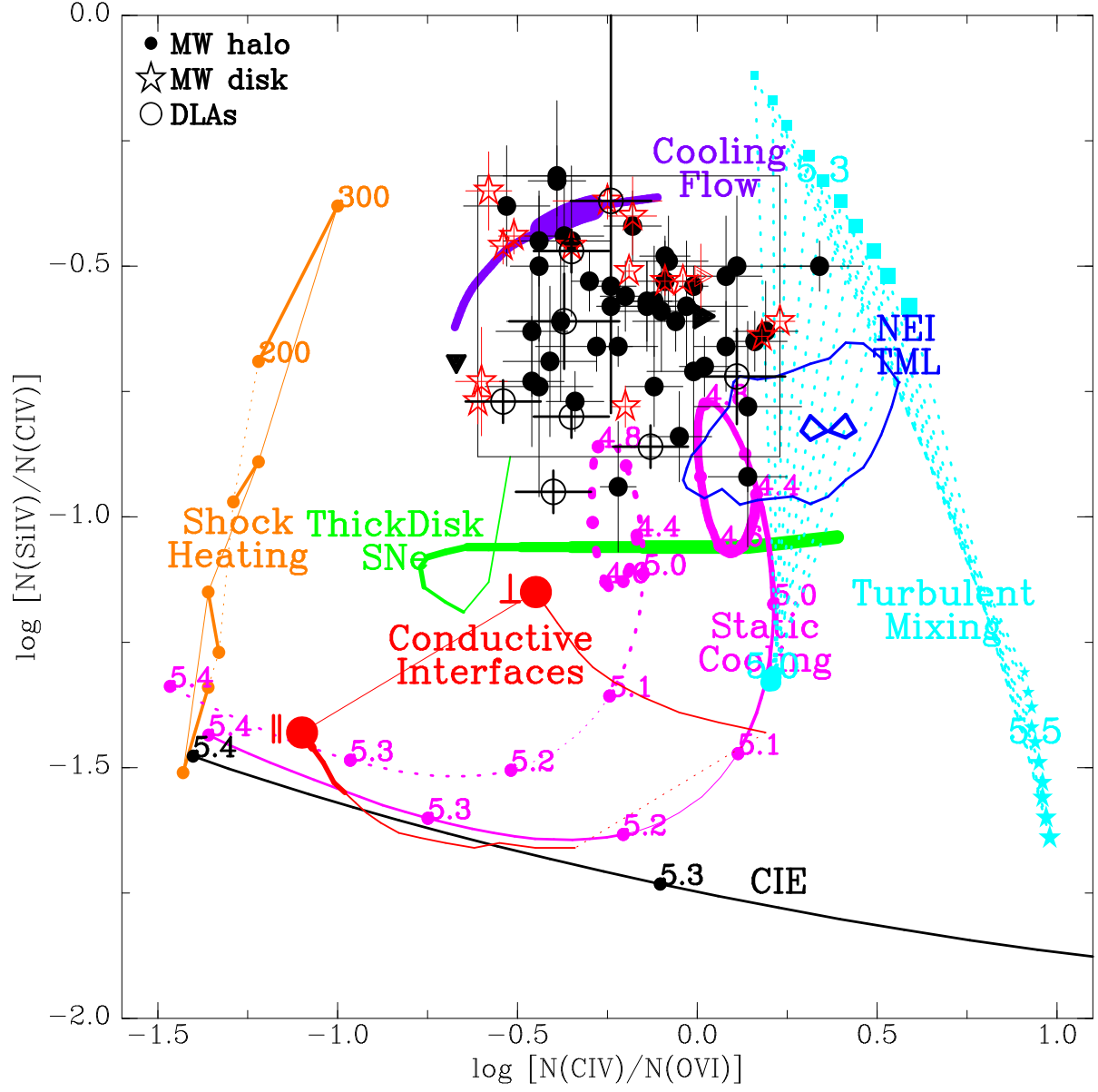
Fig. 11c.— See caption for Fig. 11a
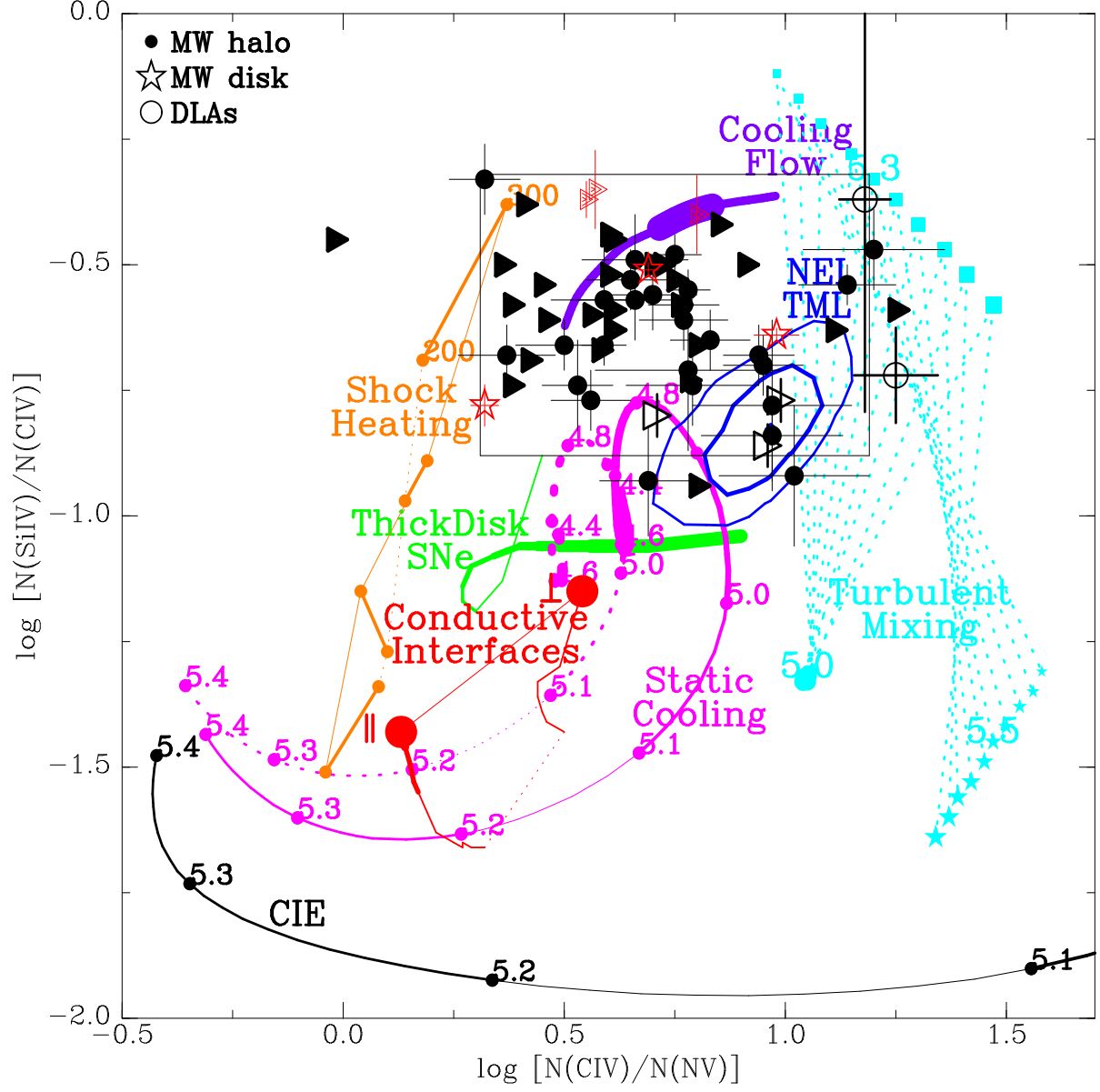
Fig. 11d.— See caption for Fig. 11a

can be explained as a differential abundance effect for nitrogen, and is not indicative of any difference in physical conditions.

We note that in nearby dwarf galaxies with metallicity [Z/H]<−1 times solar, the N/O ratio is about 0.8 dex below its value in the Sun (and in the Milky Way) (Skillman 1998). This effect can be explained as the result of a difference in the relative amount of N produced by Type II supernovae (primary N), as compared to N formed in intermediate-mass stars (secondary N). If the gas sampled by the z=2–3 systems was blown out from galaxies at early times, all N would be primary, and the N/O ratio would be subsolar, which can explain the relatively low N V/O VI ratios.

Independent of the cause, however, it is clear that N V/O VI in the high-redshift DLAs differs from that in the Milky Way. Thus, adapted numerical models are necessary, requiring subsolar N/O. However, since most of the cooling occurs through the ions of O and C, it is likely that the effects of using subsolar N/O are minimal and that the predicted N V column densities would scale linearly with N/O.

5.2.   Collisional Ionization Equilibrium (CIE)

The simplest calculation involves assuming a cloud that has fixed temperature and density, in which every collisional ionization is balanced by a recombination. Sutherland & Dopita (1993) provided a table for the resulting ion fractions, as did Gnat & Sternberg (2007). The predictions in the latter paper are about 0.3–0.4 dex higher for N V, C IV and Si IV at temperatures around $\log T$=5.3, which is caused by changes in atomic parameters (see references in Gnat & Sternberg 2007). The Si IV fraction differs even more above $\log T$=5.4. On the other hand, the predicted O VI fraction is rather similar, except above $\log T$=6.0, where the Gnat & Sternberg (2007) model predicts less O VI. All this results in predictions for the line ratios that can differ by as much as 0.4 dex from the Sutherland & Dopita (1993) values.

However, we do not expect the gas to be in CIE (and it is not observed to be). First of all, O VI will only exist at temperatures above about 10^5 K, but then the Si IV/C IV ratio is $<<−1.5$, i.e. much smaller than what is observed. Moreover, if we apply the CIE ionization fractions to a cloud with $\log N(\mathrm{H})$=19, then $\log N(\mathrm{O\ VI})$ can only be ∼14.1 for temperatures above $\log T$=5.3, while $\log N(\mathrm{C\ IV})$ is ∼13.8 for temperatures near $\log T$∼4.8 and $\log T$∼5.2. $\log N(\mathrm{Si\ IV})$ only reaches the observed value of 13.2 if $\log T$<5.0. I.e., for temperatures at which the CIE model predicts the presence of O VI, there is no C IV and no Si IV, while at lower temperatures a sufficient amount of $N(\mathrm{C\ IV})$ and $N(\mathrm{Si\ IV})$ is only

present in the absence of O VI.

5.3. Static non-equilibrium ionization radiative cooling

Edgar & Chevalier (1986) were the first to predict the ionization properties of gas starting at high temperature (10^6 K) and cooling down radiatively. In such models, the gas starts out in CIE at a high temperature (5×10^6 K in their case), and then is allowed to cool, either isochorically (at constant density) or isobarically (at constant pressure). In these models there are no external sources of heat or photoionization, the gas is not flowing, and it is assumed that the column density is low enough that the gas is optically thin. As most of the cooling is provided by metal-line emission, the metallicity of the gas will determine the timescale of the cooling. At high metallicity, the gas can cool, but highly-ionized atoms will recombine too slowly, leading to an overabundance of ions such as C IV, N V and O VI compared to gas in CIE at the same temperature. That is, the ionization is frozen in for a while. The higher the metallicity, the faster the cooling and the larger the discrepancy.

The Edgar & Chevalier (1986) paper gave predictions for both isochoric and isobaric cooling. For the isobaric case the values of Si IV/C IV, C IV/O VI and C IV/N V are 0.5–1.0 dex below the observed values, while in the isochoric case these ratios are underpredicted by 0.2–0.4 dex. Although this does not match the observations, the model was influential since it showed that it is possible to get column densities and ionic ratios that are very different from those in CIE.

Gnat & Sternberg (2007) presented a more detailed set of predicted ionization fractions for a variety of static non-equilibrium models. They provided tables for 10 cases: isochoric and isobaric cooling at metallicities $Z=0.001$, 0.01, 0.1, 1 and 2 times solar. For metallicities $Z<0.5$ solar, the difference with CIE predictions is minimal. Similarly, the difference between the isochoric and isobaric cases is one of degree. In particular, for $Z=0.1$, the isobaric and isochoric predictions differs by less than 0.1 dex, while the $Z=2$ isobaric case is almost identical to the $Z=1$ isochoric case.

Gnat & Sternberg (2007) also discussed when it would be appropriate to use the isobaric or the isochoric case. They took a spherical cloud which starts out cooling isobarically, and thus contracting as the temperature decreases. This increases the column density. If it becomes larger than $N_{tr}=1.2\times10^{19}\left(\frac{T}{10^5}\right)^{2.04}$ K the cooling become isochoric. With the ionization fractions predicted by the isobaric cooling model, we can derive the implied total hydrogen column density for an O VI column density of $\log N(\text{O VI})=14.1$. This value is below N_{tr} for temperatures $\log T>5.3$, implying that at lower temperatures the appropriate

cooling model to use is the isochoric one.

To assess whether a non-equilibrium ionization radiative cooling model is realistic, one should not only look at ionic ratios, but also take into account the predicted total ionic column densities, the cooling time and the integrity of a cloud as it cools and moves. The column densities are within 0.2 dex of the observed averages for temperatures between $\log T$=4.3 and 5.1, if the cloud has solar metallicity or higher and total hydrogen column density $\log N(\mathrm{H})$∼19. For Z=0.1, however, the cooling is so slow that recombination can keep up and the column densities of O VI, N V and C IV only barely match the observations at $\log T$=5.2, long before any Si IV is formed. The cooling time to go from T=3×10^5 K to 10^4 K is about t=3×$10^4/n_0$ (cm^{-3}) yr for a solar metallicity cloud (where n_0 is the density of H$^+$; Gnat, private communication). Given $\log N(\mathrm{H})$∼19 and a scaleheight of 3 kpc, the H$^+$ density at 1 kpc is about 7×10^{-4} cm^{-3}, implying a cooling time of 40 Myr. If the gas were moving at a rate of 10 km s^{-1}, it would move over 0.4 kpc during that time, which is likely significant relative to its size, but not so large that the cloud would completely disperse. Thus, we conclude that it is possible to construct a realistic situation in which the non-equilibrium ionization radiative cooling model might be applicable.

In Figure 11, the magenta lines show the isochoric non-equilibrium radiative cooling model for the temperature range of $\log T$=5.4 to 4.4. The solid curve is for solar metallicity, the dotted curve for two times solar metallicity. Clearly, this model can match some of the observed ratios, specifically C IV/N V and C IV/O VI. However, it underpredicts Si IV/C IV and overpredicts N V/O VI. In Figure 11d the pattern of datapoints suggestively lies on a curve with the same shape as the solar-metallicity curve, but with higher Si IV/C IV ratio. Thus, given the many simplifying assumptions, the predictions of this model are close enough to the observed values that we conclude that non-equilibrium radiative cooling is likely to be an important part of the processes that produce the highly-ionized atoms.

5.4. Radiatively cooling gas flows

The model described in the previous subsection does not take into account the gas dynamics. Doing so substantially changes the predictions for the relative ionic column densities, even with the same prescription for non-equilibrium cooling. Shapiro & Benjamin (1991, 1993) and Benjamin & Shapiro (unpublished) studied this in more detail. Their model follows the thermal and ionization state of gas in a one-dimensional planar, steady-state flow, including the effects of radiative transfer of photons generated by the hot phase of the gas. This results in a substantial boost for the column densities of CIV and especially Si IV. Since this model has not been fully described in detail in the literature, we present a

summary in an appendix. We note that the physical origin of the flow remains unspecified in this model – it is a description of the physical structure that results after a cooling front develops in a flow, be it an outflowing wind of hot gas, or an inflow.

Here we compare the predictions of the cooling flow model to the observations. This shows that the predicted column densities of all four ions (O VI, N V, C IV, Si IV) are within 1 or 2 times the observed spread from their average value (see Section 4.5 and Figure 6) for flow velocities between 20–30 and 12–42 $\mathrm{km\,s^{-1}}$, respectively. The resulting predictions for the ionic ratios are shown by the thick magenta line in Fig. 11. This reveals that this model correctly predicts the observed range of the C IV/O VI, C IV/N V and Si IV/C IV ratios. However, in general the model predicts slightly too high values for $N(\mathrm{O\ VI})$ and slightly too low values for $N(\mathrm{N\ V})$ (see appendix), leading to slightly lower N V/O VI ratios than observed (by $\sim$0.4 dex). This is true both for the average value and for most of the column densities seen in individual components where all four ions are detected. Unlike what is the case for all other models, this model predicts good values for *both* the observed column densities *and* the observed column density ratios, suggesting that a cooling flow model including self-photoionization represents the physical conditions in the Galactic lower halo fairly well. It is likely that only relatively minor adaptations may be needed to make the predictions for O VI and N V fit the observations even better.

5.5. Shock Ionization

Shock fronts passing through the gas can create transition temperature gas. A grid of low-density shock models was presented by Dopita & Sutherland (1996), for shock velocities of 200, 300, 400 and 500 $\mathrm{km\,s^{-1}}$, magnetic parameter $B\,n^{-3/2} = 0$, 1, 2 and 4 $\mu\mathrm{G\,cm^{-3/2}}$, and solar abundances. In the Milky Way corona, shock velocities of 400 $\mathrm{km\,s^{-1}}$ are not expected, so we compare data and model only for 200 and 300 $\mathrm{km\,s^{-1}}$ shocks. In these models the ionization of the ions is determined taking into account non-equilibrium conditions. In these models the logarithm of the O VI column density is predicted to be 14.32–14.35, while $\log N(\mathrm{N\ V})$ spans the range 12.85–12.95. The predictions for $\log N(\mathrm{C\ IV})$ and $\log N(\mathrm{Si\ IV})$ are much more varied, ranging from 12.8–13.0 and 11.3–12.8, respectively, with higher column densities occurring for higher shock velocities and stronger magnetic fields. Thus, shock models predict O VI and N V column densities that are a factor 1.8 and 2.4 larger than the observed average, while the column densities of C IV and Si IV are underpredicted by an order of magnitude. Thus, in the ratio-ratio plots shown in Figure 11, the predictions for the shock models (shown as orange lines) lie far away from the observed values. Therefore, shocks appear to be unlikely explanation for the observed highly-ionized atoms in the Galactic

corona.

5.6. Conductive Interfaces

If a reservoir of hot gas comes into contact with a cool cloud, electron collisions may conduct heat between the two media, and transition temperature ions can be produced in the conduction front as the cooler gas evaporates and the hotter gas condenses. This process was modeled by Borkowski et al. (1990) and Gnat et al. (2009). In the first of these two papers predicted column densities are shown for several ions as function of time and as function of the angle between the magnetic field and the conduction front. The magnetic field is important because the thermal conductivity of the plasma is far greater along the magnetic field lines than across them.

In the Borkowski et al. (1990) model the C IV column density stabilizes at more or less constant values (less than 0.3 dex variation) after about 10^4 yr. This is the case for N V after 10^5 yr and for O VI after about 2×10^5 yr. At earlier times the evolution in the column densities (and thus the ionic ratios) is rapid. Thus, in a ratio-ratio plot, the range of ratios that this model can accommodate varies with the age of the youngest interface that is included. Fox et al. (2004, 2005) chose 10^5 yr as the age of their youngest interface. However, between 10^5 and 2×10^5 yr the O VI column density has not yet stabilized, and N(O VI) increases by 0.27 dex. On the other hand, N(N V) and N(Si IV) are constant and N(C IV) decreases by 0.07 dex. Thus, the C IV/O VI ratio decreases by 0.34 dex as the interface ages from 10^5 to 2×10^5 yr. It should be noted that these interfaces mature relatively quickly. The ratios traverse the track in a few 10^5 yr, but then they stay constant for the next several 10^6 yr. Thus, for over 90% of the lifetime of the interface this model predicts a unique value of the ionic ratios.

Gnat et al. (2010) recently revisited the conductive interface model, exploring a greater range in the parameter space characterizing the interface. They present column densities for mature interfaces in which the surrounding medium has a temperature between 10^6 and 10^7 K, and in which the pressure ranges from 0.1 to 50 K cm^{-3}. They further include photoionization by the extragalactic radiation field, though not magnetic fields. However, unlike Borkowski et al. (1990) they do not tabulate the time evolution of the column densities. Comparing their predicted ionic ratios to those of Borkowski et al. (1990), we find that if the pressure P/k is >5 K cm^{-3}, all of the predicted ratios cluster within 0.2 dex of those found by Borkowski et al. (1990) models for the case of a perpendicular magnetic field. Thus, expanding the parameter space does not substantially change the nature of the predictions, and we therefore do not explicitly show the results of the Gnat et al. (2010) predictions in

Figure 11.

In Figure 11 we show with red lines the range of ratios for times $>2\times10^5$ yr, with one line for the case of a perpendicular magnetic field and one line for a parallel field. We connect the start and end points of these lines to form a box that encloses the full range of possible predictions. The line thickness increases with time. This shows that after about 1 to 2 Myr the ionic ratios stabilize at a fixed value. Thus, unless one considers a very young interface, this model predicts just a single set of ionic ratios. For the case of the perpendicular magnetic field, the predicted final ratio for N V/O VI and C IV/O VI lies toward the lower end of the observed values, while C IV/N V is close to the average. However, Si IV/C IV is underpredicted by about 0.5 dex, and all predictions for the case of a parallel magnetic field differ by about 0.5 dex from the observations. The fact that Gnat et al. (2010) added some photoionization to their models, but produce the same predictions for the line ratios implies that adding photoionization will not help to increase the relative amount of Si IV.

An additional problem with these models is that each interface produces a maximum column density of about $\log N$(O VI)=12.8, $\log N$(NV)=12.1, $\log N$(C IV)=12.5 and $\log N$(Si IV)=11.1). This is in the case with a magnetic field that is perpendicular to the conduction front, and for an initial temperature of the hot phase of 7.5×10^5 K. For a parallel field these values are 5–10 times smaller, but increasing the temperature of the hot phase to 10^6 K increases them by a factor ~2. Thus, the Borkowski et al. (1990) model can be used to predict the column density *ratios*, but it cannot explain the observed total column densities. That requires assuming that a sightline intersects many interfaces. Assuming an average angle of 45° between the magnetic field and the interface (reducing the average column density by a factor 2), but also assuming that 10^6 K is more typical for the hot gas than 7.5×10^5 K (increasing the average column density by a factor 2), between five to fifty interfaces would be required to build up the observed total column densities. As each interface has a thickness on the order of 10 pc, the interfaces would have to occupy a total pathlength on the order of 100 pc, which is easily accommodated within the several kpc scaleheight of the highly-ionized atoms.

To summarize: (1) the conductive interface model strongly underpredicts N(Si IV); (2) the time spent as a mature interface with constant ionic ratios is a factor 10 longer than the time spent along the tracks, (3) for a mature interface the predicted N V/OVI and C IV/O VI ratios are relatively low, and (4) it is difficult to build up the total column densities that are seen, with each interface only contributing a small fraction of the total. We thus conclude that conductive interface physics is not the most important process producing the highly-ionized atoms in the Galactic corona. We note that this conclusion is consistent with the Bowen et al. (2008) result that the O VI— absorbers in the disk exhibit a broad range of column densities, with the more strongly absorbing clouds having a lower space density than

the weakly absorbing clouds. The latter conclusion follows from the fact that while N(O VI) correlates with distance, the dispersion in N(O VI) does not decrease as the detected clouds get more distant.

5.7. Thick Disk supernovae

Another model that we consider here is that of Shelton (1998), who analyzed the effect that old type Ia supernova remnants above the Galactic plane might have on the state of the Thick Disk gas. She predicted the time-evolution of the column densities of O VI, N V and C IV (though not of Si IV) inside a supernova bubble for an explosion with energy 0.5×10^{51} erg expanding into a medium with ambient density $0.01 \, \text{cm}^{-3}$ and ambient non-thermal pressure $1800 \, \text{K} \, \text{cm}^{-3}$. We were separately provided the predictions for the Si IV ion, so that we could properly compare this model to the observations.

In this model, the O VI column density decreases from an early value of $\log N$(O VI)$=14.2$ at 0.1 Myr to about 13.6 at 0.5 Myr, then slowly rises to 13.7 at 10 Myr, falls to 13.2 at 15 Myr and then it disappears. The other ions behave similarly, plateauing at $\sim$12.8, 13.2, and 12.0 dex for N V, C IV and Si IV, respectively. N V/O VI is about -1.0 up to an age of 10^7 yr, then decreases to -0.5 dex at 1.5×10^7 yr. On the other hand, in the early stages, Si IV/C IV first dips from ~ -1.5 to ~ -0.7 dex, then reaches a value of ~ -1.1 dex after 2×10^6 yr, where it remains throughout.

As can be seen from the green line Figure 11b, this model predicts values for N V/O VI that span the range of observed values. However, if the supernovae have random ages, there should be more ratios near -1.1 (ages $<$10 Myr) than at higher values (ratio slowly increasing until an age of 16 Myr). Further, this model underpredicts Si IV/C IV by about 0.5 dex and the absolute values of the column densities during the plateau phase are about 0.4, 0.5, 0.6 and 1.2 dex too low for O VI, N V, C IV and Si IV, respectively. The latter problem can be accommodated if between 2 and 3 remnants are intersected in each sightline. Since Shelton (1998) derives that the sky coverage fraction due to Thick Disk supernovae is 30–60%, this implies that the predicted column density is a factor $\sim$3 to 5 too low to account for the observed column densities.

In summary, this model predicts the correct range of N V/O VI ratios, but the Si IV/C IV ratio is underpredicted by a 0.5 dex and it predicts a lopsided distribution of N V/O VI ratios. Further, the implied supernovae rate is a factor 3–5 too high, Thus, halo supernovae may contribute to the observed quantities of highly-ionized atoms, but they cannot be the whole story.

5.8.   Turbulent Mixing Layers

Conductive heat transfer is not the only process that can take place at the interface between hot and cold gas. Relative sideways motions can cause Kelvin-Helmholtz instabilities that mix the two, creating gas at transition temperatures. This model was proposed by Begelman & Fabian (1990), and developed by Slavin et al. (1993), Esquivel et al. (2006) and Kwak & Shelton (2010). These papers present predictions for ionic column densities.

Slavin et al. (1993) presented predictions for entrainment velocities between 25 and 100 km s^{-1}, at temperatures of $\log T$= 5.0, 5.3 and 5.5, and for two abundance cases – solar abundances and gas in which half of the C, N, and O (and 90% of the Si) are on dust grains, for a total of 12 different predictions. In these models the mechanical aspects of the mixing were treated analytically (based on a simplified picture of how the mixing occurs), while the ionic column densities were then predicted using non-equilibrium ionization balance calculations including self-photoionization. We show the solar-abundance results of Slavin et al. (1993) in Figure 11 (light blue points and lines). Since they showed that the change of ionic ratios with entrainment velocity is almost linear, for a given temperature we interpolate the ratios at 25 and 100 km s^{-1} to form a series of points in the ratio-ratio diagram, increasing in size with entrainment velocity. Points with $\log T$=5.0 are shown by closed circles, points at $\log T$=5.3 by closed squares and points at $\log T$=5.5 by closed stars. High Si IV/C IV occurs at $\log T$=5.3, while high N V/O VI occurs at $\log T$=5.5. We then use dotted lines to connect the values for the three different temperatures at the same entrainment velocity. This defines a region in the ratio-ratio diagnostic plot for the predictions of the Slavin et al. (1993) turbulent-mixing model. Changing the abundance pattern (i.e. assuming differential depletion onto dust) shifts these points somewhat, but by less than 0.2 dex for O VI, N V and C IV, although Si IV is strongly decreased.

In the Slavin et al. (1993) model, the O VI column density in each interface was only about 10^{11}–10^{12} cm^{-2}, implying the need for more than 100 interfaces to build up the total observed column density of 10^{13}–10^{14} cm^{-2}. de Avillez & Breitschwerdt (2005) show that this may indeed be possible. They took a hydrodynamical model of the ISM and calculated the density of O VI as implied by radiative cooling (assuming local CIE in each gridcell). The O VI originates in the interiors of regions created by supernovae, as well as the result of local cooling promoted by turbulent mixing. They found that on average each sightline out to 1 kpc contains many structures that contribute a few 10^{12} cm^{-2} of O VI, and that the total is about 10^{14} cm^{-2}. Although the assumption of local CIE is probably false (given that this predicts the wrong ionic ratios), this shows it could in principle be possible to build up the total observed O VI column density from many different small structures in the sightline.

The study by Esquivel et al. (2006) addressed the effects of magnetic fields, which mainly

result in a reduction of the spread in the predicted ratios for a given flow velocity and density choice. Since Esquivel et al. (2006) did not give a table of predictions, and since Figures 8 and 9 in Esquivel et al. (2006) show that their results are similar to those of Slavin et al. (1993), we do not include this model in Figure 11.

Kwak & Shelton (2010) revisited the turbulent mixing model, making a two-dimensional hydrodynamical calculation, while following the ionization using non-equilibrium physics (although they still used the CIE value for the cooling function at each temperature). Their base model ("A") uses a 100×300 pc box, with hot gas density and temperature $10^{-4}\,\mathrm{cm}^{-3}$ and 10^6 K and cool gas density and temperature $0.1\,\mathrm{cm}^{-3}$ and 10^3 K, and an entrainment velocity of 100 $\mathrm{km\,s}^{-1}$. In their paper, they show the time evolution of the column densities of O VI, N V and C IV, and tabulate the time and sightline averages for these three ions (which are $\log N$(O VI)=12.8, $\log N$(N V)=12.2, $\log N$(C IV)=13.1), as well as the ionic ratios. Although Kwak & Shelton (2010) did not publish their predictions for Si IV, they included it in their calculations, and we obtained the Si IV values from them.

For each time step, their model produces a two-dimensional map, with 256 directions along which a column density can be derived for each ion. We obtained each of these values, once every Myr for an 80 Myr period. Since it takes about 20 Myr for the effects of initial conditions to disappear, we used the results between 20 and 80 Myr to create a contour plot showing how often a given ratio occurs. The resulting contours are shown in blue in Figure 11. Clearly, this model gets the ratios almost correct, with on average N V/O VI about 0.3 dex too high (observed average −0.87, model average −0.56), C IV/O VI about 0.6 dex too high (−0.21 observed average, 0.39 predicted average), C IV/N V about 0.2 dex too high (0.75 vs 0.94) and Si IV/C IV about 0.2 dex too low (−0.60 vs −0.83). Some of these differences are similar to the mismatches for other models, but for the TML model none of the differences is larger than 0.6 dex, unlike what is the case for any other model. The curve showing the evolution of the ratios during static non-equilibrium cooling crosses the turbulent mixing contours, suggesting that in the turbulent mixing model the cooling is not highly affected by the motions of the gas. In this model, the O VI column density through each ∼100 pc thick layer is about $\log N$(O VI)=12.8, so that about 10–20 layers are needed to make up the observed total. These would take up about 1 kpc of the sightlines, which is a substantial, but possible, percentage for gas with a scaleheight of 3 kpc.

We also compared the predictions of the Kwak & Shelton (2010) model A to those of their models D and F. They already showed that their results are not very sensitive to the parameters (spatial resolution, grid size, entrainment velocity, initial perturbation amplitude, temperature of the hot gas), but that there are some differences. To be precise, Model D (entrainment velocity 50 $\mathrm{km\,s}^{-1}$ instead of 100 $\mathrm{km\,s}^{-1}$) results in relatively more Si IV and

C IV, improving the correspondence with the observed values for Si IV/C IV, but it makes the predictions for C IV/O VI and C IV/N V slightly worse. The same effect, but stronger, happens in Model F (temperature of the hot gas 3×10^6 K instead of 10^6 K). Their Model A appears to give the best fit. We conclude that turbulent mixing layers may play an important role in explaining the highly-ionized ions in the Galactic Corona.

6.   Discussion

We showed in the Sect. 4.2 that the highly-ionized gas in the Galactic corona usually is seen at velocities 30 to 100 $\mathrm{km\,s^{-1}}$ more negative or more positive than can easily be explained by differential galactic rotation. In Sects. 4.3, 4.4, 4.5, and 4.6 we analyzed the widths of the absorption lines, the signature of Galactic rotation, the column densities and the relation between these quantities and location on the sky. We found that the widths (FWHM) of individual absorption lines range from $\sim$25 $\mathrm{km\,s^{-1}}$ to $\sim$120 $\mathrm{km\,s^{-1}}$. On average the widths of O VI and N V absorption lines are similar, as are those of C IV and Si IV, while the average of the latter is slightly, but significantly, narrower (42 $\mathrm{km\,s^{-1}}$ vs 60 $\mathrm{km\,s^{-1}}$). The line width is always much larger than the maximum contribution from thermal motions ($\sim$20 $\mathrm{km\,s^{-1}}$), so most of the linewidth must be non-thermal. Therefore, the four ions cannot be completely co-spatial. On the other hand, the widths of O VI/N V vs C IV/Si IV correlate very well. That is, in sightlines where O VI and N V are wide, C IV and Si IV are also wide. Furthermore, there appears to be no difference in the centroids of the absorption lines of these ions. Thus, although they do not originate in the same parcels of gas, they must originate in a single structure, in which non-thermal motions are larger in the region where the hotter gas occurs.

There appears to be no relation between galactic latitude and the extent of the absorption, which implies that the velocities of individual gas parcels in the sightline are randomly oriented. If, for instance, the velocities were mostly vertical, projection effects would lead to a relation between the extent of the absorption and latitude, with wider lines at higher latitude. The large spread of velocities in each direction make the effect of galactic rotation difficult to discern, but we can show that it is responsible for shifting the centroids of the profiles by up to 30 $\mathrm{km\,s^{-1}}$ from zero. We looked for evidence of a vertical gradient in the rotation velocity, by comparing the expected centroids to the observed values. Taking into account that the observed scaleheight of the gas is about 3 kpc, we find that a co-rotating corona best explains the centroids. We further find that although the distribution of the highly-ionized gas is by no means uniform, the variations across the sky are less than an order of magnitude, with no directions toward which these ions are not seen. Much of the

variation can be explained as a latitude effect, with a larger pathlength through the layer at low latitudes. However, over most of outer galaxy below the Galactic plane there is a slight (0.2 dex, factor 1.6) deficit in N(O VI), while in the inner Galaxy and over the Galactic North Pole there is a slight excess (0.2–0.4 dex, factor $\sim$2) in the column density of all ions. A description in terms of a plane-parallel layer in which the column density changes as $N \sin|b|$ works fairly well. The dispersion around $N \sin|b|$ is then only about 0.15–0.20 dex (a factor $\sim$1.5). Thus, the highly-ionized atoms appear to occur in a somewhat irregular thick layer with scaleheight 3 kpc, which rotates along with the Milky Way, and in which gas parcels have random velocities that are on the order of $\pm$60 km s^{-1}.

For a given absorption component and ion, the distribution of column densities is relatively narrow. The range in column densities is no more than a factor 10, with a dispersion of a factor of about 2, i.e. for 70% of the sightlines the observed ionic column density falls within a factor 2 of the average. This is compatible with a situation in which the transition temperature gas originates in just a few (3–5) individual structures in each sightline, in each of which the column density is on the order of 1/3–1/2 the average observed value. The distribution of column density ratios is even narrower, with the ratios N V/O VI and Si IV/C IV having a dispersion of only 0.14 dex (a factor 1.3 either way). This suggests that in each individual structure the same process is responsible for producing the transition temperature gas everywhere. The fact that the distribution of the C IV/O VI and C IV/N V ratios is slightly wider 0.23 dex (a factor 1.7) again indicates that although these ions all come from a single structure, the ions that should occur at somewhat higher temperature are not fully co-spatial with the ions that are more prevalent at lower temperatures.

From the ratio-ratio plots shown in Figure 11, we conclude that the physical process(es) that generate the highly-ionized gas in the Milky Way's corona must include non-equilibrium ionization and involve radiative cooling. In fact, the gas must be very far from collisional ionization equilibrium, since in CIE O VI cannot coexist with Si IV, and there is no single temperature that simultaneously explains the observed N V/O VI and C IV/N V ratios. Further, for temperatures near 10^5 K all ionic ratios differ by at least a factor 10 from the observed values. Predictions based on shock heating strongly overpredict the amount of O VI relative to N V and C IV, and even the amount of N V relative to C IV. A model in which the transfer of heat occurs purely through electron conduction strongly underpredicts the Si IV/C IV ratio (by a factor 5–10, and underpredicts N V/O VI and C IV/O VI, although it gets N V/O VI correct, but only when the magnetic field is perpendicular to the interface. For a non-perpendicular magnetic field the predictions of the conductive interface model are rather different from the observations. This model *does* seem to work reasonably well if one only considers the N V/O VI vs C IV/O VI ratio-ratio plot. However, compared to the square box used by Fox et al. (2004, 2005), a more detailed look at the actual predictions

shows that they fall in a strip parallel to but below the observations (see Figure 11b).

We explored four different models that include non-equilibrium radiative cooling, including static cooling, the flow of gas through a cooling front, Thick Disk supernovae and turbulent mixing. The original turbulent mixing model of Slavin et al. (1993) predicts much larger ranges for the ratios than is observed, as well as a factor 1–2 more O VI than the newer numerical simulations of Kwak & Shelton (2010). Except for the static case, in these models the O VI, N V, C IV and Si IV do not coexist in the same gas parcels, but they are present in a related way in different parts of the same structure, as is indeed indicated by the observations. Since the predicted column densities are based on an integral through these structures, the predictions account for this effect.

The Thick Disk supernovae model underpredicts Si IV/C IV by about 0.5 dex, and predicts a distribution of ratios for N V/O VI and C IV/O VI that is much more strongly weighted toward lower values than what is observed. For the remaining three models, the predicted range of ratios differs by up to about 0.3 dex from the observations, with static radiative cooling and turbulent mixing predicting a value for N V/O VI N V/C IV that is too high by about 0.25 dex and C IV/O VI too high by 0.5 dex. At the same time, Si IV/C IV is too low by about 0.2 dex. That is, for a given amount of O VI, these models (on average) predict a factor 1.8 too much N V, a factor 3 too much C IV and a factor 1.7 too much Si IV. The cooling flow model (with self-photoionization included) predicts the correct range of ratios for C IV/O VI and for Si IV/C IV, but it underpredicts the amount of O VI relative to C IV and N V. Thus, none of the non-equilibrium ionization radiative cooling models can quite get all four ions correct at the same time. However, compared to models having equilibrium ionization and no radiative cooling, the former do a much better job.

7. Summary

We have analyzed the absorption from highly-ionized atoms through the complete Milky Way Thick Disk and halo as seen in 58 sightlines toward extragalactic targets. These ions are O VI, N V, C IV and Si IV and they sample gas at temperatures near 10^5 K, which originates where gas near 10^6 K cools or interacts with 10^4 K gas. For each sightline we determined over which range of velocities the absorption is likely to be associated with the lower Milky Way corona. We then measured the centroid velocity, linewidth, and column density for each ion. In many sightlines multiple components can be distinguished, which were separately measured. From these measurements we find that:

(1) The centroid velocities of O VI, N V, C IV and Si IV are very well aligned, with a

dispersion in the differences of $<8 \ \mathrm{km\,s^{-1}}$.

(2) The highly-ionized absorption extends to velocities between 30 and 80 $\mathrm{km\,s^{-1}}$ more negative or more positive than the range that can easily be explained by differential galactic rotation. For sightlines in the region near the Galactic north pole there is an excess of absorption at velocities more negative than $-60 \ \mathrm{km\,s^{-1}}$. This excess does not correlate with the intermediate-velocity clouds seen in H I 21-cm emission.

(3) We determined linewidths by calculating the second moment of the apparent column density profiles, converting to the full width at half maximum (FWHM). The resulting widths of the O VI and N V lines are on average 60 $\mathrm{km\,s^{-1}}$ and correlate very well (correlation coefficient ρ=0.97). The average widths of C IV and Si IV are 42 $\mathrm{km\,s^{-1}}$ (and ρ=0.94). The other correlations (e.g. between the widths of O VI and C IV) are slightly less strong (ρ~0.92). The difference between the widths of O VI/N V and C IV/Si IV is shown to be significant. Since the thermal width of these lines is only ~15 $\mathrm{km\,s^{-1}}$ for gas at a temperature of 10^5 K, most of the width must be non-thermal.

(4) We find that differential galactic rotation leaves its imprint on the velocities of the absorption lines. We predict the locations of the centroids from a simple model in which the gas co-rotates as one goes up above the disk, and in which the density falls off exponentially with a scaleheight of 3 kpc. Comparing these predictions to the observed centroids we can see the effect of galactic rotation, and we find that the average difference between the data and the prediction from the simple model is $5\pm16 \ \mathrm{km\,s^{-1}}$.

(5) The distributions of the integrated column densities of the highly-ionized atoms is relatively narrow, with average and dispersion 14.31 ± 0.20 (O VI), 13.48 ± 0.23 (N V), 14.17 ± 0.21 (C IV) ad 13.57 ± 0.18 (Si IV). For individual components these values are 14.06 ± 0.27 (O VI), 13.30 ± 0.30 (N V), 13.83 ± 0.34 (C IV) and 13.24 ± 0.35 (Si IV). Note that in the case of N V upper limits were omitted for this calculation.

(6) Over much of the sky the column densities generally increase with decreasing galactic latitude, but with a dispersion of about 0.17 dex (a factor 1.5) around the average. The equivalent polar column densities are 14.15, 13.19, 13.89 and 13.32 for O VI, N V, C IV and Si IV, respectively.

(7) Assuming solar abundances and an ionization fraction of about 10% the polar column densities imply a total hydrogen column density associated with the transition temperature gas of about $10^{18.8} \ \mathrm{cm^{-2}}$.

(8) In sightlines near the Galactic Center and toward the Galactic north pole, the column densities of all ions are enhanced by about 0.3 dex. This suggests enhanced activity at small

galactocentric radii, and near the Galactic north pole. We find marginal evidence that this excess is associated with enhanced absorption at negative velocities.

(9) At intermediate latitudes in the southern sky, O VI is depressed by about 0.2 dex, but none of the other ions are, indicating a subtle difference in the physical conditions.

(10) Determining the ratios of the column densities of the different ions, we find that the distributions of N V/O VI and Si IV/C IV are rather narrow, with a dispersion of just 0.14 dex ($\pm40\%$), and a spread between the smallest and largest value of 0.6 dex (factor 4). The distributions of other ratios (such as C IV/O VI) give a larger spread of 0.23 dex ($\pm70\%$). Important average ratios and spreads are (using a linear scale) N V/OVI=0.14 ± 0.04, O VI/N V=7.80 ± 2.90, C IV/O VI=0.71 ± 0.36, O VI/C IV=1.83 ± 1.15, Si IV/C IV=0.26 ± 0.08, C IV/Si IV=4.19 ± 1.47

(11) We discuss a number of ionization mechanisms, going back to the original papers to extract the detailed predictions. The models we discuss include collisional ionization equilibrium (CIE, from Sutherland & Dopita 1993 and Gnat & Sternberg 2007), static non-equilibrium ionization radiative cooling (Gnat & Sternberg 2007), radiatively cooling gas flows (Shapiro & Benjamin 1991, but fully described for the first time in the appendix), shock ionization (Dopita & Sutherland 1996), conductive interfaces (Borkowski et al. 1990 and Gnat et al. 2010), Thick Disk supernovae (Shelton 1998) and turbulent mixing layers (Slavin et al. 1993 and Kwak & Shelton 2010). We compare the predictions of ionic ratios for each model with the data in four different ratio-ratio plots, which include N V/OVI, C IV/O VI or C IV/N V vs Si IV/C IV and N V/O VI vs C IV/O VI. These were chosen so that for future observations at least one diagram can be used if data are available for only three of the ions. The historically most-used N V/O VI vs C IV/O VI diagram is the least discriminative of the four.

(12) We find that single-phase CIE models fail to explain the observations.

(13) The model for static non-equilibrium ionization radiative cooling shows that if the gas cools below $T \sim 10^{4.9}$ K the predicted ionic ratios are close to the observed values, with Si IV/C IV underpredicted by about 0.3 dex and N V/O VI overpredicted by the same amount.

(14) In radiatively cooling gas flows, there is a range of flow velocities at which the amount of cooling gas is similar to the observed amount. The best match for all four ions simultaneously requires a flow velocity on the order of $25 \, \mathrm{km\,s^{-1}}$. This model predicts that the different ions originate in different parts of the flow, with the pairs N V/O VI and C IV/Si IV living more closely together with each other than they do with the other ions. The model correctly predicts the range of ratios for C IV/N V and Si IV/C IV, although it overpredicts O VI/N V.

(15) Shock ionization models predict far too much O VI relative to the amount of N V and C IV, as well as too much N V relative to C IV. I.e., the predicted ionization state of the gas is too high.

(16) Conductive interface models were favored by Sembach et al. (2003) and Fox et al. (2004, 2005) to explain the transition temperature ions seen in high-velocity clouds. However, Fox et al. (2004, 2005) used the full ranges for N V/O VI and C IV/O VI predicted by Borkowski et al. (1990) for interfaces older than 10^5 yr. Here, we instead follow the evolution of these ratios with time and find that the delineated region is really a strip that lies below the observations. Furthermore, it takes only 1–2 Myr for the ratios to stabilize at a fixed value, compared to an interface lifetime that is >10 Myr. The other three diagrams show that the model strongly underpredicts Si IV/C IV, while the stabilized values for N V/O VI and C IV/O VI also tend to be too low. Furthermore, the model predicts total column densities in a single layer of only $\sim 10^{12.5}$ for O VI, so that >50 interfaces are required in each sightline. In light of these considerations, we conclude that the absorption from highly-ionized atoms in the Galactic corona probably does not originate in conductive interfaces.

(17) The effects of Thick Disk supernovae on the ionization state of the tenuous Galactic coronal gas was explored by Shelton (1998). In this model, the N V/O VI and C IV/O VI ratios evolve slowly at first, but then increase almost linearly over 16 Myr to cover the observed range. Si IV/C IV on the other hand is basically constant over the lifetime of the remnant, but underpredicted by about 0.5 dex. The integrated ionic column densities for O VI, N V and C IV are only a factor 3–5 below the observed values. If a way could be found to increase $N(\mathrm{Si\ IV})$ (e.g. including photoionization), this model might fit the observations. However, the number of Thick Disk supernovae needed to produce the integrated column densities is a factor of a few larger than the number of supernovae observed.

(18) The original predictions for turbulent mixing layers by Slavin et al. (1993) cover a range in Si IV/C IV that is much larger than what is observed. The predictions for the other ionic ratios also do not match the data well. On the other hand, a more recent, numerical, model of turbulent mixing layers by Kwak & Shelton (2010) almost gets most of the ionic ratios correct, although it appears to overpredict the amount of the ions with higher ionization potential (O VI and N V).

(19) From the fact that the number of absorption components that can be identified in each sightline is between 1 and 3, combined with the comparisons between the data and predictions from different models, and taking into account the results of our analysis of velocities and column densities, we conclude that the transition temperature gas in the Milky Way corona originates in several (1 to 5) structures in each sightline. These are

more common closer to the plane, and have a scaleheight of $\sim$3 kpc. Each structure has a randomly-oriented velocity, with a dispersion between different structures of about $75\,\mathrm{km\,s^{-1}}$. In these structures radiative cooling takes place, fast enough for the ionization to be frozen in. Whether the structures originate in a cooling flow, or as the result of the mixing of cool and hot gas remains unclear.

(20) Comparing the observed ionic ratios in Thick Disk gas to those seen in Disk gas and high-velocity clouds, we find that all of these fall in the same regions in the ratio-ratio plots, suggesting a similar origin for the transition temperature gas. In high-redshift Damped Lyα Absorbers the O VI, C IV and Si IV ions also exist in the same proportions, but N V appears underabundant, which is consistent with the subsolar N/O ratios measured in these systems.

Appendix

A cooling flow model

In this appendix we describe a model to predict the column densities and emissivities of highly-ionized atoms. A summary of this model was presented by Shapiro & Benjamin (1991, 1993) and Benjamin & Shapiro (1993); the full model is described in Benjamin (1994). This is the model labeled "Cooling Flow" in Fig. 11.

The model starts from the realization that a common element of the models used to analyze the column densities of the highly-ionized atoms is that they originate in gas that is not thermally stable. As a result, these ions are necessarily associated with flows of heating or cooling material. Since the heating and cooling timescales of this gas can be shorter than the ionization or recombination timescales, it is necessary to account for non-equilibrium effects when calculating the ionization. Moreover, it is important to consider the effects of ionizing radiation, produced either externally or by the cooling gas itself; this can substantially change the colum denities for certain ions under the right circumstances.

Such models of a radiatively cooling flow can be considered a generalization of post-shock flow models. However, unlike the case of radiative shock models, the initial flow velocity and the initial gas temperature are not necessarily coupled. The parameters for a flow model are (1) the initial temperature, (2) the initial density, and (3) the flow's velocity, as well as (4) the density compression evolution. In addition, one must specify an elemental abundance set and a set of atomic data to calculate the non-equilibrium ionization and cooling of the gas. In the model calculations described below the abundances used were from Allen (1973); the atomic data were completely described in Benjamin (1994), but come principally from Raymond & Smith (1977), Raymond (1987, priv. comm.) Shull & van Steenberg (1985) and Romanik (1988). There would be a (small) correction associated with adjusting the results to the more recent Asplund et al. (2009) abundances, which changes C IV/O VI by 0.04 dex and Si IV/C IV by −0.08 dex. We include these two changes in all the results shown below. The absolute changes in the abundances are a bit larger (−0.13 dex for oxygen, −0.09 dex for carbon, −0.13 dex for nitrogen and +0.01 dex for silicon), but (as argued below), a change in the abundance of oxygen will not significantly affect the O VI column density. For the other elements it is only the change relative to the change in oxygen abundance that matters.

Cooling curve

The effects of the non-equilibrium ionization and cooling are encapsulated in the cooling curve. These are given in Fig. A1 for equilibrium, isobaric and isochoric cooling gas, along with the dominant coolants at different temperature ranges. The instantaneous cooling time
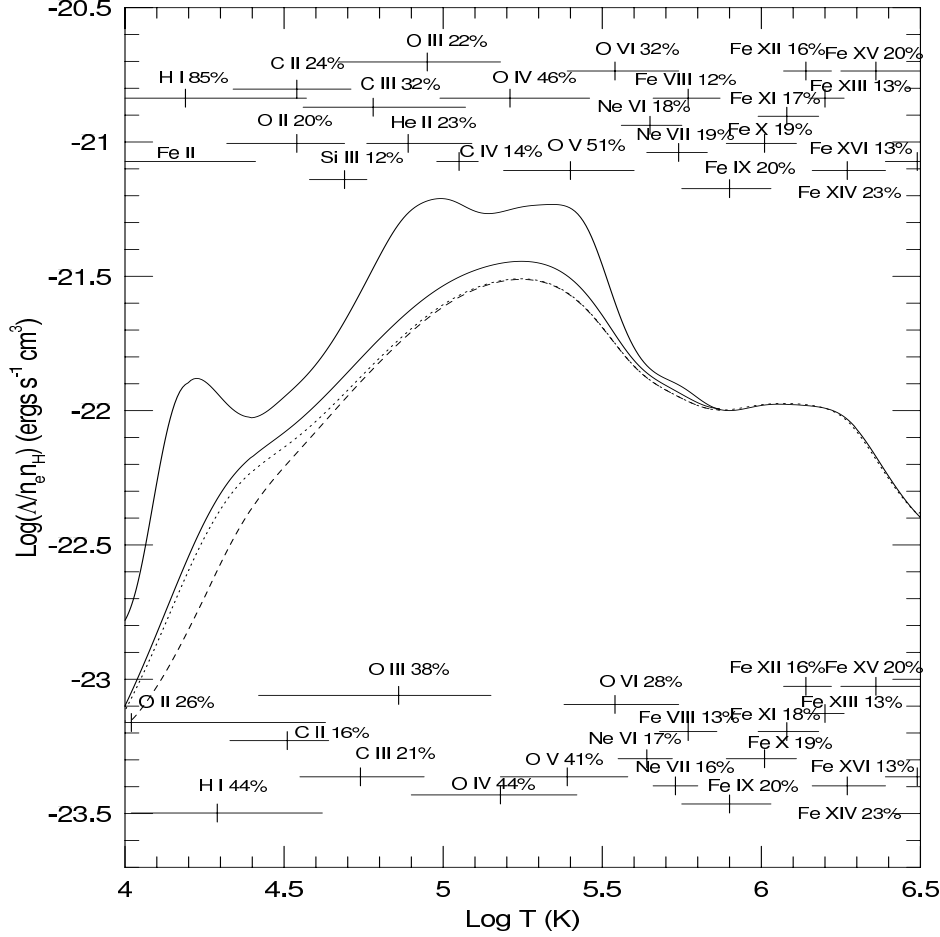
Fig. A1.— Radiative cooling rate of a solar metallicity gas ($\log[\Lambda/n_e \, n_H]$ $(\mathrm{erg\,cm^{-3}\,s^{-1}})$) versus $\log T (\mathrm{K})$. Three cases are shown: cooling in collisional equilibrium ionization (upper solid curve), isobarically with non-equilibrium ionization evolution (lower solid curve), and isochorically with non-equilibrium ionization evolution (dotted curve), in the absence of the effects of ionizing radiation. The dashed line shows the change in the isochoric cooling curve when the effects of radiation are accounted for assuming an initial flow velocity of $v_0 = 30$ km s^{-1}. These curves are very similar in shape and level to the ones used by others (see e.g. Sutherland and Dopita 1993 and Gnat & Sternberg 2007). The horizontal bars at the top of the graph indicate the temperature regime in which the labeled ion contributes more than 10% of the total cooling rate for gas cooling in ionization equilibrium. The temperature at which this ion makes its maximum fractional contribution to the cooling rate is denoted by a vertical tick mark and the percentage is noted. The lower bars show the same quantities but for non-equilibrium, isobarically cooling gas.

for a solar metallicity gas in ionization equilibrium with initial temperature $T_6=T/10^6$ K is $t_c=3\times10^7\ n_{-2}^{-1}\ T_6\ \mathcal{L}_{-23}^{-1}$ yr, where $n_{-2}=n_H/(10^{-2}\,\mathrm{cm}^{-3})$ and the normalized cooling rate is $\mathcal{L}_{-23} = \Lambda/(n_e n_H)/(10^{-23}\ \mathrm{erg\,cm}^{-3}\,\mathrm{s}^{-1})$. This complicated function can be approximated by functional forms that are good to within 50% (for the equilibrium case) or even 30% (for the isobaric and isochoric cases) by the following formulae:

$$\mathcal{L}_{-23}(T) = \left\{ \begin{array}{ll} 13.4\ T_6^{-0.74} & 10^5\,\mathrm{K} \lesssim T \lesssim 2\times10^7\,\mathrm{K}\ \text{(equilibrium)} \\ 36.3\exp\left[-3.4(\log_{10}(T)-5.23)^2\right] & 10^{4.4}\,\mathrm{K} \lesssim T \lesssim 10^6\,\mathrm{K}\ \text{(isobaric)} \\ 31.2\exp\left[-3.4(\log_{10}(T)-5.23)^2\right] & 10^{4.4}\,\mathrm{K} \lesssim T \lesssim 10^6\,\mathrm{K}\ \text{(isochoric)}\ , \end{array} \right\}$$

(1)

When the gas cools to a temperature $T\sim10^{4.4}$ K, the dominant source of cooling is collisional excitation of H Lyα, which is extremely sensitive to the ionization fraction of hydrogen, and thus depends sensitively upon the assumed value of the incident ionizing flux.

Structure of the flow

The initial conditions of the one-dimensional model are marked by a flow boundary. On one side of this boundary the gas has some high initial temperature T_0 ($>10^6$ K), and on the other side the gas has started to cool due to radiative losses. Hot material flows through the boundary, and moves away from it. This sets up a steady-state temperature and ionization-level gradient along the direction of the flow. The rate of mass (M) flowing through per unit area (A) equals $\dot{M}/A = \bar{m}n_{H,0}v_0$, where $\bar{m}$ is the mean mass per hydrogen atom (which depends on the metallicity), $n_{H,0}$ is the initial hydrogen particle density, and v_0 is the flow velocity. This velocity is defined in the (unique) reference frame where the particle flux remains constant.

As the gas cools, the loss of thermal energy reduces its pressure, and thus its density should increase. However, the actual pressure profile along the flow is also affected by the constant addition of new material, by geometrical constraints (e.g. expansion) and/or by magnetic fields. For simplicity, we only consider two bounding cases for the density evolution of the gas as it travels along the flow: isobaric (constant pressure) and isochoric (constant volume and thus constant density). In the isobaric case the temperature drops along the flow, but it is assumed that the volume increases proportionally, such that the pressure is constant. This occurs, for example, in a non-magnetized steady-state environment, where the sound crossing time is shorter than cooling time. Most of the other models that are being considered elsewhere in this paper (turbulent mixing, conductive interfaces, radiative shocks) are also characterized by pressure equilibrium. In the isochoric case, the temperature drops, but the gas does not compress. This occurs, for example, if magnetic pressure exceeds the thermal pressure in the gas, or if the flow is unconstrained by external pressure and allowed to diverge. For either of these cases (isobaric or isochoric), fixing the pressure or density

profile along the flow fixes the temperature profile as function of the time elapsed since the material passed the boundary.

In order to compare the model predictions to observations, we derive the column densities of the different ions along sightlines along the flow direction, i.e., perpendicular to the boundary. The column density of any given ion is equal to the integral of the ion's density times the length of the segment in the flow where the ion is present. Given a flow velocity v_0, and an amount of time dt spent at some given temperature, the segment's length is $v_0\,dt$. Each ion i has an elemental abundance, A_i. Its ionization fraction after some amount of time, t, since passing through the boundary is $f_i(t)$, as derived from the radiative cooling calculation. Thus, the ion's volume density at time t since crossing the boundary is $f_i(t)\,A_i\,n_{H,0}$. This implies a column density along the flow direction equal to

$$N_i = \int_0^t f_i(t')\,A_i\,v_0\,d(n_{H,0}t') = v_0\mu_i,$$

where this equation defines μ_i as a constant of the flow for each ion. Values for μ_i for a number of ions can be found in Table A1.

The fact that the column densities are proportional to the flow velocity, but do not depend on the density or ionization structure can be understood as follows. Start with a zone in the flow at a given temperature. If the density is high, the cooling time is short, and thus the thickness of the zone is small. At lower densities, the cooling time is long and thus the zone is thicker. The thickness of zone is thus proportional to the product of the density, the flow velocity and the time spent at a given temperature. Since the flow velocity is assumed to be a constant of the flow, the time evolution of a fluid element only depends on the product $(n_{H,0}t)$. This is referred to as the fluence, and it may be interpreted indirectly as a scaled spatial coordinate. The resulting scaling property allows us to run a case for a fixed density, and then rescale our results for an arbitrary density. We note that other models (radiative shocks, mixing layers, conductive interfaces) also exhibit scaling relations.

The same argument shows that the column density predictions will not change much with metallicity. Lowering the metal abundance increases the cooling time by the same factor, since the principal coolants are ions of oxygen. This means that the predictions for oxygen ions are nearly independent of oxygen abundances. To first order, the column densities for the other ions will also stay constant. However, a proper handling of this issue would require calculations using a number of different assumed abundances.

Photoionization

A crucial (and unique) aspect of the model described here is that it takes into account the ionizing radiation that is produced by the hot, upstream gas. Here we discuss a few

general implications of including photoionization.

For a given cooling history, the quantity $\phi_\nu = F_\nu/(n_{\mathrm{H,0}}v_0)$ is a constant of the flow, where F_ν is the photon flux emitted by the cooling gas at a given frequency and $(n_{\mathrm{H,0}}v_0)$ is the particle flux. The effectiveness of photoionization depends on the photoionization parameter, $U_i = n_{\gamma,i}/n_{\mathrm{H}}$, where $n_{\gamma,i} = (F_i/c)$ is the density of photons capable of ionizing some ion i. Therefore, we can express the ionization parameter at a given point in the cooling flow as $U_i = F_i/(cn_{\mathrm{H}}) = (\Phi_i/X)(v_0/c)$, where $X = n_{\mathrm{H}}/n_{\mathrm{H,0}}$ is the factor by which the flow has compressed, and Φ_i is the integral of ϕ_ν for photons that can ionize ion i.

For example, for a flow velocity of $v_0{=}60\ \mathrm{km\,s^{-1}}$, the ionization parameter in the photoionized part of an isochoric flow, where the hydrogen ionizing photons per H atom is $\Phi_{\mathrm{HI}}{=}4.3$ and the gas compression is $X = 1$, will be $\log U_{\mathrm{HI}}{=}{-}3.1$. In contrast, for isobarically cooling gas, where $\Phi_{\mathrm{HI}}{=}7.0$ and $X = 112$, the corresponding ionization parameter is $\log U_{\mathrm{HI}}{=}{-}4.9$. This low ionization parameter in isobarically cooling gas implies that there is no photoionization boost in this case. Despite the increased number of ionizing photons produced per atom in the cooling gas (due to pdV work), the compression lowers the effectiveness of photoionization.

The width of the photoionization zone, where the radiation from the hot section is reprocessed, can be estimated by equating the number flux of ionizing photons produced by the hot flow to the number of recombinations per hydrogen atom per second in the photoionized zone. Using the scaling relationships above this yields $L \sim v_0\Phi_{\mathrm{HI}}/(n_{\mathrm{H,0}}\alpha_{\mathrm{H}}X^2)$, where α_{H} is the Case A radiative recombination coefficient of hydrogen. Our numerically calculated lengths agree well with this analytical estimate, yielding $L{\sim}4/n_{-2}$ pc for the isobaric case and $L{\sim}800/n_{-2}$ pc for the isochoric case with $v_0{=}30\ \mathrm{km\,s^{-1}}$. The corresponding flow times are $t{=}3.3{\times}10^5/n_{-2}$ years for the isobaric case and $2.5{\times}10^7/n_{-2}$ years for the isochoric case.

The inclusion of photoionization produces a steeper than linear relationship between the column density and v_0, as demonstrated in Fig. A4 In this case, the column density can be written as $N_i = v_0\mu_i b_i(v_0)$, where $b_i(v_0)$ is a photoionization boost for ion i, which increases with flow velocity.

Column density predictions

The cumulative column density as a function of (normalized) position is shown in Fig. A2 for an isochoric flow with $v_0{=}30\ \mathrm{km\,s^{-1}}$, both with and without photoionization. Figure A3 shows the temperature evolution and the ionization fractions as function of position. In this example, the spatial thickness of the zone containing the highly ionized gas is $\sim100\,n_{-2}$ pc. When the effects of photoionization are added in, the pathlength occupied by C IV and

particularly Si IV is extended by a factor of 2 to 8.

Figure A4 shows the predicted column densities as function of the flow velocity, v_0. There are three useful insights that one can take from this figure. First, when comparing models to observations, *column density ratios are not necessarily independent of total column densities.* Models which successfully produce the observed ratios of column densities might do so in increments so large as to be inconsistent with the estimated column per component or so small as to require hundreds of interfaces along the line sight (as is e.g. the case for conductive interface layers). Second, for any reasonable set of parameters, the O VI and N V ions originate only in the thermal zone and are basically independent of the radiation field. This is because their ionization potentials are much higher than the typical photon energy (I.P., for going from O V to O VI 113.9 eV, for going from N IV to N V 77.47 eV). Third, if there is resistance to density compression (or a higher radiation field than that produced in the cooling gas alone), photoionization can become important in contributing to the column densities of Si IV (I.P. 33.49 eV), and C IV (I.P. 47.89 eV).

Figure A4 shows that the observed ranges of column densities through the Galactic corona for C IV and Si IV both are consistent with flow velocities between 15 and 35 $\mathrm{km\,s^{-1}}$. The range for N V (15 to 65 $\mathrm{km\,s^{-1}}$) overlaps with this, but in some directions higher flow velocities would be needed to produce the observed N V. On the other hand, such flows would predict too much O VI. Nevertheless, since this cooling flow is modeled as a simplified 1-dimensional flow, it is encouraging that there is a range of flow velocities for which all four column densities are similar to the observed values.

It is relatively easy to understand why the thermal and ionization structure of the cooling gas is independent of density or metallicity. However, if photoionization is important one might expect the volume density to influence the column densities. However, the photon flux from the flow is linearly proportional to the particle flux. This means that cooling flows produce a fixed number of ionizing photons per hydrogen atom, independent of the density. Thus, the column density predictions do not depend on the absolute value of the volume density (although they do depend on the density structure).

Emissivity predictions

In general, the density of the flow can be determined by comparing a column density ($\propto n_H$) with an emission line (or broadband) intensity ($\propto n_H^2$). With a model, any absorption/emission pair can be chosen. In the original Galactic Fountain model of Shapiro & Field (1976), for example, the combination of matching a model of soft X-ray emission and O VI column densities yielded a density large enough that it indicated outflowing gas would cool and fall back before reaching an equilibrium scaleheight, suggesting that hot gas in the
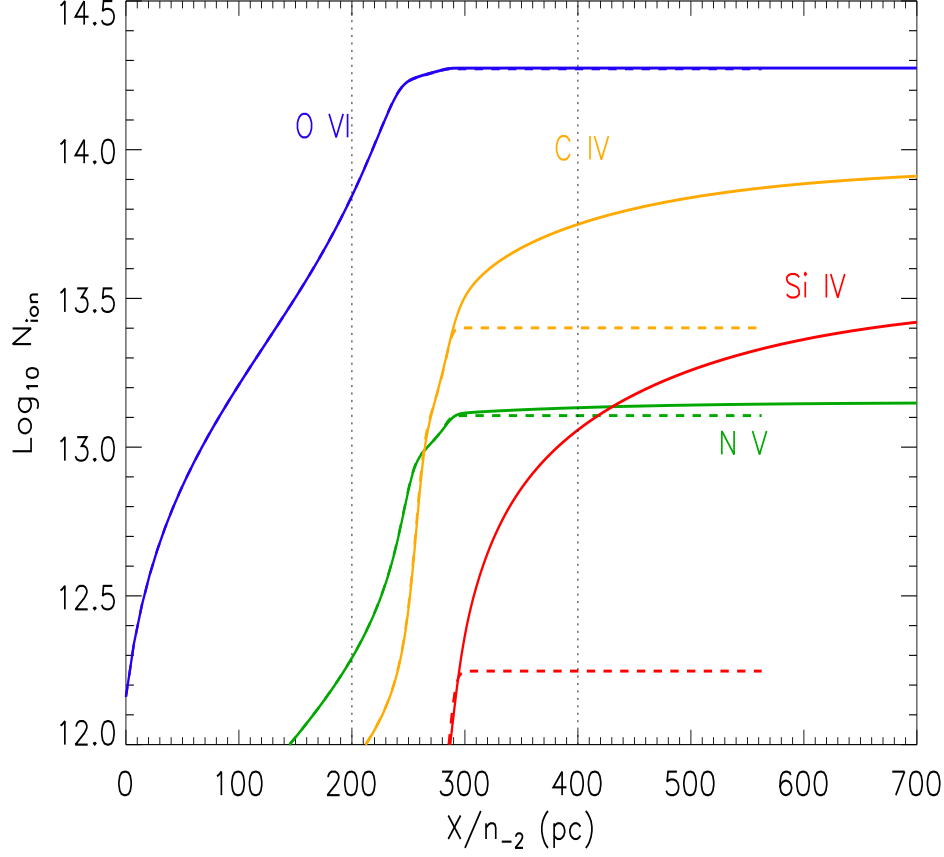
Fig. A2.— Cumulative column density of highly ionized gas as a function of (normalized) path length through an isochoric radiative cooling flow with v_0=30 km s^{-1}. The solid and dotted lines show the column density with and without the inclusion of photoionization from the radiation field produced by the cooling gas.
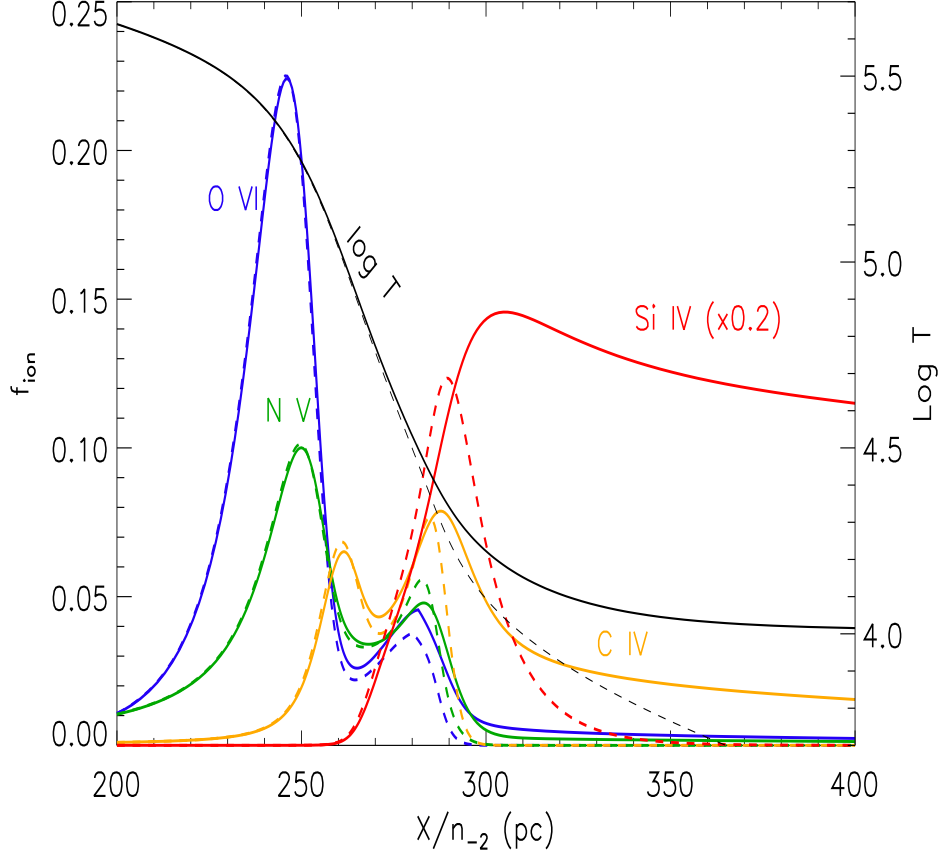
Fig. A3.— Ionization fractions (left axis) and temperature (right axis) as a function of normalized position for isochorically cooling gas with $v_0=30$ km s^{-1} for cases that include (solid) and do not include (dashed) the effects of photoionization. For clarity, the ionization fraction of Si IV has been multiplied by 0.2. The thickness of the zones scales linearly with v_0, although the zones where C IV and Si IV occur become more extended due to the enhanced photoionization.
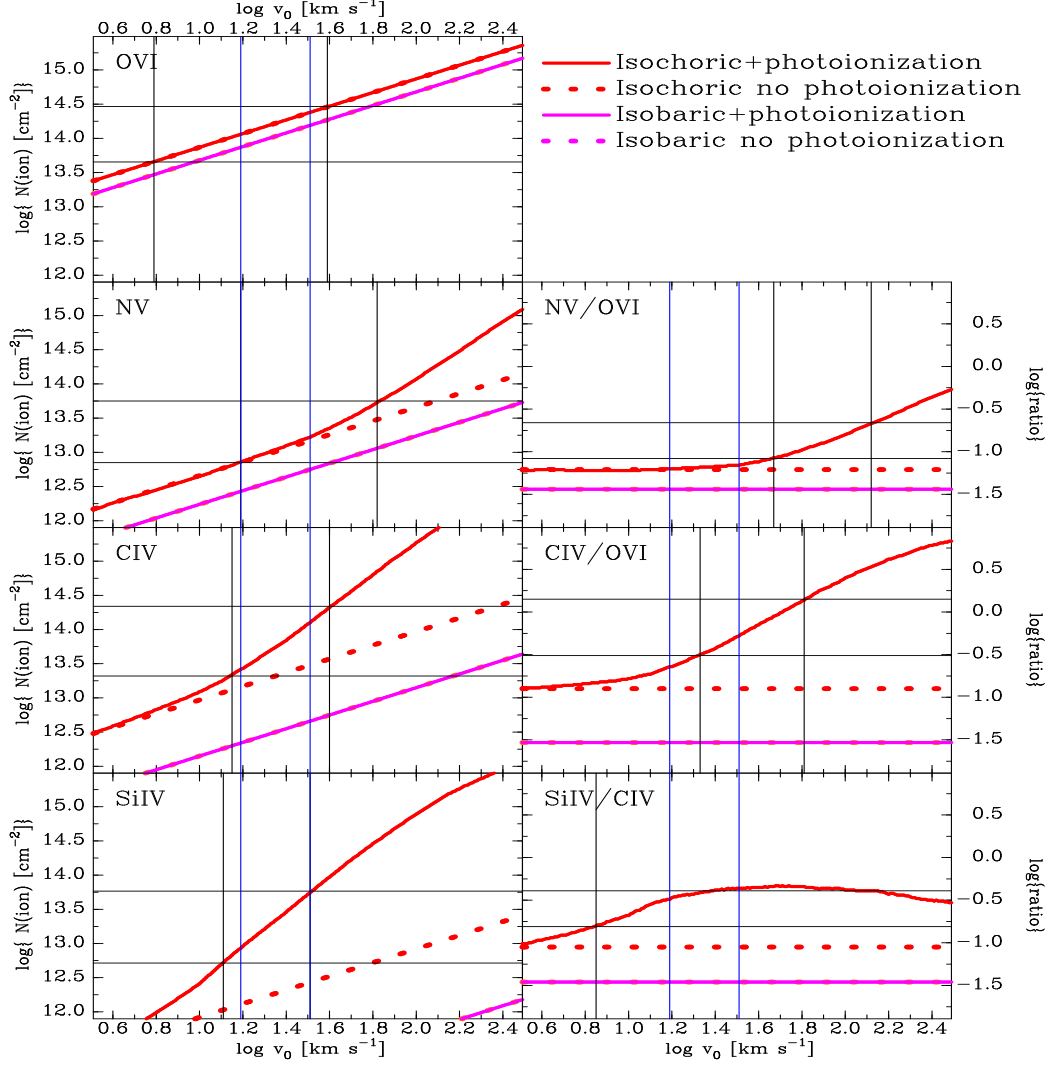
Fig. A4.— Left panels: column densities as a function of the logarithm of the flow velocity, v_0, for cases with isobaric cooling (magenta line) and for isochoric cooling with and without photoionization (red solid and red dashed line). Note that the column densities are linearly proportional to flow velocity for low velocities. Note the significant photoionization boost for N IV, C IV and Si IV, setting in at $\log v_0 \sim 1.4$, 1.0 and 0.7, respectively. Right panels: selected column densities ratios as a function of the logarithm of the flow velocity. In all panels the observed 1.5σ range around the average ionic column density or ratio observed in the Galactic corona is shown with horizontal lines. The averages and dispersions can be found in Sects. 4.5 and 4.8. In all panels vertical lines shows the range of velocities, v_0 for which the predicted column density or ratio falls within the observed range. The solid blue vertical lines show the velocity range within which all four column density predictions fit the observed range (15–$32 \ \mathrm{km \, s^{-1}}$).

disk might establish a convective-radiative cycle. The least model dependent results come from comparing the emission and absorption from a single ion. Martin & Bowyer (1990), for example, used the absorption/emission from C IV. However, the chief uncertainty in this approach is the possibility that a significant fraction of C IV could be produced in a photoionized region and therefore absorbing but not emitting. The body of O VI absorption and emission measurements now available from FUSE alleviates this problem, since it is expected that O VI absorption and emission arise in the same spatial region.

Since the intensity of any emission line is proportional to the particle flux, $I_j = (n_{H,0} v_0) b(v_0) \iota_j$, and the column densities are proportional to the flow velocity only, $N_i = v_0 a_i(v_0) \mu_i$, one can use the comparison of the two quantities to solve for the initial density of the flow, $n_{H,0} = (I_{j,obs}/N_{i,obs})(\mu_i/\iota_j)(a(v_0)/b(v_0))$, where $I_{j,obs}$ and $N_{i,obs}$ are the observed emission line intensity and column density from a region of interest. The constant of proportionality between the particle flux and emission line intensity, ι_j, is given in Table A1 for selected lines. The photoionization boost term for the intensities is $b(v_0)$. For infrared and optical lines, this correction can be quite significant. However, for ultraviolet and x-ray resonance lines, this correction is negligible, as the temperature in the photo-ionized zone is too low to excite these higher energy transitions. For example, the C IV $\lambda\lambda 1548, 1550$ doublet is enhanced by less than 10% in the photo-ionized isochoric flows for example.

Combining the results for the emission and absorption, and scaling these numbers to reasonable values, $N_{i,14} = N_i/10^{14} \, \mathrm{cm}^{-2}$ and $I_{j,1000} = I_j/(1000 \, \mathrm{photons \, s^{-1} \, cm^{-2} \, sr^{-1}})$ (line units=LU), we can solve for the initial flow density,

$$n_{H,0} = (10^{-3} \, \mathrm{cm}^{-2}) \left\{ \begin{array}{ll} (0.34/3.31) \, a_{CIV}(v_0) \, I_{CIV,1000}/N_{CIV,14} & \text{(isobaric/isochoric)} \\ (1.62/3.91) \, a_{OVI}(v_0) \, I_{OVI,1000}/N_{OVI,14} & \text{(isobaric/isochoric)} \end{array} \right\}, \quad (2)$$

where the intensity lines are the combined intensities of the resonance doublets of O VI and C IV. In this above equation, we neglect the (small) photoionization boost, $b_i(v_0)$ to the UV emission lines, and $a_{OVI}(v_0) \sim 1$. Note that since the isochoric case does not compress it must have a higher initial density to produce the same emergent intensity as an isobaric flow.

Observations of I(O VI) fall in the range 3000 to 7000 line units (Dixon & Sankrit 2008), while the 1σ range of N(O VI) is 1.3–$3.0 \times 10^{14} \, \mathrm{cm}^{-2}$ (this work). Unfortunately, there are not enough simultaneous measurements to judge whether these two quantities are correlated. Moreover, the intensity must be corrected for the extinction along the line of sight, and both quantities must be estimated for the same physical path length, c.f. Lei et al (2009) and Shelton et al (2010). Just using the values above to bracket the possible range of densities, we find that for isochoric flows, $n_{H,0}=0.3$-$1.5 \times 10^{-2} \, \mathrm{cm}^{-3}$. Using a mean O VI temperature of $\log T=5.3$ gives a thermal pressure in the O VI zone of $p/k=600$-$3000 \, \mathrm{cm}^{-3} \, \mathrm{K}$. For both isobaric and isochoric cases, the radiative cooling models predict I(O VI) to be ~ 6 times

greater than I(C IV) (in line units). There are very few directions toward which both lines have been estimated Shelton et al. (2010) combined SPEAR data for C IV with O VI from FUSE, finding a ratio ∼1. Using just SPEAR data, Welsh et al. (2007) find ratios <1 to ∼3 in directions toward the North Galactic Cap. These ratios indicate a larger C IV abundance or higher O VI abundances in thermal (non-photoionized) zones than expected from cooling gas. However, until more and especially more detailed observations are done, it will remain unclear how serious this discrepancy is.

Table 2—Continued

Object	vel. range	ion	strong line			weak line			ratios	
			$\log N$ [cm^{-2}]	$<v>$ [km s^{-1}]	FWHM [km s^{-1}]	$\log N$ [cm^{-2}]	$<v>$ [km s^{-1}]	FWHM [km s^{-1}]	ions	log ratio
(1)	km s^{-1}] (2)	(3)	(4)	(5)	(6)	(7)	(8)	(9)	(10)	(11)
		SIII	[H$_2$]							

Note. — a: The columns contain the following. Column 1: Target name. Column 2: Velocity range of integration for either all Milky Way Disk/Halo absorption or for individual components. Columns 4, 5, 6: Logarithmic column density, central velocity and second-moment width of the strong line of each doublet (O VI λ1031.926, N V λ1238.821, C IV λ1548.204, Si IV λ1393.760), *if* the measurement was deemed to be reliable; note that the listed widths are corrected for instrumental broadening (FWHM$_{\mathrm{corr}}$=$\sqrt{\mathrm{FWHM_{obs}^2 - Res^2}}$). Instrumental widths are 19 km s^{-1} for GHRS-G160M spectra, 30 km s^{-1} for STIS-G140M spectra, 6.5 km s^{-1} for STIS-E140M spectra, and $\sim$20 km s^{-1} for FUSE spectra. Values in square brackets are given for cases where we deemed it possible to make a measurement, but it is too unreliable to use in the analyses; notes in square brackets indicate the reason for a contamination or the identification of the line blending with the Galactic high-ionization absorption. Columns 7, 8, 9: Logarithmic column density, central velocity and second-moment width of the weak line of each doublet (O VI λ1037.617, N V λ1242.804, C IV λ1550.78, Si IV λ1402.772). Columns 10, 11: log of the ratio of the column densities of an ion pair, as identified in Col. 10. Values are omitted for all cases where the ratio was deemed untrustworthy.

Table A1. Cooling flow parameters (without photoionization effects)

Case	X^a	ϕ_{HI}^b	$\mu_{i,6}^c$					$\iota_{j,3}^d$	
			Si IV	C IV	N V	O VI	Ne VIII	C IV 1548 Å	O VI 1031 Å
Isobaric	112	7.0	0.037	1.35	1.67	41.40	27.93	4.0	25.6
Isochoric	1	4.3	0.59	8.39	4.26	62.33	23.87	2.5	15.9

[a]Density compression of gas, $n_{\mathrm{H}}/n_{\mathrm{H,o}}$ between T_o=10^6 K and $T\sim10^4$ K.

[b]Hydrogen ionizing photons produced per H atom in flow.

[c]Column density normalized to initial flow velocity, $\mu_i = N_i/v_o$, in units of 10^6 cm^{-3} s when photoionization is neglected.

[d]Emission line intensity of resonance doublet normalized to flow mass flux, $\iota_{j,-3} = I_j/(n_{\mathrm{H,o}}v_0)$ in units of 10^3 photons ster^{-1}.

References

Allen C.W., 1973, Astrophysical Quantities (London: The Athlone Press)

Asplund M., Grevesse N., Sauval A.J., Scott P., 2009, ARA&A, 47, 481

Begelman M.C., Fabian A.C., 1990, NNRAS, 244, 26P

Benjamin R.A., Shapiro P.R., 1993, in "UV and X-ray Spectroscopy of Laboratory and Astrophysical Plasmas", eds. Silver E.H. & Kahn S.M., (Cambridge: Cambridge University Press), p280

Benjamin R.A., 1994, Ph.D. thesis University of Texas

Borkowski K.J., Balbus S.A., Fristrom C.C., 1990, ApJ, 355, 501

Bregman, J.N. 1980, ApJ, 236, 577

Bunner A.N., Coleman P.L., Kraushaar W.L., McCammon D., Williamson F.O., 1973, ApJ, 179, 781

Bowen D., et al. 2008, ApJS, 176, 59

Collins J.A., Shull J.M., Giroux M.K., 2004, ApJ, 605, 216

Collins J.A., Shull J.M., Giroux M.K., 2005, ApJ, 623, 195

Cowie L.L., Jenkins E.B., Songaila A., York D.C., 1979, ApJ, 232, 467

Cowie L.L., Taylor W., York D.G., 1981, ApJ, 248, 528

de Avillez M.A., Breitschwerdt D., 2005, ApJ, 634, L65

Dixon W.V.D., Sankrit R., 2008, ApJ, 686, 1162

Dopita M.A., Sutherland R.S., 1996, ApJS, 102, 161

Edgar R.J.. Chevalier R.A., 1986, ApJ, 310, L27

Esquivel A., Benjamin R.A., Lazarian A., Cho J., Leitner S.N., 2006, ApJ, 648, 1043

Everett J.E., Zweibel E.G., Benjamin R.A., McCammon D., Rocks L., Gallagher J.S., 2008, ApJ, 674, 258

Fox A.J., Savage B.D., Sembach K.R., Fabian D., Richter P., Meyer D.M., Lauroesch J., Howk J.C., 2003, ApJ, 582, 793

Fox A.J., Savage B.D., Wakker B.P., Richter P., Sembach K.R., Tripp T.M., 2004, ApJ, 602, 738

Fox A.J., Wakker B.P., Savage B.D., Tripp T.M., Sembach K.R., Bland-Hawthorn J., 2005, ApJ, 630, 332

Fox A.J., Savage B.D., Wakker B.P., 2006, ApJS, 165, 279

Fox A.J., Petitjean P., Ledoux C., Srianand R., 2007, A&A, 465, 171

Fox A.J., Prochaska J.X., Ledoux C., Petitjean P., Wolfe A.M., Srianand R., 2009, A&A, 503, 731

Fox A.J., Wakker B.P., Smoker J.V., Richter P., 2010, ApJ, 718, 1046

Fraternali F., Oosterloo T.A., Sancisi R., 2004, A&A, 424, 485

Gaensler B.M., Madsen G., Chatterjee S., Mao S.A., 2008, PASA, 25, 184

Ganguly R., Sembach K.R., Tripp T.M., Savage B.D., 2005, ApJS, 157, 253

Gnat O., Sternberg A., 2007, ApJS, 168, 213

Gnat O., Sternberg A., 2009, ApJ, 693, 1514

Gnat O., Sternberg A., McKee, 2010, ApJ, 718, 1315

Heald G.H., Rand R.J., Benjamin R.A., Bershady M.A., 2006, ApJ, 647, 1018

Heald G.H., Rand R.J., Benjamin R.A., Bershady M.A., 2007, ApJ, 663, 933

Henley D.B., Shelton R.L., Kwak K., Joung M.R., Mac Low M.-M., 2010, ApJ, 723, 935

Houck, J.R., Bregman, J.N. 1990, ApJ, 352, 506

Howk J.C., Savage B.D., Sembach K.R., Hooper C.G., 2002, ApJ, 572, 264

Howk J.C., Sembach K.R., Savage B.D., 2003, ApJ, 586, 249

Hulsbosch A.N.M., Wakker B.P. 1988, A&AS, 75, 191

Indebetouw R., Shull J.M., 2004a, ApJS, 605. 205

Indebetouw R., Shull J.M., 2004b, ApJ, 607, 309

Jenkins E.B., Meloy D.A., 1974, ApJ, 193, L121

Jenkins E.B., 1978a, ApJ, 219, 845

Jenkins E.B., 1978b, ApJ, 220, 107

Jenkins E.B., et al., 1998, ApJ, 492, 147

Jenkins E.B., Oegerle W.R., Gry C., Vallerga J., Sembach K.R., Shelton R.L., Ferlet R., Vidal-Madjar A., York D.G., Linsky J.L., Roth K.C., Dupree A.K., Edelstein J., 2000, ApJ, 538, L81

Kalberla P.M.W., Burton W.B., Hartmann D., Arnal E.M., Bajaja E., Morras R., Pöppel W.G.L., 2005, A&A, 440, 775

Kahn, F.D. 1981, in Investigating the Universe: Papers presented to Zdenek Kopal on the occasion of his retirement, September 1981 (Dordrecht, Reidel), 1

Kim-Quijano, J. et al. 2007, STIS Instrument Handbook, Version 8.0, (Baltimore: STScI).

Keeney B.A., Danforth C.W., Stocke J.T., Penton S.V., Shull J.M., Sembach K.R., 2006, ApJ, 646, 951

Kwak K., Shelton R.S., 2010, ApJ, 719, 523

Knauth D.C., Howk J.C., Sembach K.R., Lauroesch J.T., Meyer D.M., 2003, ApJ, 592, 946

Kuntz K.D., Danly L. 1996, ApJ, 457, 703

Lehner N., Jenkins E.B., Gry C., Moos H.W., Chayer P., Lacour S., 2003, ApJ, 595, 858

Lehner N., Howk J.C., 2010, ApJ, 709, L138

Lehner N., Zech W.F., Howk J.C., Savage B.D., 2011, ApJ, 727, 461

Lei S., Shelton R.L., Henley D.B., 2009, ApJ, 699, 1891

Martin C., Bowyer S., 1990, ApJ 350, 242

Münch, G. 1952, PASP, 64, 312

Münch, G., Zirin, H., 1961, ApJ, 133, 11

Oegerle W.R., Tripp T.M., Sembach K.R., Jenkins E.B., Bowen D.V., Cowie L.L., Green R.F., Kruk J.W., Savage B.D., Shull J.M., York D.G., 2000, ApJ, 538, L23

Oegerle W.R., Jenkins E.B., Shelton R.L. Bowen D.V., Chayer P., 2005, ApJ, 622, 377

Oosterloo T.A., Fraternali F., Sancisi R., 2007, AJ, 134, 1019

Petitjean P., Ledoux C., Srianand R., 2008, A&A, 480, 349

Raymond J.C., Smith, B.W., 1977, ApJS 35, 419

Richter P., 2006, Reviews in Modern Astronomy, 19, 31

Rogerson J.B., York D.G., Drake J.F., Jenkins E.B., Morton D.C., Spitzer L., 1973, Ap, 181,

L110

Romanik C.J., 1988, ApJ, 330, 1022

Savage B.D., de Boer K.S., 1979, ApJ, 230, L77

Savage B.D., de Boer K.S., 1981, ApJ 243, 460

Savage, B.D., Massa, D. 1987, ApJ, 314, 380

Savage B.D., Edgar R., Diplas A., 1990, ApJ, 361, 107

Savage B.D., Sembach K.R., 1991, ApJ, 379, 245

Savage B.D., Sembach K.R., 1994, ApJ, 434, 145

Savage B.D., Sembach K.R., Lu L., 1995, ApJ, 449, 145

Savage B.D., Sembach K.R., Tripp T.M., 1997a, ApJ, 480, 216

Savage B.D., Sembach K.R., Lu L., 1997b, AJ, 113, 2158

Savage B.D., Sembach K.R., Howk J.C., 2001a, ApJ, 547, 907

Savage B.D., Meade M., Sembach K.R., 2001b, ApJS, 136, 631

Savage B.D., Sembach K.R., Wakker B.P., et al., 2003, ApJS, 146, 125

Savage B.D., Wakker B.P., Fox A.J., Sembach K.R., 2005, ApJ, 619, 863

Savage B.D., Lehner N., 2006, ApJS, 162, 134

Savage B.D., Wakker B.P., 2009, ApJ 702, 1472

Sembach K.R., Savage B.D., Massa D., 1990, ApJ, 355, 114

Sembach K.R., Savage B.D., Massa D., 1991, ApJ, 372, 81

Sembach K.R., Savage B.D., 1992, ApJS, 83, 147

Sembach K.R., Savage B.D., Cardelli J.A., 1994a, ApJ, 420, 183

Sembach K.R., Savage B.D., Jenkins E.B., 1994b, ApJ, 421, 585

Sembach K.R., Savage B.D., 1994, ApJ, 431, 201

Sembach K.R., 1994, ApJ, 434, 244

Sembach K.R., Savage B.D., Lu L., 1995, ApJ, 439, 672

Sembach K.R., Savage B.D., Hurwitz M., 1999, ApJ, 524, 98

Sembach K.R., Howk J.C. Savage B.D., Shull J.M., Oegerle W.R., 2001, ApJ, 561, 573

Sembach K.R., Wakker B.P., Savage B.D., Richter P., Meade M., Shull J.M., Jenkins E.B., Sonneborn G., Moos H.W., 2003, ApJS, 146, 165

Shapiro P.R., Field G.B., 1976, ApJ, 205, 762

Shapiro P.R., Benjamin R., 1991, PASP, 103, 923

Shapiro P.R., Benjamin R.A., 1993, in "Star-Forming Galaxies and their Interstellar Media", ed. Franco J.J., (Cambridge: Cambridge University Press), p273

Shelton R., 1998, ApJ, 504, 785

Shelton R.L., Henley D.B., Dixon W.V., 2010, ApJ, 722, 302

Shull J.M., van Steenberg M.E., 1985, ApJ 298, 268

Skillman E.D., 1998, in "VIII Canary Islands Winter School of Astrophysics: Stellar Astrophysics for the Local Group", eds. A. Aparicio, A. Herrero, F. Sánchez

Slavin J.D., Shull J.M., Begelman M.C., 1993, ApJ, 407, 83

Sutherland R.S., Dopita M.A., 1993, ApJS, 88, 253

Spitzer L., 1956, ApJ, 124, 20

Spitzer L., 1990, ARA&A, 28, 71

Spitzer L., 1996, ApJ, 458, L29

Sterling N.C., Savage B.D., Richter P.R., Fabian D., Sembach K.R., 2002, ApJ, 567, 354

Tripp T.M., Sembach K.R., Savage B.D., 1993, ApJ, 415, 652

Wakker B.P., 2001, ApJS, 146, 463

Wakker B.P., 2004, in "High-velocity clouds", Astrophysics and Space Science Library, vol. 312, Kluwer-Dordrecht, p25

Wakker B.P., 2006, ApJS, 163, 282

Wakker B.P., Howk J.C., Savage B.D., van Woerden H., Tufte S.R., Schwarz U.J., Benjamin R., Reynolds R.J., Peletier R.F., Kalberla P.M.W., 1999, Nature, 400, 388

Wakker B.P., Savage B.D., Sembach K.R., et al., 2003, ApJS, 146, 1

Wakker B.P., York D.G., Howk J.C., Barentine J.C., Wilhelm R., Peletier R.F., van Woerden H., Beers T.C., Ivezić Z, Richter P., Schwarz U.J., 2007, ApJL, 670, L113

Wakker B.P., Savage B.D., 2009, ApJS, 182, 378

Welsh B.Y., Edelstein J., Korpela E.J., Kregenow J., Sirk M., Min K.-W., Park J.W., Ryu K., Jin H., Yuk I.-S, Park J.-H., 2007, A&A 472, 509

Williamson F.O., Sanders W.T., Kraushaar W.K., McCammon D., Borken R., Bunner A.N., 1974, ApJ, 193, L133

York D.G., 1974, 193, L127

York D.G., 1977, ApJ, 213, 43

Zsargó J., Sembach K.R., Howk J.C., Savage B.D., 2003, ApJ, 586, 1019